UC Berkeley
UC Berkeley Electronic Theses and Dissertations

Title

Estimation, Identification and Data-Driven Control Design for Hard Disk Drives

Permalink

https://escholarship.org/uc/item/0998n097

Author

Bagherieh, Omid

Publication Date

2017

Peer reviewed|Thesis/dissertation

Estimation, Identification and Data-Driven Control Design for Hard Disk Drives

by

Omid Bagherieh

A dissertation submitted in partial satisfaction of the

requirements for the degree of

Doctor of Philosophy

in

Engineering - Mechanical Engineering

in the

Graduate Division

of the

University of California, Berkeley

Committee in charge:

Professor Roberto Horowitz, Chair
Professor Masayoshi Tomizuka
Professor Claire Tomlin

Spring 2017

Estimation, Identification and Data-Driven Control Design for Hard Disk Drives

Abstract

Estimation, Identification and Data-Driven Control Design for Hard Disk Drives

by

Omid Bagherieh

Doctor of Philosophy in Engineering - Mechanical Engineering

University of California, Berkeley

Professor Roberto Horowitz, Chair

The demand for online storage has been increasing significantly during the last few years. Hard disk drives are the primary storage devices used in data centers for storing these online contents. The servo assembly of the dual-stage Hard Disk Drive (HDD) is composed of the Voice Coil Motor (VCM) and the Mili-Actuator (MA), where the VCM is responsible for coarse positioning at low frequency regions and the MA is responsible for fine positioning at high frequency regions. Controlling these two actuators is very critical in precision positioning of the read/write head, which is mounted at the edge of the servo assembly. In this dissertation, the precision positioning of the head during the self-servo writing process as well as feed-forward and feedback controls in the track following mode are considered.

This dissertation discusses three control design methodologies for hard disk drives servo systems, in order to improve their performance as well as their reliability. The first is a state estimator for non-uniform sampled systems with irregularities in the measurement sampling time, which estimates the states at a uniform sampling time. The second is an online uncertainty identification algorithm, which parameterizes and identifies the uncertain part of transfer functions in a dual-stage HDD. The third is a frequency based data-driven control design methodology, which considers mixed H_2/H_∞ control objectives and is able to synthesize track following servo systems for dual stage actuators utilizing only the frequency response measurement data, without the need of identifying the models of the actuators.

The state estimator design for non-uniform sampled systems with irregularity in the measurement sampling time is considered, where it is proposed to design an observer to estimate the states at a uniform sampling time. This observer is designed using a time-varying Kalman filter as well as a gain-scheduling observer. The Kalman filter has the optimal performance, while the gain-scheduling observer requires relatively lower computational power. Simulations are conducted involving the self-servo writing process in hard disk drives, where performance as well as computational complexity of these two observers are compared under different noise scenarios.

Uncertainties in system dynamics can change the closed loop transfer functions and affect the performance or even stability of the control algorithm. These uncertainties are

parameterized as stable terms using coprime factorizations, and are identified in an online fashion. The uncertainty identification, in comparison to the complete transfer function identification, requires less computational power as well as a smaller order for the identified transfer function.

The proposed online uncertainty identification algorithm is utilized to factorize and identify the uncertain part of transfer functions in a dual-stage Hard Disk Drive (HDD). The dual-stage actuators' gains and resonance modes are affected by temperature variations, which in turn affect all closed loop transfer functions. Therefore, these transfer functions must be periodically updated in order to guarantee the convergence and stability criteria for the adaptive Repeatable Run-Out (RRO) following algorithm proposed in [61, 62]. Experimental results conducted on a hard disk drive equipped with dual-stage actuation, confirm the effectiveness of the proposed identification algorithm.

A frequency based data-driven control design considering mixed H_2/H_∞ control objectives is developed for multiple input-single output systems. The main advantage of the data-driven control over the model-based control is its ability to use the frequency response measurements of the controlled plant directly without the need to identify a model for the plant. In the proposed methodology, multiple sets of measurements can be considered in the design process to accommodate variations in the system dynamics. The controller is obtained by translating the mixed H_2/H_∞ control objectives into a convex optimization problem. The H_∞ norm is used to shape closed loop transfer functions and guarantee closed loop stability, while the H_2 norm is used to constrain and/or minimize the variance of signals in the time domain.

The proposed data-driven design methodology is used to design a track following controller for a dual-stage HDD. The sensitivity decoupling structure[34] is considered as the controller structure. The compensators inside this controller structure are designed and compared by decoupling the system into two single input-single-output systems as well as solving for a single input-double output controller.

Contents

List of Figures

List of Tables

Acknowledgments

This thesis has not been possible without the help, support and inspirations from many people. I would like to take this opportunity to thank all these great people. First, I want to thank my supervisor, Professor Roberto Horowitz who provided me the opportunity to be part of his great team. I would also like to thank him for his patience, encouragement and support during my PhD studies. His guidance has been extraordinary helpful during my graduate studies at UC Berkeley.

I must express my gratitude to the Controls group at UC Berkeley. I am indebted to them for their help. I would like to thank my thesis committee members, Professor Masayoshi Tomizuka and Professor Claire Tomlin for all their help, guidance and suggestions. I would also like to thank Professor Kameshwar Poolla, Professor Reza Alam, Professor Sanjit Seshia and Professor Ikhlaq Sidhu for serving as my PhD Qualifying exam committee. I want to take the opportunity and thank my master's degree supervisor, Professor Ryozo Nagamune who has paved the way for my success in my graduate studies.

Completing this work would have not been possible without the support from the data storage industry. I would like to thank the Advance Storage Technology Consortium, Western Digital Corporation and Hitachi Global Storage Technologies for all their support and guidance. I would also like to especially thank Western Digital Corporation for giving me the opportunity to closely work with them as an intern. I am really grateful of Dr. Guoxiao Guo, Dr. Young-Hoon Jake Kim, Dr. Richard Conway and Dr. Siri Weerasooriya for their advice, guidance and suggestions.

I need to thank all my laboratory members at Computer Mechanics Laboratory-Servo Group. I would like to thank Ehsan Keikha, Behrooz Shahsavari, Jinwen Pan, Prateek Shah and Zhi Chen for their help, support and encouragement.

Last but not the least, I would like to sincerely thank my family whom have made this journey possible for me. I am grateful to my wife and love of my life, Atoosa for her continuous support, encouragement and love. I want to express my deep and sincere gratitude to my parents, parents-in-law and my brother for their unconditional support and love throughout my life.

Chapter 1

Introduction

1.1 Introduction

Rapid development of Internet and computer technologies continue to demand ever increasing digital data storage. Hard disk and solid state drives are the dominant players in the digital storage game. Hard Disk Drives (HDDs) are primarily used in data centers, while Solid State Drives (SSDs) are mainly used in personal computers and portable devices [43]. It is predicted that the amount of data stored in data centers will increase by a factor of six from 2015 to 2020 [63]. As a consequence, data centers need to be equipped with high storage density devices, with continuous improvement of their reliability and performance.

Hard disk drive servo systems and their structures are described in chapter 2. High precision positioning of the actuators in HDDs is critical for the performance and reliability of these devices. There have been significant scientific efforts to improve the HDD performance and reliability using a variety of control theories [1, 5, 17]. These control theories design controllers which are utilized during the manufacturing as well as the operating stages of the HDD.

In one of the manufacturing process, servo patterns are written on the disk surface [5]. These patterns are used as a reference for measuring the head position during the operating stage. The conventional mechanism for writing these servo patterns is to use an external device [2], which increases the HDD manufacturing time. The latest methodology uses the HDD head to write these patterns [27, 68]. This new methodology is called the self-servo writing process [13, 16, 22] and is helpful in decreasing the HDD manufacturing time.

In one of the procedures used in the self-servo writing process, the actuator control inputs are updated at a uniform sampling time, but the feedback measurements are arriving at a nonuniform sampling time [12, 59, 70]. In order to close the loop and form a feedback controller, the inconsistency between measurements and control input sampling times should be resolved. Chapter 3 proposes to design an observer which can estimate system states at the control input uniform sampling time. Therefore, the output of this observer can be used to generate the uniform sampled control inputs.

The variations in the measurements sampling times can be modeled as plant dynamics variations [12, 60], where the plant model is obtained as an explicit function of the sampling time variations. The observers for this class of plants will be obtained using Kalman filter [40] and gain-scheduling [23, 24] techniques. In the gain-scheduling technique, the functionality of the plant model on the sampling time is considered in the design step, and the observer will be designed as a function of sampling time variations. The Kalman filter will obtain the optimal observer, which minimizes trace of a-posteriori state estimation error covariance for given variances of noises. The performance of the gain-scheduling observers will be evaluated by comparing them with Kalman filters. Although the tuned Kalman filter has optimal performance, observers designed using gain-scheduling techniques are significantly more computationally efficient [23, 24]. The performance of detuned gain-scheduling and Kalman filters will be compared in chapter 3.

The controllers designed for the operating stage of the HDD can be categorized as feed-forward and feedback controllers [5, 35, 46]. The feed-forward controllers are primarily used for track seek controls, repeatable run-out following and vibration rejection [10, 20, 38], while the feedback controllers are primarily used for stabilizing the closed loop system considering a desired set of performance specifications [30, 31, 52, 53] as well as vibration rejection [19, 66]. Examples of HDD feed-forward and feedback controls will be given in chapters 4 and 6, respectively.

Bit patterned media is a new technology that the HDD industry is exploring in order to increase storage density by writing data in magnetic islands [57, 67]. In conventional HDDs, data are written in concentric tracks and read back from those tracks. However, there are repeatable and non-repeatable run-out in the system, which the HDD track-following servo attempts to reject, in order to write and read on near circular tracks [5, 12, 21]. In bit patterned media, data are written on the predetermined tracks that are not concentric and maybe subjected to significant Repeatable Run-Out (RRO). As a consequence, in Bit-Pattern Media (BPM), the HDD track following servo must follow the repeatable run-out instead of rejecting it.

An adaptive RRO following algorithm for BPM was presented in [61, 62]. The proposed feed-forward controller was designed to follow the RRO using an adaptive algorithm by estimating the signals that must be injected in a feed-forward fashion, in order to track the RRO on the disk [61, 62]. This methodology utilizes a modified filtered-X LMS method [4, 49, 58], which requires a sufficiently accurate model of the closed-loop sensitivity transfer function. The required condition for convergence of this algorithm is that the phase mismatch between this model and its actual transfer function should be less than 90 degrees [11].

Temperature variations affect actuators' gains and resonance modes, which will change closed-loop sensitivity transfer functions. Therefore, these transfer functions must be period-ically updated in order to guarantee satisfaction of the 90-degree criteria. Chapter 4 utilizes coprime factorizations [26, 64] in order to estimate plant uncertainty relative to a nominal closed-loop error rejection transfer function. Therefore, only identification of the uncertain part is required [11, 64].

The feedback controllers in HDDs are designed primarily for stabilizing the actuators

as well as achieving the desired performance specifications required for reliable and precise positioning of the read/write head mounted on the edge of the servo assembly [31, 69]. The most common configuration for the servo assembly is to use the *dual-stage actuation*, which uses two actuators to control the head position [6]. The controllers for the dual-stage actuation can be designed using either the model of actuators or their frequency response measurement data sets. The former is called the model-based control design [1, 31], while the later one is called the data-driven control design [28, 41, 42].

The data-driven control design is a frequency-based methodology, which designs the controller based on the frequency response measurements of the plant rather than using the plant model in the design process [14, 41, 42]. The main advantage of using frequency measurement is to represent the real dynamics of the system, while the model cannot capture all the dynamics represented by the measurement. Moreover in the model-based control design, the order of the controller is a function of the model complexity. Therefore, if a relatively high order model is used to accurately represent the measurement, the resulting controller will be relatively high order and may not be practical to implement. In the data-driven approach, the controller order is predetermined and depends on how aggressive the control objectives are.

The robust control theory has been developed to consider dynamics uncertainties in the design process [32, 72]. In the model-based robust control, the nominal model as well as uncertainties are modeled based on the available measurements [47, 56]. However, this methodology has two major drawbacks. The first drawback is that the accurate modeling requires high order dynamics for both the nominal model and the uncertainties, which will lead to a high order controller [72]. The second drawback is that the modeled uncertainties may not be representing the actual variations in the system dynamics [29]. In the data-driven control design, the measurements represent the real dynamics of the system. Therefore, if the number of measurements are adequate enough to represent uncertainties and modes of the system, the stability and performance level achieved in the design step are guaranteed to be achieved when implementing the controller on the real system [14]. Moreover, the data-driven control methodologies can be useful in designing a common controller for a set of plants produced in a production line [36]. The dynamics variations among all these plants are represented by their frequency response measurements, and the data-driven control methodologies use these measurements to design a common controller for all these plants.

In order to design the controller using the data-driven control methodology in the frequency domain, the state of the art is to convert the problem into an optimization problem where H_2 and/or H_∞ norms of the closed loop transfer functions can be considered as the objective and/or constraints. The data-driven H_∞ control problem for Single Input-Single Output (SISO) systems was addressed in [42], where a necessary and sufficient convex condition for the H_∞ norm constraint was obtained. This H_∞ control methodology is extended to systems with Multiple Input-Single Output (MISO) in chapter 5. A sufficient convex condition for the H_∞ norm of Multi Input-Multi Output (MIMO) systems was also developed in [41]. The data-driven H_2 control problem for SISO systems with pre-specified control structures such as Finite Impulse Response (FIR) filters was given in [14]. The data-driven

H_2 control for MIMO systems with general control structures was developed in [41], where a sufficient convex condition for the upper-bound of the H_2 norm of closed loop transfer functions was derived.

The H_∞ and H_2 norm criteria for the closed loop transfer functions can be considered as a mixed H_2/H_∞ control problem [41, 44]. This problem is addressed in chapter 5 for MISO systems. The proposed algorithm combines the necessary and sufficient convex conditions for the H_∞ norm and the sufficient convex conditions for the H_2 norm [41]. The mixed H_2/H_∞ developed in [41] used a sufficient convex condition for the H_∞ norm, whereas a necessary and sufficient convex condition for the H_∞ norm is considered here. Moreover, the mixed H_2/H_∞ in [41] designs the controller based on one set of frequency response measurement of the system. However, one set of measurement cannot represent the uncertainties in the plant dynamics, and multiple measurements are required to capture these uncertainties [54]. Therefore, multiple measurements are considered in the proposed algorithm.

The proposed data-driven mixed H_2/H_∞ methodology is applied to a dual-stage HDD in chapter 6. The dual-stage HDD utilizes two actuators for the precision positioning of the read/write head [3, 5, 25]. These actuators have several resonance modes [9, 37]. Including each of these resonance modes in the actuator model directly increases the controller order [72]. However by using the data-driven control methodology, all these modes are already included in the system frequency response measurements and are considered in the controller design step without any direct effect on the controller order [14]. In the proposed methodology, the controller order is fixed and is a function of the control objectives rather than a direct function of the model complexity.

The dual-stage HDD accepts two control inputs, while having only one measurement output. Therefore, the controller for this system will be a single input-double output controller. The conventional design methodology in the HDD industry is to decouple the system into two SISO systems using a well-known methodology called the sensitivity decoupling approach [1, 45, 34]. Therefore, the individual controllers can be obtained in two sequential steps by considering the mixed H_2/H_∞ design process for SISO systems. Chapter 6 proposes to use the mixed H_2/H_∞ methodology developed for MISO systems, where the complete SIMO control block will be obtained in one step. The controller synthesized using the MISO design strategy will be compared with the controller synthesized using the sequential SISO design strategy. The main advantage of the MISO design is its ability to design both controllers in one step, rather than having one controller fixed in the design of the other controller.

1.2 Contributions of Each Chapter

The contributions for each chapter of the dissertation are provided below.

- **Chapter 2:** This chapter provides a general overview of the hard disk drive structure and mechanisms. Moreover, the control blocks diagram used for precision positioning of the head will be explained in this chapter.

- **Chapter 3:** The observer design problem for systems with uniform sampled control inputs and non-uniform sampled measurements is considered in this chapter. The non-uniformity in the measurement sampling time is modeled as plant dynamics variations, and an observer which can estimate system states at uniform sampled time is designed for this varying plant. This observer is designed using the gain-scheduling methodology and its performance as well as its computational complexity will be evaluated in comparison with a Kalman filter under several different noise scenarios.

- **Chapter 4:** Temperature variations in HDDs can move system resonance modes which directly affect system dynamics. These variations in system dynamics are described by stable uncertainty parameterizations using coprime factorizations [26, 64], which will be identified in an online fashion. The main reason for parameterizing the uncertainty is to avoid unnecessary identification of the unchanged part of the plant dynamics. Therefore, the uncertainty identification, in comparison to the complete plant dynamics identification, will require less computational power as well as a smaller order for the identified transfer function.

  The uncertainty parameterizations are identified for an experimental dual-stage HDD, where its dynamics is changing mainly as a function of temperature. The identification is done in an online fashion, where the identified uncertainty parameterizations are used to guarantee the stability and convergence criteria for the adaptive RRO following algorithm proposed in [61, 62].

- **Chapter 5:** The data-driven control design methodology, which designs the controller based on the frequency response measurements of the system, is discussed in this chapter. The main advantage of data-driven control over model-based control is the ability of data-driven control methodology in using the frequency response measurements directly without the need to identify a model. Therefore, the designed controller is guaranteed to stabilize the real system and achieve the performance specifications considered in the design process.

  The control objectives considered in the data-driven approach are usually described in terms of H_∞ and H_2 norms of closed loop transfer functions. The controller is obtained by solving a convex optimization problem, where these norms are translated to convex constraints and objectives. The necessary and sufficient convex conditions for the H_∞ constraints of the SISO systems were proposed in [42]. This chapter will extend these result to MISO systems. Moreover, the extended results are considered along with H_2 results from [41] to form a mixed H_2/H_∞ control problem. The plant dynamics variations are addressed by considering multiple frequency response measurements of the plant in the design step.

- **Chapter 6:** The data-driven mixed H_2/H_∞ control algorithm proposed in chapter 5 is used to design a track-following controller for a dual-stage HDD. The designed controller is a SIMO controller with the sensitivity decoupling structure. However, the

controllers inside this block are designed and compared using the sequential SISO and SIMO data-driven design strategies. In the sequential SISO design strategy, the dual-stage closed loop system is decoupled into two SISO loops, where the controller for each loop is synthesized using the SISO mixed H_2/H_∞ control algorithm. On the other hand, the SIMO design strategy will synthesize a SIMO controller for the MISO plant in one step.

- **Chapter 7:** This chapter concludes the dissertation by providing a concise conclusion of the materials discussed in different chapters. Moreover, the potential future works and directions are provided. One of the proposed future works is the potential guideline for the extension of the developed data-driven H_∞ control designs from MISO to MIMO systems, where a necessary and sufficient condition for the H_∞ norm constraint is obtained.

- **Appendix A:** The algorithm for data-driven H_∞ control design is extended to MISO systems in chapter 5. The proof of this algorithm is provided in this appendix.

- **Appendix B:** The closed loop transfer functions as well as their H_∞ constraints used to shape these closed loop transfer functions are shown here. These results are obtained for the example used in chapter 6.

1.3 Notations and Preliminaries

The notations used throughout this dissertation will be introduced in this section. The set of real and complex matrices with m rows and n columns are denoted as $\mathbb{R}^{m \times n}$ and $\mathbb{C}^{m \times n}$, respectively. The set of real and complex scalars use the same notation without the superscript. Considering a complex scalar $a \in \mathbb{C}$, the real and imaginary parts of the scalar a are denoted as $Re(a)$ and $Im(a)$. The magnitude of this scalar is also denoted as $|a|$.

The dimensions of a complex matrix are shown as a subscript, where $M_{m \times n} \in \mathbb{C}^{m \times n}$ represents a complex matrix with m rows and n columns. I_n and 0_n respectively denote the identity and zero matrices of size n. The dimension of a matrix, shown as a subscript, may be eliminated to simplify the notation. The trace of a matrix M is denoted as $Tr(M)$ and its minimum and maximum singular values are denoted as $\underline{\sigma}(M)$ and $\bar{\sigma}(M)$, respectively. M^* represents the complex conjugate transpose of M. The matrix inequalities are shown with $\succ$ and $\prec$.

The proposed estimation, identification and control algorithms in this dissertation are all considered to be in the discrete time domain. Therefore, the transfer functions are represented either in the z-domain or the frequency domain. $G_{m \times n}(z)$ and $G_{m \times n}(e^{j\omega})$ represent the transfer function $G_{m \times n}$ in the z-domain and the frequency domain, respectively. Moreover, the subscript $m \times n$ indicate that the transfer function has n inputs and m outputs. The notations for the transfer function dimensions, z-domain and frequency domain may be eliminated to simplify the notations. $\mathbb{R}_p^{m \times n}$ denotes the class of all rational causal transfer
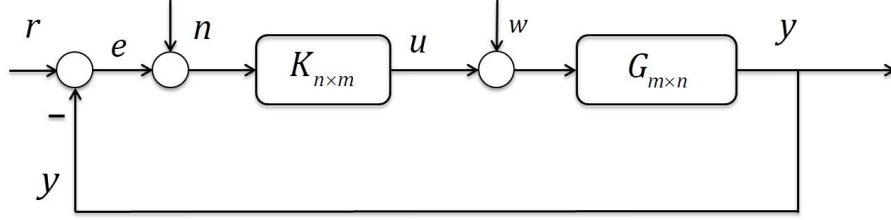
Figure 1.1: The closed loop block diagram. The plant and controller can be either represented in the z-domain or the frequency domain.

functions with m outputs and n inputs. $\mathbb{R}_{p,q}^{m \times n}$ denotes the same class of transfer functions as $\mathbb{R}_p^{m \times n}$ with order q. $\mathbb{RH}_\infty^{m \times n}$ denotes the class of all asymptotically stable rational proper transfer functions with m outputs and n inputs.

The well-known stable factorization results [64] are used to factorize the plant and controller. Consider the feedback system in Fig. 1.1, and assume that a negative feedback controller $K_{n \times m} \in \mathbb{R}_p^{n \times m}$ is designed, which stabilizes the plant $G_{m \times n} \in \mathbb{R}_p^{m \times n}$. The plant and controller can respectively be represented by the factorizations

$$G_{m \times n} = N_{m \times n} M_{n \times n}^{-1}, \tag{1.1}$$
$$G_{m \times n} = \tilde{M}_{m \times m}^{-1} \tilde{N}_{m \times n}, \tag{1.2}$$

and

$$K_{n \times m} = X_{n \times m} Y_{m \times m}^{-1}, \tag{1.3}$$
$$K_{n \times m} = \tilde{Y}_{n \times n}^{-1} \tilde{X}_{n \times m}, \tag{1.4}$$

where $M_{n \times n} \in \mathbb{RH}_\infty^{n \times n}$, $\tilde{M}_{m \times m} \in \mathbb{RH}_\infty^{m \times m}$, $N_{m \times n} \in \mathbb{RH}_\infty^{m \times n}$, $\tilde{N}_{m \times n} \in \mathbb{RH}_\infty^{m \times n}$, $X_{n \times m} \in \mathbb{RH}_\infty^{n \times m}$, $\tilde{X}_{n \times m} \in \mathbb{RH}_\infty^{n \times m}$, $Y_{m \times m} \in \mathbb{RH}_\infty^{m \times m}$ and $\tilde{Y}_{n \times n} \in \mathbb{RH}_\infty^{n \times n}$ are all stable transfer functions. These transfer functions can be obtained such that they satisfy the double Bezout identities given in the following equations

$$\begin{bmatrix} \tilde{Y}_{n \times n} & \tilde{X}_{n \times m} \\ -\tilde{N}_{m \times n} & \tilde{M}_{m \times m} \end{bmatrix} \begin{bmatrix} M_{n \times n} & -X_{n \times m} \\ N_{m \times n} & Y_{m \times m} \end{bmatrix} = \begin{bmatrix} I & 0 \\ 0 & I \end{bmatrix}, \tag{1.5}$$

$$\begin{bmatrix} M_{n \times n} & -X_{n \times m} \\ N_{m \times n} & Y_{m \times m} \end{bmatrix} \begin{bmatrix} \tilde{Y}_{n \times n} & \tilde{X}_{n \times m} \\ -\tilde{N}_{m \times n} & \tilde{M}_{m \times m} \end{bmatrix} = \begin{bmatrix} I & 0 \\ 0 & I \end{bmatrix}. \tag{1.6}$$

Norms

The infinity norm and the two norm can be defined for transfer functions as well as matrices. The H_∞ and H_2 notations are used to represent the infinity and two norms of transfer functions, and they should not be confused with matrix norms.

The matrix norms are defined by considering a complex matrix $M \in \mathbb{C}^{m \times n}$ with m rows and n columns. Here, the infinity norm and two norm for the matrix M are defined.

- *Infinity norm*: The maximum magnitude column sum of the given matrix.

$$\|M_{m \times n}\|_\infty \overset{\Delta}{=} \max_j \ \sum_{i=1}^{m} |m_{ij}| \tag{1.7}$$

where m_{ij} represents the element in row i and column j of the matrix M. If the matrix has only one row, the infinity norm will be the maximum magnitude of the matrix entries.

- *Two norm*: The maximum singular value of the matrix.

$$\|M_{m \times n}\|_2 \overset{\Delta}{=} \bar{\sigma}(M). \tag{1.8}$$

The transfer function norms are defined considering a transfer function $H_{m \times n}(e^{j\omega})$ with m outputs and n inputs in the frequency domain, where $\omega \in \Omega$ and $\Omega = (-\pi, \pi]$. Here, the infinity norm and two norm for the transfer function $H_{m \times n}$ are defined.

- *Infinity norm also known as H_∞ norm*: The supremum of the largest singular value of the transfer function $H_{m \times n}(e^{j\omega})$ across the entire frequency region.

$$\|H_{m \times n}\|_\infty \overset{\Delta}{=} \sup_{\omega \in \Omega} \bar{\sigma}(H_{m \times n}(e^{j\omega})) \tag{1.9}$$

where $\bar{\sigma}(.)$ denotes the largest singular value of the matrix $H_{m \times n}(e^{j\omega})$. According to Eq. (1.8), the H_∞ norm definition in Eq. (1.9) can also be written as follows

$$\|H_{m \times n}\|_\infty \overset{\Delta}{=} \sup_{\omega \in \Omega} \left\|H_{m \times n}(e^{j\omega})\right\|_2. \tag{1.10}$$

In the case of SISO systems, the largest singular value is equivalent to the magnitude of the frequency response, and the H_∞ norm definition can be simplified as

$$\|H_{1 \times 1}\|_\infty \overset{\Delta}{=} \sup_{\omega \in \Omega} \left|H_{1 \times 1}(e^{j\omega})\right|. \tag{1.11}$$

According to Eq. (1.9), the H_∞ norm of a system will be helpful in the control design process to constrain the maximum singular value of the system. Moreover in the case of the SISO system in Eq. (1.11), the maximum magnitude of the system can be directly constrained.

- *Two norm also known as H_2 norm*: The H_2 norm is a representative for the system energy and is defined as

$$\|H_{m \times n}\|_2^2 \overset{\Delta}{=} \frac{1}{2\pi} \int_\Omega \text{Tr}[H_{m \times n}^*(e^{j\omega}) H_{m \times n}(e^{j\omega})] \ d\omega \tag{1.12}$$

In the case of SISO systems, the term inside the trace is a scalar, and the H_2 norm is defined as follows

$$\|H_{1\times 1}\|_2^2 \triangleq \frac{1}{2\pi} \int_\Omega \left| H_{1\times 1}(e^{j\omega}) \right|^2 \; d\omega. \tag{1.13}$$

According to the Parseval's relation[72], the H_2 norm of a transfer function is equal to the square root of the variance of the transfer function output in the time domain, if the input to the transfer function is zero mean white noise with a unit variance. Therefore, the H_2 norm is a useful criteria for constraining the variance of stochastic signals in the time domain.

Chapter 2

Hard Disk Drive (HDD) Servo Systems

2.1 Introduction

Everyday more than 2.5 Exabytes[1] of data are produced. The Hard Disk Drives (HDDs) and the Solid State Drives (SSDs) are the primary devices used for storing these massive amount of data. SSDs have been successful in personal computers markets, because they are significantly faster than the traditional HDDs. However, HDDs are still the dominating data storage devices in the data centers all around the world because of their reliability and cost effectiveness.

Fig. 2.1 shows the amount of data stored in data centers worldwide from 2015 to 2020 in Exabytes of data. As one can notice, the amount of stored data in data centers is increasing exponentially. Therefore, the demand for the enterprise level HDD market will be growing, despite the decay in the personal computers market. HDDs with high storage capacity and improved reliability and performance are necessary to supply the data center market demands.

In this chapter, the servo structure of the HDD is described first. Then, the feedback structure used for controlling this servo structure is introduced.

2.2 Hard Disk Drive Structure

The structure of a HDD is shown in Fig. 2.2. Data are stored on a rotating magnetic disk. This disk is rotating with a constant angular speed, and there is a head moving along the radius to read/write data on the disk. These data are stored in relatively tinny circular tracks called data tracks, where their width can be smaller than 100 nm. Therefore, accurate positioning of the head on data tracks is essential for a reliable HDD performance.

---

[1]One Exabyte is one billion Gigabytes of data.
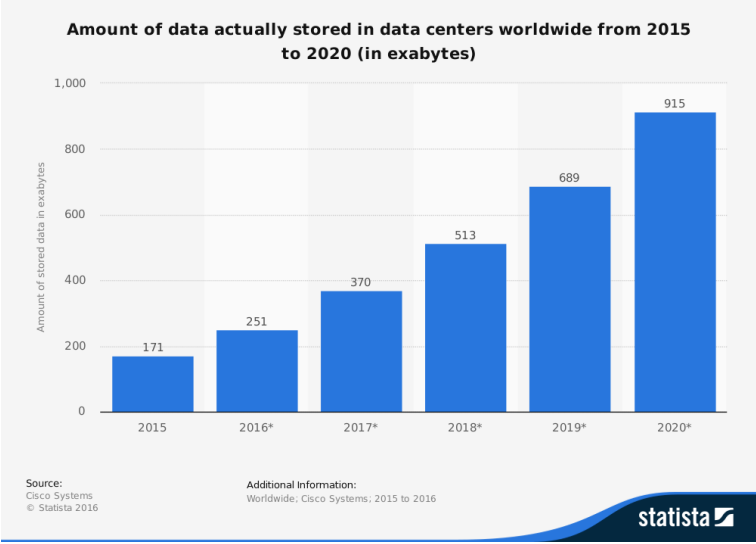
Figure 2.1: This statistic provides a forecast of the actual amount of data stored by data centers worldwide, from 2015 to 2020. Adapted from [63] with permission.
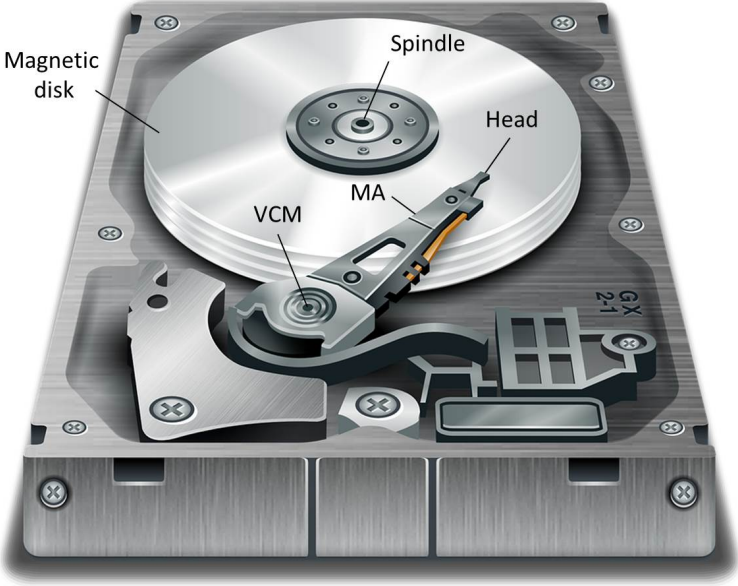
Figure 2.2: The structure of a dual-stage HDD.
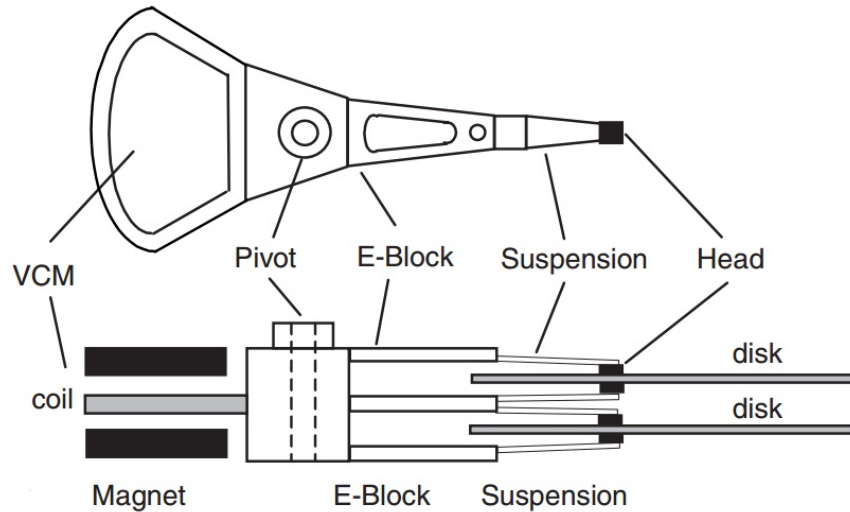
Figure 2.3: The structure of a dual-stage HDD servo assembly. Adapted from [34] with permission.

As shown in Fig. 2.2, the state of the art for nano-positioning the head on the tracks is to use the dual-stage actuation. The dual-stage HDD is composed of two actuators, the Voice Coil Motor (VCM) and a piezoelectric actuator called the Mili-Actuator (MA). These two actuators are located in the HDD servo assembly shown in Fig. 2.3. The E-block is the main structure of the servo assembly and is connected to the VCM directly. This block is extended through a flexible structure called the suspension. The suspension is a flexible structure designed to avoid any contact between the magnetic disk and the servo assembly. Finally, the head is attached to the suspension through a solid structure called the slider.

The magnetic field inside the VCM creates rotational movement around the pivot point shown in Fig. 2.3. This actuator is capable of having a large range of movements and is used for coarse positioning at lower frequency regions. In dual-stage actuations, the MA can be used to either move the suspension or the slider. The former configuration is called the *suspension-actuated*, while the later one is called the *slider-actuated* configuration. In both of these configurations, the MA creates translational movements along the disk radius, which is used in the fine positioning of the head on data tracks. The MA has limited range of movements and is used at higher frequency regions.

The read/write head will also be used as a sensor to measure the head position on the magnetic disk. There are servo patterns written at each circular track of the magnetic disk, and the head can measure its position relative to those servo patterns. Therefore, the head can measure its position relative to circular data tracks. This measurement is called the Position Error Signal (PES).
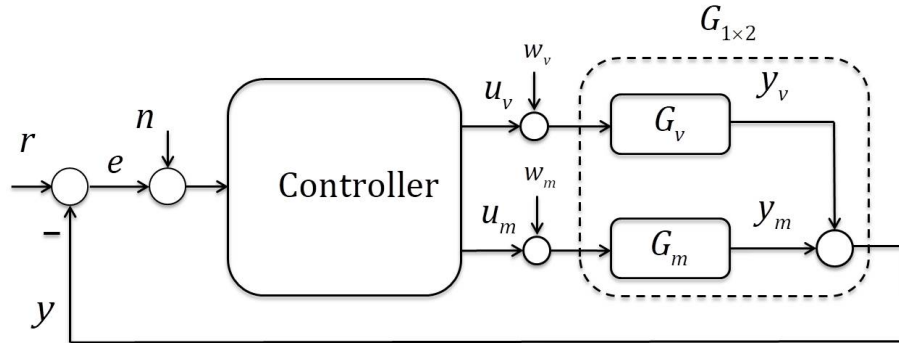
Figure 2.4: The feedback structure for a dual-stage HDD.

2.3 Hard Disk Drive Controls

The general feedback structure used for designing the controllers in dual-stage HDDs is shown in Fig. 2.4. The two actuators used in the HDD structure will receive their individual control inputs, however only the overall movement of the head relative to the center of the data track, which is generally known as PES, can be measured. Therefore, the system is a Multi Input-Single Output (MISO) system and the controller will be a Single Input-Multi Output (SIMO) block.

The high rotational speed of the disk will create air flow inside the disk. This air flow tends to move the head and act as a disturbance on the actuators. In HDD terminology, the air flow disturbance input is called the *windage*. The windage along with external vibrations and other disturbances can deteriorate the performance of the HDD. As shown in Fig. 2.4, these noises can be modeled as run-out, r, measurement noise, n and control input noises, w_v and w_m.

The data are written on circular tracks, as shown with red dotted circles in Fig. 2.5. Therefore, during the read/write process, the actuators should reject the disturbances and try to keep the head on the desired track. The controller used for keeping the head on the desired track is called the *track following* controller and is shown in Fig. 2.5a. This process requires high-precision positioning control, since the track width can be smaller than 100 nm.

In order to move the head from one track to another, track seeking and settling processes are used. These two processes are shown in Figs. 2.5b and 2.5c, respectively. The track seeking process will use VCM as the actuator and move the head toward track B as fast as possible. As the head gets close to the track B, the controller is switched to the track settling controller, which uses the VCM and MA to settle the head on track B as fast as possible. After settlement of the head on track B, the track following control is used to read or write data on this track.

The state of the art for designing the track following controller in a dual-stage HDD is to use the sensitivity decoupling design methodology. This methodology decouples the system into two Single Input-Single Output (SISO) systems and designs the controller for

(a) Track following

(b) Track seeking

(c) Track settling
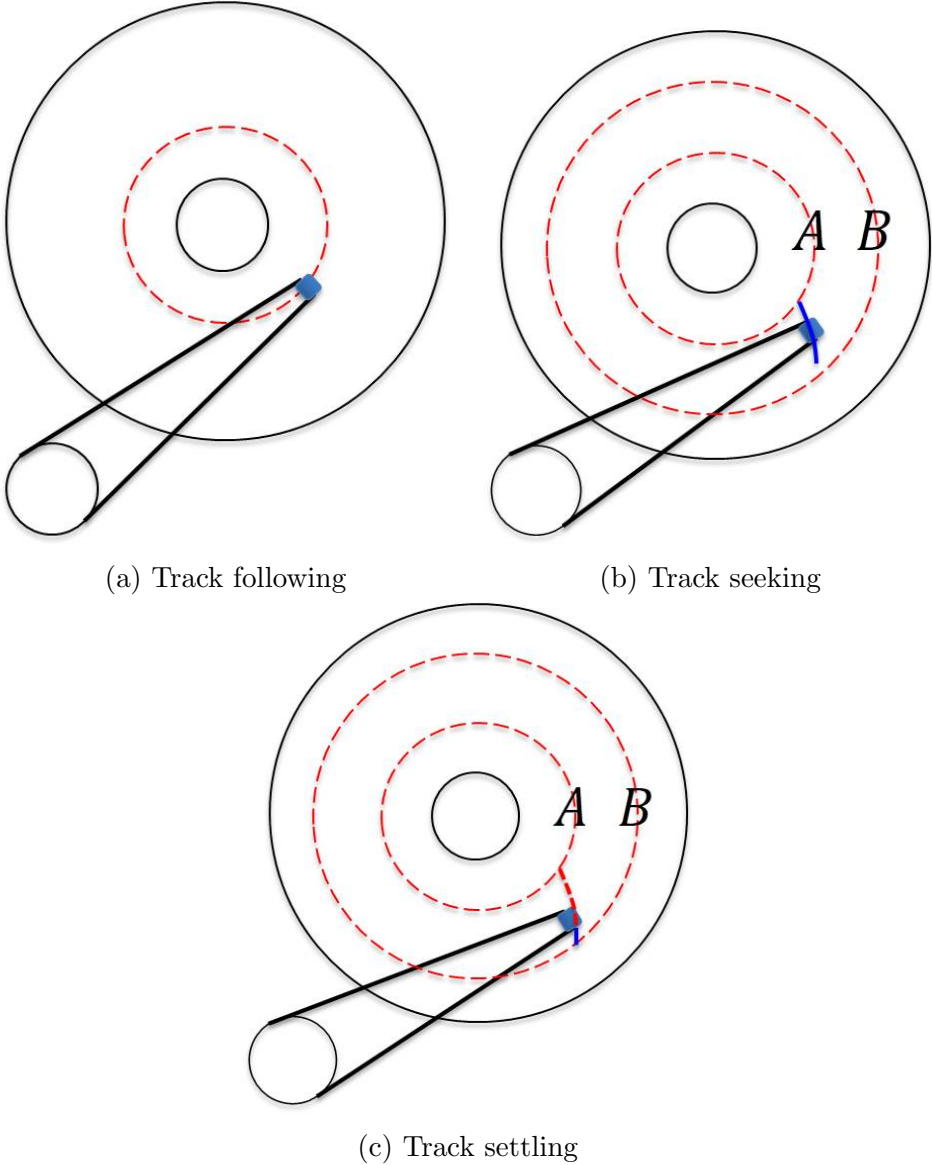
Figure 2.5: Three types of actuator controls used in HDDs for reading or writing data on data tracks. The data tracks are shown with red dotted lines and the blue square is representing the read/write head with exaggerated dimension.
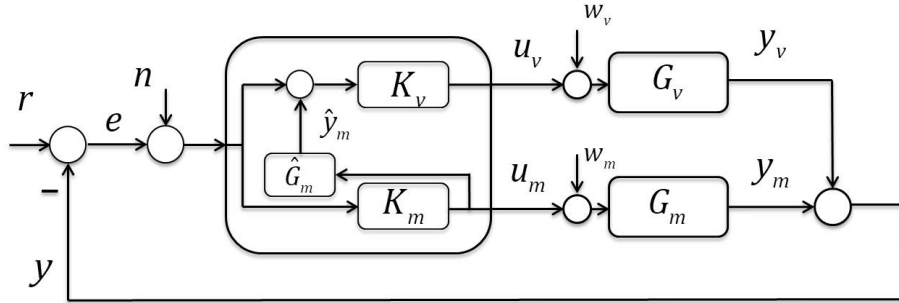
Figure 2.6: Sensitivity decoupling control structure. $\hat{G}_m(z)$ represents the estimated MA transfer function.

each actuator individually.

Sensitivity Decoupling Design Method

The sensitivity decoupling control design method is proposed for the dual-stage HDD control design [1, 34, 45, 51]. The control block diagram for this structure is shown in Fig. 2.6. In the sensitivity decoupling control structure, the estimated model of the MA plant, $\hat{G}_m(z)$, is used inside the control structure in order to decouple the sensitivity of the VCM loop from the MA loop. The overall sensitivity transfer function from the external signal r to e is given by

$$S_r(z) = \frac{1}{1 + K_m(z)G_m(z) + K_v(z)G_v(z)(1 + K_m(z)\hat{G}_m(z))}. \tag{2.1}$$

This overall sensitivity function can also be written as

$$S_r(z) = \frac{1}{1 + K_v(z)G_v(z)} \cdot \frac{1}{1 + K_m(z)\bar{G}_m(z)}, \tag{2.2}$$

where the modified MA plant, $\bar{G}_m(z)$, is derived using the following equation

$$\bar{G}_m(z) = \frac{G_m(z) + K_v(z)G_v(z)\hat{G}_m(z)}{1 + K_v(z)G_v(z)}, \tag{2.3}$$

or equivalently

$$\bar{G}_m(z) = G_m(z) + \frac{K_v(z)G_v(z)(\hat{G}_m(z) - G_m(z))}{1 + K_v(z)G_v(z)}. \tag{2.4}$$

The MA has high frequency uncertainties. Therefore, the estimated model of the MA , $\hat{G}_m(z)$, is a good approximation for the MA plant, $G_m(z)$, in low frequency regions and as a result $\bar{G}_m(z)$ will be very close to $G_m(z)$ in those low frequency regions. In the high frequency regions, the $K_v(z)G_v(z)$ term is relatively small since the VCM is not active in that region. Consequently, any difference between $\hat{G}_m(z)$ and $G_m(z)$ at high frequency regions will be

decreased by the $K_v(z)G_v(z)$ term, and the $\bar{G}_m$ will also be a good approximation of $G_m(z)$ at high frequency regions. Therefore, the overall sensitivity of the dual-stage actuation in Eq. (2.1) can be approximately decoupled as the multiplication of the actuators' sensitivity transfer functions

$$S_r(z) = S_{r,v}(z).S_{r,m}(z), \tag{2.5}$$

where

$$S_{r,v}(z) = \frac{1}{1 + K_v(z)G_v(z)}, \tag{2.6}$$

$$S_{r,m}(z) = \frac{1}{1 + K_m(z)G_m(z)}. \tag{2.7}$$

In HDD control design, the sensitivity transfer function which denotes the closed loop transfer function from the track run-out, r, to the PES, e, is one of the most important transfer functions to consider in the design process, since it describes the level of attenuation that the track-following servo system is able to attenuate. In the sensitivity decoupling design methodology, the overall attenuation provided by the feedback system can be approximated as a loop series combination of attenuation provided by the VCM and the MA loops [45]. Therefore, $K_v(z)$ and $K_m(z)$ can be individually designed, since their effects on the sensitivity transfer function is decoupled according to Eq. (2.5). As a result, shaping individual sensitivity of each transfer function will shape the overall sensitivity transfer function.

The controller obtained using the sensitivity decoupling structure can guarantee the stability of each individual loop as well as the stability of the overall dual-stage actuation. The advantage of guaranteeing the stability of single loops is that, in the case of MA failure, the dual-stage HDD can be converted to a single-stage HDD, where the single-stage loop is stable and working with degraded performance compared to the dual-stage HDD.

Chapter 3

Observer Design for Non-uniform Sampled HDD Servos

The servo patterns written on the HDD magnetic disk are used as a reference to measure the head position. In the self-servo writing procedure, the HDD head is used to write these servo patterns in a few consecutive steps [13, 16]. One of these steps is called the spiral self-servo writing [22], where the seek movement of the head with constant speed will create a spiral path. As a result of this movement, the head will arrive at the previously written circular servo patterns in non-uniform time intervals. Therefore, the head position is measured with irregular sampling time. However, the control inputs to the actuators should be updated at regular sampling time. In this chapter, it is proposed to design an observer which can estimate the states of this system with the same sampling time as the control inputs. Therefore, the estimated states can be directly used to generate the control inputs.

The proposed observer should deal with uniform sampled control inputs and non-uniform sampled measurements. The non-uniformity in the measurement sampling time is modeled as plant dynamics variations in section 3.1. An observer structure which can estimate system states at uniform sampled time is introduced for this varying plant in section 3.2. The observer gain for this structure is designed using the gain-scheduling method and its performance as well as its computational complexity will be evaluated in comparison with a Kalman filter under several different noise scenarios. Section 3.3 will compare the simulation results for these two types of observers.

3.1 Modeling

A special case of non-uniform sampled systems given in Fig. 3.1 is considered in this chapter. It is assumed that the system is excited with uniform-sampled control inputs with the interval of T_c, and that measurements are arriving at non-uniform time intervals. These measurements can arrive anytime between two consecutive control updates. The parameter
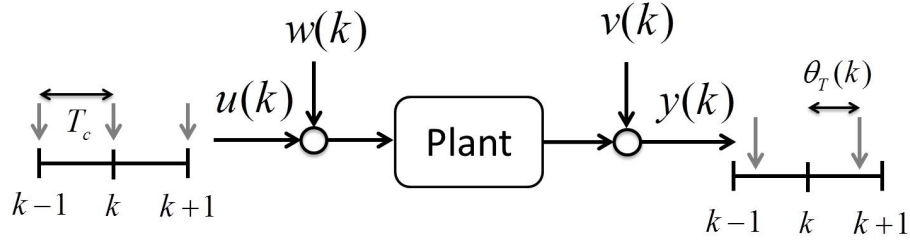
Figure 3.1: The system with non-uniform-sampled measurements. $w(k)$ and $v(k)$ represent the control input disturbance and measurement noise, respectively.

θ_T represents the delay in the measurement arrival for the sampling interval k.

$$0 \leq \theta_T(k) \leq T_c \tag{3.1}$$

If the value of $\theta_T(k)$ for all the sampling intervals is zero, the measurements are arriving at uniformed-sampled time intervals without any delay.

In order to obtain the discrete-time model of the system given in Fig. 3.1, it is assumed that the continuous model of the system is known. This continuous model is represented as

$$\dot{x}(t) = A^c x(t) + B_u^c u(t) + B_w^c w(t)$$
$$y(t) = C^c x(t) + D_u^c u(t) + D_w^c w(t) + v(t) \tag{3.2}$$

where $x(t)$, $u(t)$ and $y(t)$ represent the internal state of the system, control input and measurement output in the continuous time-domain.

The given continuous time model can be discretized with the sampling time τ.

$$x(k + 1) = A^d(\tau) x(k) + B_u^d(\tau) u(k) + B_w^d(\tau) w(k)$$
$$y(k) = C^d x(k) + D_u^d u(k) + D_w^d w(k) + v(k) \tag{3.3}$$

where the discretized model for the state-update equation can be computed as

$$A^d(\tau) = e^{A^c \tau}$$
$$B_u^d(\tau) = \int_{\lambda=0}^{\tau} e^{A^c \lambda} B_u^d d\lambda \tag{3.4}$$
$$B_w^d(\tau) = \int_{\lambda=0}^{\tau} e^{A^c \lambda} B_w^d d\lambda$$

and the discretized model for the output equation is computed as

$$C^d = C_u^c$$
$$D_u^d = D_u^c \tag{3.5}$$
$$D_w^d = D_w^c.$$

It is worth mentioning that the parameters of the output equation for the discrete-time model will be the same as the continuous time model. However, the parameters of the state-update equation for the discrete-time model depends on the sampling time τ.

The discretized model of the system in Fig. 3.1 is obtained under the assumption that the state of the system is updated with the uniform sampling time of the control inputs. Therefore, the state-update equation can be derived as

$$x(k+1) = A^d(T_c)x(k) + B_u^d(T_c)u(k) + B_w^d(T_c)w(k). \tag{3.6}$$

In order to obtain the discretized output equation, the state of the system at the instance of measurement arrival is computed as

$$x(\theta_T) = A^d(\theta_T)x(k) + B_u^d(\theta_T)u(k) + B_w^d(\theta_T)w(k). \tag{3.7}$$

Also, the output of the system at that instance can be computed as

$$y(\theta_T) = C^d x(\theta_T) + D_u^d u(k) + D_w^d w(k) + v(k). \tag{3.8}$$

Therefore by using Eq. (3.7) and (3.8), the discretized output equation of the system will be written as

$$y(\theta_T) = C^d A^d(\theta_T)x(k) + (C^d B_u^d(\theta_T) + D_u^d)u(k) + (C^d B_w^d(\theta_T) + D_w^d)w(k) + v(k). \tag{3.9}$$

Eq. (3.6) and (3.9) represent the state-update and output equation for the discretized model given in Fig. 3.1. As one can notice, the state-update equation is not a function of delay in the measurement arrival, θ_T, and this delay is modeled to affect the output equation given in Eq. (3.9). Therefore using Eqs. (3.6) and (3.9), the plant dynamics can be written as

$$\begin{aligned} x(k+1) &= Ax(k) + B_u u(k) + B_w w(k) \\ y(k) &= C(k)x(k) + D_u(k)u(k) + D_w(k)w(k) + v(k) \end{aligned} \tag{3.10}$$

where

$$A = A^d(T_c), \quad B_u = B_u^d(T_c), \quad B_w = B_w^d(T_c) \tag{3.11}$$

and

$$\begin{aligned} C(k) &= C^d A^d(\theta_T(k)) \\ D_u(k) &= C^d B_u^d(\theta_T(k)) + D_u^d \\ D_w(k) &= C^d B_w^d(\theta_T(k)) + D_w^d. \end{aligned} \tag{3.12}$$

3.2 Observer Design

The non-uniform sampled system modeled in the previous section has the control input with regular sampling time and the measurement output with irregular sampling time. In order
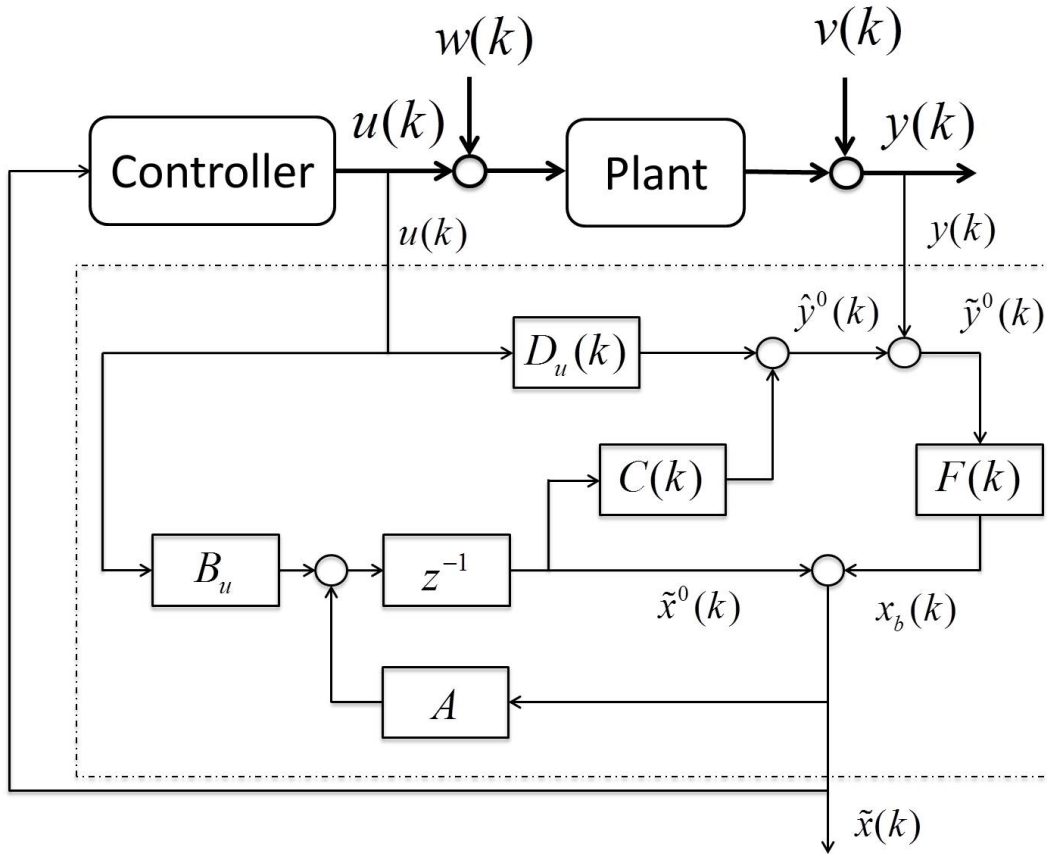
Figure 3.2: Observer structure for both Kalman filtering and Gain-scheduling techniques.

to be able to use the measurement output as a feedback signal for generating the control inputs, it is proposed to design an observer. This observer is used to estimate the plant states with uniform sampling time, given uniform sampled control input and non-uniform sampled measurements.

The structure used to design this observer is given in Fig 3.2. In this structure, the only unknown is the observer gain $F(k)$. *Kalman filtering* and *Gain-scheduling* techniques are the two methodologies which will be considered to design this observer gain.

The structure of the observer in Fig. 3.2 uses both the a-priori and a-posteriori state estimations. The a-priori state estimate $\hat{x}^0(k)$ is obtained using the measurements up to time step $k-1$, while the a-posteriori state estimate $\hat{x}(k)$ is obtained using the measurements up to time step k. The estimation errors for the a-priori state estimate, $\hat{x}^0(k)$, a-posteriori state

estimate, $\hat{x}(k)$, and the a-priori output estimate, $\hat{y}^0(k)$ are defined as follows.

$$
\begin{aligned}
\tilde{x}^0(k) &= x(k) - \hat{x}^0(k), \\
\tilde{x}(k) &= x(k) - \hat{x}(k), \\
\tilde{y}^0(k) &= y(k) - \hat{y}^0(k).
\end{aligned}
\tag{3.13}
$$

Kalman Filter

The structure of the observer shown in Fig. 3.2 is the Kalman filter structure. The Kalman filtering technique will find the optimal observer gain $F(k)$ at each time step which minimizes the trace of a-posteriori state estimation error covariance defined as

$$
J(k) = Tr[Z(k)],
\tag{3.14}
$$

where $Z(k)$ represents the a-posteriori state estimation error covariance and is defined as

$$
Z(k) = E[\ (x(k) - \hat{x}(k))(x(k) - \hat{x}(k))^T \ \mid y_k, .., y_0 \ ].
\tag{3.15}
$$

E, Tr and T are the symbols for the expectation, trace and transpose, respectively. The notation $\mid y_k, .., y_1$ is used to represent the knowledge of measurement up to time instance k.

The Kalman filter computes the optimal observer gain given the variance of input disturbance, W and measurement noise, V. The optimal Kalman filter gain is computed using the following equation[40].

$$
F(k) = M(k)C'(k)[C(k)M(k)C'(k) + D_w(k)WD'_w(k) + V]^{-1}
\tag{3.16}
$$

where $M(k)$ represents the a-priori estimation error covariance, and is defined as follows

$$
M(k) = E[\ (x(k) - \hat{x}(k))(x(k) - \hat{x}(k))^T \ \mid y_{k-1}, .., y_0 \ ].
\tag{3.17}
$$

The a-priori estimation error covariance is computed using the following iterative equation

$$
\begin{aligned}
M(k+1) &= AM(k)A' + B_w(k)WB'_w - ... \\
(AM(k)C'(k))&[C(k)M(k)C'(k) + D_w(k)WD'_w(k) + V]^{-1}(AM(k)C'(k))'.
\end{aligned}
\tag{3.18}
$$

Gain-Scheduling Observer

The gain-scheduling is a feedback design methodology used for systems with known dynamics variations[23, 24]. In this methodology, first the dynamics variation is modeled as a function of a varying parameter called the scheduling parameter. Then, the gain-scheduling methodology considers the plant dynamics variation in the design step and obtains a feedback loop as a function of the scheduling parameter.

The plant dynamics represented in Eq. (3.10) is a function of the scheduling parameter, θ_T. The objective is to design the observer as a function of this scheduling parameter such
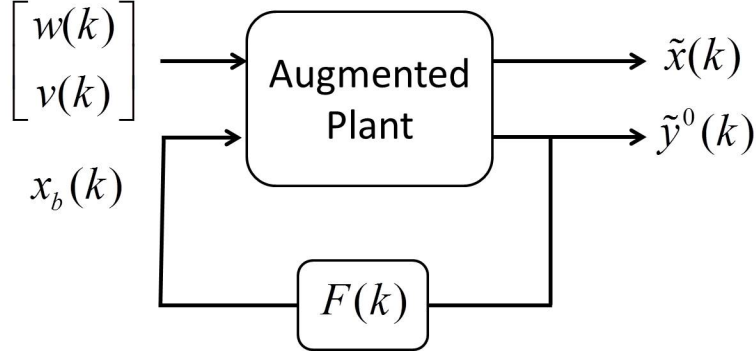
Figure 3.3: The augmented plant for the observer strucutre given in Fig. 3.2.

that the H_2 or H_∞ norm of the transfer function from disturbances, $w(k)$ and $v(k)$, to the estimation error is minimized.

The structure considered for the observer is the same as the Kalman filter structure shown in Fig. 3.2. Since the only unknown parameter is the observer gain $F(k)$, all the known blocks in Fig. 3.2 will be augmented into one block known as the augmented plant in Fig. 3.3. Considering the transfer function $T^{\tilde{x}}_{w,v}$ from disturbances w and v to the a-posteriori estimation error $\tilde{x}$, the observer gain $F(k)$ will be designed to minimize either H_2 or H_∞ norm of this transfer function.

The augmented plant model is obtained by considering the relations between blocks in Fig. 3.2. The a-priori state estimate will evolve as a function of the a-posteriori state estimate and control input.

$$\hat{x}^0(k + 1) = A\hat{x}(k) + B_u u(k) \tag{3.19}$$

and the a-posteriori state estimate will be obtained as summation of a-priori state estimate and the state-update term, $x_b(k)$

$$\hat{x}(k) = \hat{x}^0(k) + x_b(k), \tag{3.20}$$

where the state-update term is defined as follows

$$x_b(k) = F(k)\tilde{y}^0(k). \tag{3.21}$$

Considering the definition of a-priori and a-posteriori estimation error given in Eq. (3.13), Eqs. (3.19) and (3.20) will result in

$$\tilde{x}^0(k + 1) = A\tilde{x}(k) + B_w w(k) \tag{3.22}$$

and

$$\tilde{x}(k) = \tilde{x}^0(k) - x_b(k). \tag{3.23}$$

The equation for updating the a-priori state estimation error is obtained by combining Eqs. (3.22) and (3.23)

$$\tilde{x}^0(k + 1) = A\tilde{x}^0(k) + B_w w(k) - Ax_b(k). \tag{3.24}$$

The a-priori output estimation is computed based on the a-priori state estimation and the control input

$$\hat{y}^0(k) = C(k)\hat{x}^0(k) + D_u(k)u(k). \tag{3.25}$$

Considering the estimation error for the a-priori output defined in Eq. (3.13) and the output equation defined in Eq. (3.10), Eq. (3.25) will result in

$$\tilde{y}^0(k) = C(k)\tilde{x}^0(k) + D_w(k)w(k) + v(k). \tag{3.26}$$

Therefore, the state-space model for the augmented plant in Fig. 3.3 will be derived using Eqs. (3.23), (3.24) and (3.26).

$$\begin{bmatrix} \tilde{x}^0(k+1) \\ \tilde{x}(k) \\ \tilde{y}^0(k) \end{bmatrix} = \begin{bmatrix} A & B_w & 0 & -A \\ I & 0 & 0 & -I \\ C(k) & D_w(k) & I & 0 \end{bmatrix} \begin{bmatrix} \tilde{x}^0(k) \\ w(k) \\ v(k) \\ x_b(k) \end{bmatrix} \tag{3.27}$$

According to Eq. (3.12), the augmented plant dynamics in Eq. (3.27) is a function of the measurement time delay, θ_T. Therefore, the observer gain $F(k)$ in Fig. 3.3 is obtained as a function of θ_T using the synthesis techniques presented in [24] by using Linear Matrix Inequalities (LMIs). These LMIs have been defined in *Theorem 8 and 9* of [24] to respectively minimize H_∞ and H_2 norm of the a-posteriori state estimation error from disturbances w and v.

The functionality of the observer gain $F(k)$ on scheduling parameter θ_T is usually considered to be similar to the functionality of the plant on θ_T. However, more complex functionality can also be considered to achieve a smaller state estimation error. As an example, if the plant dynamics is a quadratic function of θ_T, the parameter $F(\theta_T)$ is also considered to be a quadratic function of θ_T

$$F(\theta_T) = F_2\theta_T^2 + F_1\theta_T + F_0. \tag{3.28}$$

The observer gain coefficients in Eq. (3.28) are obtained offline using LMIs proposed in [24]. Once these coefficients are known, the implementation of the gain-scheduling observer will be relatively fast compared to the Kalman filter gain computation given in Eqs. (3.16) and (3.18). The Kalman filter gain requires matrix inversion and also higher number of multiplications which makes it computationally less efficient compared to the gain-scheduling observer. However the solution to the Kalman filter will be optimal in terms of minimizing trace of a-posteriori state estimation error covariance given in Eq. (3.14), while the gain-scheduling observer is a sub-optimal solution.

3.3 Simulation Results

The proposed observer design methods for the non-uniform sampled systems are applied to the self servo writing process in hard disk drives, where there is non-uniformity in the

Table 3.1: The relative percentage for the trace of state estimation error covariance (gain-scheduling observer relative to the Kalman filter) given in Eq. (3.31). The time domain simulations were run for 5 seconds with sampling time $T_c = 70\ \mu s$.

$V_{simulation}$ \\ V_{design}	10^{-4}	10^{-2}	1
10^{-4}	120 %	75 %	91 %
10^{-2}	173 %	109 %	92 %
1	186 %	153 %	116 %

measurement sampling time as described in Fig. 3.1. The self-servo writing process is a low frequency process, at which VCM is only used as an actuator. This process mainly uses the VCM at low frequency regions, therefore a simple double integrator is considered for the VCM model. It is possible to consider more complex model at the cost of having more offline computations for obtaining the observer gain.

A double integrator in the continuous time is discretized according to Eq. (3.10)

$$A = \begin{bmatrix} 1 & T_c \\ 1 & 0 \end{bmatrix}, B_u = B_w = \begin{bmatrix} T_c^2/(2J) \\ T_c/J \end{bmatrix}, \tag{3.29}$$

$$C(k) = \begin{bmatrix} 1 & \theta_T(k) \end{bmatrix}, D_u(k) = D_w(k) = \begin{bmatrix} \theta_T(k)^2/(2J) \end{bmatrix}, \tag{3.30}$$

where J is the VCM inertia. T_c and θ_T represent sampling time and measurement arrival delay in Fig. 3.1.

Gain-scheduling and Kalman filters are designed using the observer structure given in Fig. 3.2. The performance of the designed gain-scheduling observer is compared with the optimal Kalman filter in terms of trace of covariance matrix for the a-posteriori state estimation error given in Eq. (3.14). Also, the plot of state estimation error in the time domain are compared among two methods.

The observer design is a function of the relative variance of input disturbance W and measurement noise V. Therefore, the observers are designed based on different values of the variance V by assuming $W = 1$. These noises are considered to be white in this example. However, colored noises can be considered by augmenting the noise model into the plant model. This augmentation will create more complex augmented plant model and has significant effects on offline computation for the gain-scheduling observer and online computation for the Kalman filter.

The trace of state estimation error covariance for the gain-scheduling observer relative to the Kalman filter is shown in table 3.1. This value is defined as follows

$$100 \frac{J_{\text{Gain scheduling observer}}}{J_{\text{Kalman filter}}}, \tag{3.31}$$

where $J_{\text{Gain scheduling observer}}$ and $J_{\text{Kalman filter}}$ are the trace of a-posteriori state estimation error covariance for the gain-scheduling and Kalman filters, defined in Eq. (3.14). The observers in each column are designed based on a given variance of measurement noise. However, the simulations were conducted using different variances for the measurement noise, since in physical systems the exact variance of noises may not be known.

The performance of the tuned gain-scheduling observer deviates about 10-20 percent as compared to the tuned Kalman filter. The better performance of the tuned Kalman filter is expected, since the Kalman filter gain is the optimal gain for the given variance of noises. However, if the simulation variance is less than the designed variance, the gain-scheduling observer achieves smaller error covariance compared to the detuned Kalman filter, since the gain-scheduling observer is designed to accommodate noises with the variance of equal or smaller than the designed value. If the simulation noise variance is greater than its designed value, the Kalman filter performs better than the gain-scheduling observer. However, none of these two observers are designed for this magnitude of measurement noise variance.

The time domain simulation results for the case of $V_{disturbance} = V_{design} = 10^{-4}$ in table 3.1 are shown in Fig. 3.4. The original simulation was run for 5 *seconds* with control update rate of 70 μs. However to make the plots visible, the results for a smaller portion of time is sketched in Fig. 3.4. The measurements arrival time relative to the latest control update, θ_T, is shown in the top figure, and the two bottom figures show the a-posteriori states estimation errors. Since the tuned Kalman filter has the optimal gain, the Kalman filter achieves a smaller state estimation error variance compared to the gain-scheduling observer.

The gain-scheduling observer and Kalman filter both use the same observer structure. However, their performance and online computational complexity are different. In terms of performance, if the variance of noise is known in advance, the Kalman filter has relatively better performance compared to the gain-scheduling observer. However, if only the upper bound of the noise variance is known, the gain-scheduling observer will outperform the Kalman filter. In terms of computational complexity, the observer gain $F(k)$ in the Kalman filter, Eq. (3.16), requires relatively more online computations compared to the gain-scheduling observer gain given in Eq. (3.28). The gain-scheduling gain only requires few multiplications, while the Kalman filter gain requires significantly higher number of multiplication as well as a divisions which are computationally expensive.
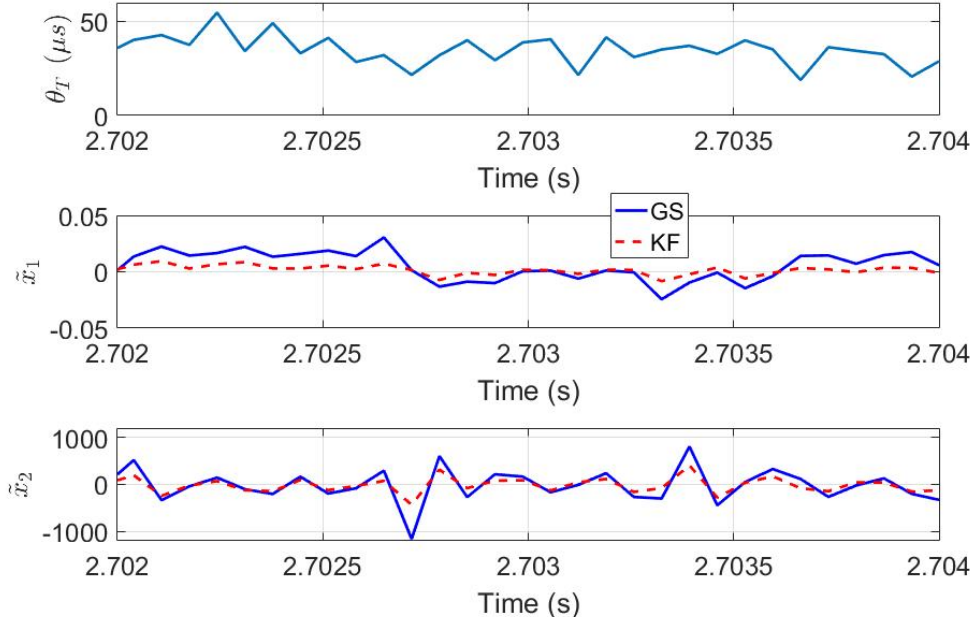
Figure 3.4: Time domain results. The top figure plots the delay in the measurement arrival time, while the other two figures plot the states estimation errors as functions of time.

Chapter 4

Online Identification of HDD Modeling Uncertainties

Temperature variations in HDDs will move system resonance modes which directly affect system dynamics. These variations in system dynamics are identified in an online fashion by coprime factorizations of uncertainties using coprime factorizations [26, 64]. The main reason for factorizing the uncertainties is to avoid unnecessary identification of the unchanged part of the plant dynamics. Therefore, the uncertainty identification, in comparison to the complete plant dynamics identification, will require less computational power as well as smaller order for the identified transfer function.

In section 4.1, the motivation for performing online identification of the closed loop transfer functions in dual-stage HDDs is elaborated. Subsequently, a methodology for plant uncertainty identification is presented in section 4.2. Experimental results are provided in section 4.3, which shows the effectiveness of this algorithm in satisfying the stability criteria for the adaptive RRO following algorithm proposed in [61, 62] for the dual-stage HDDs.

4.1   Motivation

The simplified block diagram of a dual-stage, double input-single output hard disk drive track following servo system is shown in Fig. 4.1. In this figure, $G_{VCM} \in \mathbb{R}_p$ is the voice coil motor, VCM transfer function, while $G_{MA} \in \mathbb{R}_p$ represents the micro-actuator, MA transfer function. u_{vcm} and u_{MA} are respectively the control inputs to the VCM and the MA. r is the track run-out while e is the measured Position Error Signal (PES) of the magnetic hard relative to the center of the data track. n is the non-repeatable run-out. The adaptive RRO following algorithm described in [61] injects signals at u_{VCM}, u_{MA} in order to track the RRO written on the disk. The model of the system from these injection points to e is used for obtaining the RRO tracking control signals. The closed loop block diagrams in this chapter use the negative feedback to close the loops. Let $G = [G_{VCM} \ G_{MA}] \in \mathbb{R}_p^{1 \times 2}$ and
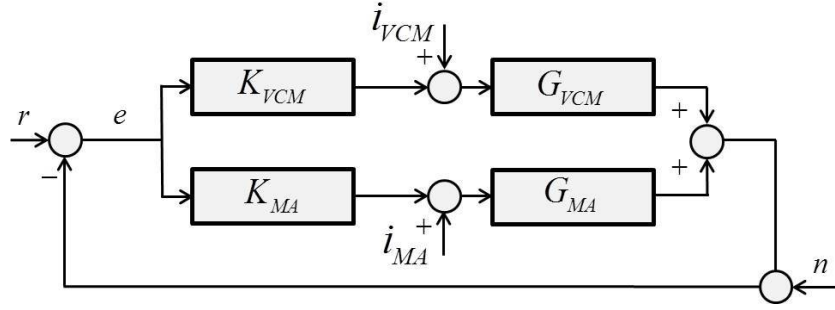
Figure 4.1: Control block diagram for a dual-stage HDD. G_{VCM} and G_{MA} are respectively open-loop plant transfer functions for the voice coil motor and mili-actuator. Also, K_{VCM} and K_{MA} are their corresponding controllers. r and n are respectively representing the repeatable run-out RRO and noises in the system.

$K = [K_{VCM}\ K_{MA}]^T \in \mathbb{R}_p^{2\times1}$, then

$$R = [R_{VCM}\ R_{MA}] = \frac{1}{1+GK}G \in \mathbb{RH}_\infty^{1\times2}. \tag{4.1}$$

$R_{VCM} \in \mathbb{RH}_\infty$ and $R_{MA} \in \mathbb{RH}_\infty$ are respectively two closed-loop sensitivity transfer functions from the VCM and MA injection inputs, u_{VCM} and u_{MA} to the PES e. $\hat{R}_{VCM} \in \mathbb{RH}_\infty$ represents the model estimate of the true transfer function R_{VCM}. Similarly, $\hat{R}_{MA} \in \mathbb{RH}_\infty$ represents the model estimate of the true transfer function R_{MA}.

The adaptive RRO following algorithm introduced in [61, 62] has guaranteed convergence if and only if the frequency response phase differences between the actual transfer functions, R_{VCM}, R_{MA}, and their respective model estimates, $\hat{R}_{VCM}, \hat{R}_{MA}$, are less than 90-degree. More specifically denoting $\angle G(j\omega)$ as the phase of the frequency response of the transfer function $G \in \mathbb{R}_p$, the adaptive RRO following algorithm in [61, 62] converges iff

$$\begin{aligned} \left|\angle(R_{VCM}(j\omega)/\hat{R}_{VCM}(j\omega))\right| &< 90° \text{ and} \\ \left|\angle(R_{MA}(j\omega)/\hat{R}_{MA}(j\omega))\right| &< 90°. \end{aligned} \tag{4.2}$$

We will often refer to Eq. (4.2) as the "90-degree" criteria.

The frequency response measurements of the transfer function $R = [R_{VCM}\ R_{MA}]$ can be used to obtain the nominal model $R_0 = [R_{VCM,0}\ R_{MA,0}]$, such that the 90-degree criteria given by Eq. (4.2) is satisfied. However, temperature variations affect the MA dynamics, resulting in variations in some of its resonance modes. These resonance frequencies variations may cause Eq. (4.2) to be violated, as illustrated in Fig. 4.2. This figure shows the magnitude and phase of the frequency responses for the MA closed-loop sensitivity transfer function R_{MA} at different temperatures, relative to its nominal frequency response at $T = 34°$ *Celsius*. As shown in the figure, there are significant phase variations at the
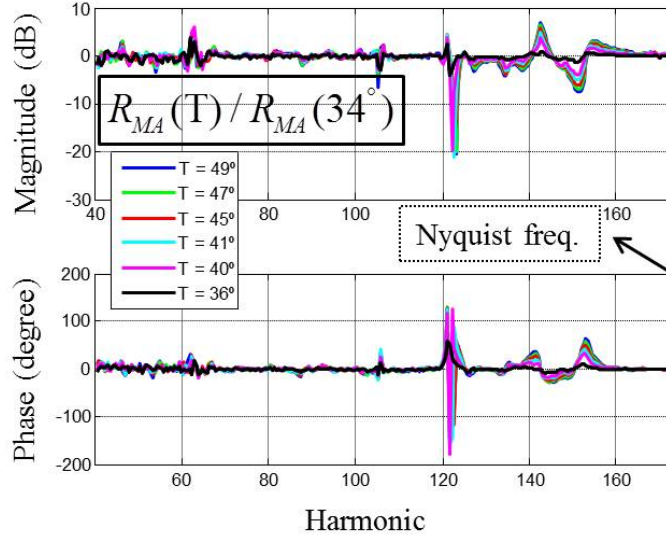
Figure 4.2: The actual frequency responses from the MA injection point to PES signal,e, compared to the one at $T = 34°\ Celsius$.

resonance mode located around harmonic 120 and also in the resonance modes located between harmonics 140 to 160. These variations can violate the 90-degree criteria in Eq. (4.2). Therefore, we need to identify these variations online, and accordingly modify the model $\hat{R}_{MA}$ which must be used in the adaptative RRO following algorithm.

4.2   Methodology

In this section we will parameterize uncertainty due to temperature variations using coprime factorizations [26, 64]. These factorizations are used to parameterize and isolate the uncertainty relative to the plant nominal transfer function in terms of a causal and stable transfer function $S \in \mathbb{RH}_\infty^{1\times2}$. As will be shown subsequently, identification is only required for the uncertain parameterization, S, and not the entire closed-loop transfer function R.

Uncertainty Factorization

The closed-loop feedback system in Fig. 4.1 can be described as shown in Fig. 4.3, where the plants and controllers are defined as

$$G = \left[\begin{array}{cc} G_{VCM} & G_{MA} \end{array}\right] \in \mathbb{R}_p^{1\times2}, \tag{4.3}$$

$$K = \left[\begin{array}{c} K_{VCM} \\ K_{MA} \end{array}\right] \in \mathbb{R}_p^{2\times1}. \tag{4.4}$$
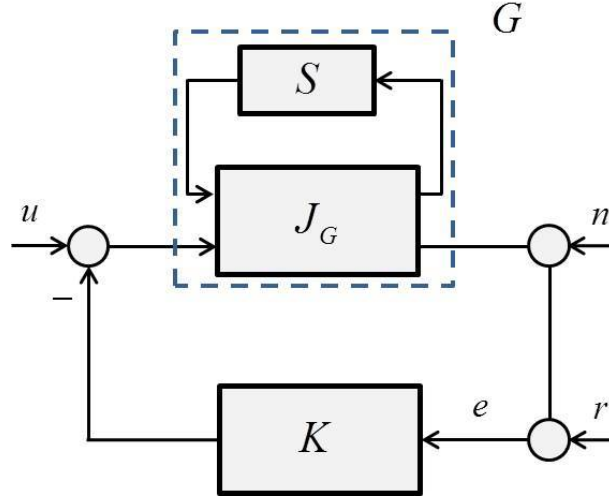
Figure 4.3: Uncertainty factorization in the control block diagram of a dual-stage HDD. J_G represents the nominal factorization of the open-loop plant.

As stated previously, $\mathbb{R}_p^{m \times n}$ denotes the class of rational proper transfer functions and $\mathbb{RH}_\infty^{m \times n}$ denotes the class of all stable, rational proper transfer functions with n inputs and m outputs. Also, $u = [u_{VCM}, \ u_{MA}]^T$ is the injection signal and the stable transfer function $S \in \mathbb{RH}_\infty^{1 \times 2}$ parameterizes the class of all transfer functions $G(S) \in \mathbb{R}_p^{1 \times 2}$ that are stabilized by the feedback controller $K \in \mathbb{R}_p^{2 \times 1}$ [64].

The closed loop transfer function from the injection points u to e is given by

$$R(S) = \frac{1}{1 + G(S)K} G(S), \tag{4.5}$$

where

$$R(S) = [R_{VCM}(S), R_{MA}(S)] \in \mathbb{RH}_\infty^{1 \times 2}. \tag{4.6}$$

The first and second columns are respectively representing the closed-loop transfer functions from VCM and MA injection points to e.

As illustrated in Fig. 4.2, temperature variations affect the MA resonances at high frequencies, which can change the closed-loop transfer functions. Considering the closed-loop transfer functions from the injection points to e, we will make the simplifying assumption that temperature variations will only affect $R_{MA}(S)$ and not R_{VCM}. This assumption is justified by the fact that the control system K_{VCM} is designed in order to not excite the VCM's high frequency resonance modes, which are uncertain and may be affected by temperature variations. Therefore, uncertainty identification is only required for the MA. In other words,

$$R(S) = [R_{VCM}, R_{MA}(S)]. \tag{4.7}$$

In order to identify the uncertainty, we utilize well-known factorization results [64] to characterize plant uncertainty. Consider the feedback system in Fig. 4.3, and assume that

a negative feedback robust controller K is designed, which stabilizes the nominal plant $G_0 \in \mathbb{R}_p^{1 \times 2}$ as well as all possible plant variations in G. According to coprime factorizations of the plant and controller given in Eqs. (1.2)-(1.4), the nominal plant and controller can respectively be represented by the factorizations

$$G_0 = N_0 M_0^{-1} = \tilde{M}_0^{-1} \tilde{N}_0, \tag{4.8}$$

$$K = X_0 Y_0^{-1} = \tilde{Y}_0^{-1} \tilde{X}_0, \tag{4.9}$$

where $M_0 \in \mathbb{RH}_\infty^{2 \times 2}$, $\tilde{M}_0 \in \mathbb{RH}_\infty^{1 \times 2}$, $N_0 \in \mathbb{RH}_\infty^{1 \times 2}$, $\tilde{N}_0 \in \mathbb{RH}_\infty^{2 \times 2}$, $X_0 \in \mathbb{RH}_\infty^{2 \times 1}$, $\tilde{X}_0 \in \mathbb{RH}_\infty^{2 \times 1}$, $Y_0 \in \mathbb{RH}_\infty^{1 \times 1}$ and $\tilde{Y}_0 \in \mathbb{RH}_\infty^{2 \times 2}$ are all stable transfer functions and satisfy the double Bezout identities given in Eqs. (1.5) and (1.6). These transfer functions can be obtained given the nominal plant and controller as described in [64].

In the presence of plant uncertainty, the transfer function G deviates from its nominal value G_0. The class of all plants $G(S)$, which can be stabilized by the controller K, can be parameterized in term of a stable transfer function $S \in \mathbb{RH}_\infty^{1 \times 2}$ as follows

$$G = G(S) = N M^{-1} = \tilde{M}^{-1} \tilde{N} \in \mathbb{R}_p^{1 \times 2}, \tag{4.10}$$

where,

$$N = N_0 + Y_0 S \quad M = M_0 - X_0 S, \tag{4.11}$$

$$\tilde{N} = \tilde{N}_0 + S \tilde{Y}_0 \quad \tilde{M} = \tilde{M}_0 - S \tilde{X}_0. \tag{4.12}$$

According to Eq. (4.7), temperature variations only change $R_{MA}(S)$; R_{VCM} is assumed to remain constant in its operating frequency region. Therefore, transfer function R_{MA}, in the nominal and uncertain cases, can be obtained as described below [64].

Nominal case: Consider the case when $S = 0$. The nominal closed loop transfer function is given by

$$R_0 = \frac{1}{1 + G_0 K} G_0 \in \mathbb{RH}_\infty^{1 \times 2}. \tag{4.13}$$

Substituting Eq. (4.8) and (4.9) into the above equation and using the double Bezout identities given in Eqs. (1.5) and (1.6) will result in

$$R_0 = [R_{0,VCM}, R_{0,MA}] = N_0 \tilde{Y}_0. \tag{4.14}$$

Uncertain case: Consider the case when S is non-zero. The closed loop transfer function is given by

$$R(S) = \frac{1}{1 + G(S)K} G(S) \in \mathbb{RH}_\infty^{1 \times 2}. \tag{4.15}$$

Utilizing Eqs. (4.9)-(4.12) and the double Bezout identities given in Eqs. (1.5) and (1.6) will result in

$$R = [R_{VCM}, R_{MA}] = N(S)\tilde{Y}_0, \tag{4.16}$$

where the transfer function $N(S) = N_0 + SY_0$ is affine in S. As mentioned earlier, it is assumed that the uncertainty is not affecting the closed-loop transfer function for the VCM, R_{VCM}, in its operating frequency region. Therefore, the MA closed-loop transfer function can be written as follows

$$R_{MA}(S) = R_{0,MA} + S\,Y_0\tilde{Y}_{0,2^{nd}} \in \mathbb{RH}_\infty^{1\times 1}, \tag{4.17}$$

where $\tilde{Y}_{0,2^{nd}} \in \mathbb{RH}_\infty^{2\times 1}$ represents the second column of $\tilde{Y}_0 \in \mathbb{RH}_\infty^{2\times 2}$.

In the subsequent section, the method for identification of uncertainty transfer function $\hat{S} \in \mathbb{RH}_\infty^{1\times 2}$ is represented, and the MA closed loop transfer function $\hat{R}_{MA}$ will be updated using Eq. (4.18). If $\hat{S}$ is identified with sufficient accuracy, $\hat{R}_{MA}$ can be close to R_{MA} and the robustness condition (*90-degree criteria*) given by Eq. (4.2) will be satisfied.

$$\hat{R}_{MA} = R_{0,MA} + \hat{S}\,Y_0\tilde{Y}_{0,2^{nd}} \in \mathbb{RH}_\infty^{1\times 1}. \tag{4.18}$$

Uncertainty Identification

In order to identify the uncertain stable transfer function $\hat{S}$ in Eq. (4.18), the first step is to obtain the nominal model. This nominal model is obtained by taking the average of several uncertain models of the system and reducing the order of the resulting transfer function. Having the nominal model, all the nominal transfer functions, such as the ones used in Eq. (4.18) are obtained. Then, the plant uncertainty ($\hat{S}$) will be identified using Eq. (4.18).

In order to identify the uncertainty parameter, $\hat{S}$, the recursive least square technique has been utilized. In this identification approach, a white noise, which is passed through a band pass filter, is used as an excitation signal at u_{MA}. The band pass filter is used to attenuate excitation outside of the frequency range at which the system is going to be identified. The response of the system to this excitation is measured by PES signal, e. According to Fig. 4.3, signal e can be written as

$$e = R_{MA}\,u_{MA} + T_s\,r + T_s\,n, \tag{4.19}$$

where $T_s \in \mathbb{RH}_\infty^{1\times 1}$ is representing the closed loop sensitivity transfer function. Moreover, Eq. (4.18) can be written as

$$\hat{R}_{MA}\,u_{MA} = R_{0,MA}\,u_{MA} + \hat{S}Y_0\tilde{Y}_0\,u_{MA} \tag{4.20}$$

In this equation, $\hat{R}_{MA}\,u_{MA}$ can be used as an approximation of PES, e, if the effects of the repeatable run-out, r, and noise, n are eliminated from e. The effects of run-out can be eliminated by filtering both u_{MA} and e at the run-out frequencies. Let

$$F(z^{-1}) = (1 - z^{-N}) \in \mathbb{RH}_\infty^{1\times 1}, \tag{4.21}$$

where N is the total number of PES measurements collected during one disk revolution. This filter can annihilate the repeatable run-out, i.e. $F(z^{-1}) \ r = 0$. Notice that N also represents the number of RRO harmonics. If the excitation signal is large enough compared to the noises in the system, term $T_s \ n$ in Eq. (4.19) can be ignored. Therefore, Eq. (4.19) can be written as

$$F \ e \simeq \hat{R}_{MA} F \ u_{MA} = R_{0,MA} F \ u_{MA} + \bar{S} Y_0 \tilde{Y}_0 F \ u_{MA}, \qquad (4.22)$$

In this equation, the only unknown is the stable transfer function $\hat{S} \in \mathbb{RH}_\infty^{1 \times 2}$, which is obtained using the recursive least square technique.

As mentioned in the previous section, the transfer function S is guaranteed to be input-output stable, therefore, it can be identified either as a finite impulse response (FIR) or a stable infinite impulse response (IIR) transfer function. Eq. (4.23) shows the FIR formulation of this transfer function. The advantage of the FIR filter is that the resulting estimated transfer function

$$\hat{S}_{FIR}(z^{-1}) = \left[\sum_{m=0}^{M} z^{-m} \hat{s}_{m,1}, \quad \sum_{m=0}^{M} z^{-m} \hat{s}_{m,2} \right] \in \mathbb{RH}_\infty^{1 \times 2} \qquad (4.23)$$

is always stable. Here, $\hat{s}_{m,1}, \hat{s}_{m,2}, m = 0, \cdots M$, are the identified parameters, M is the order of the FIR filter and z^{-d} is the backwards-shift operator (i.e. $y(k-d) = z^{-d}y(k)$). However, FIR filters normally require a larger number of parameters than IIR filters to adequately characterize a plant response, particularly if the identified plant has lightly damped poles.

Infinite impulse response (IIR) filters have both numerator and denominator polynomials. Thus, the identified transfer function is given by

$$\hat{S}_{IIR}(z^{-1}) = \left[\frac{\sum_{m=0}^{M} z^{-m} \hat{b}_{s_{m,1}}}{1 + \sum_{n=1}^{N} z^{-n} \hat{a}_{s_{n,1}}}, \quad \frac{\sum_{m=0}^{M} z^{-m} \hat{b}_{s_{m,2}}}{1 + \sum_{n=1}^{N} z^{-n} \hat{a}_{s_{n,2}}} \right]. \qquad (4.24)$$

where M and N are respectively the orders of the numerator and denominator polynomials, while $\hat{b}_{s_{m,1}} \in \mathbb{R}, \hat{b}_{s_{m,2}} \in \mathbb{R}, m = 0, \ldots, M$ and $\hat{a}_{s_{n,1}} \in \mathbb{R}, \hat{a}_{s_{n,2}} \in \mathbb{R}, n = 1, \ldots, N$, are the estimated parameters. It is however necessary to guarantee that identified denominator polynomial parameters are such that the roots of the polynomials $z^N + \sum_{n=1}^{N} \hat{a}_{s_{n,1}} z^{N-n} = 0$ and $z^N + \sum_{n=1}^{N} \hat{a}_{s_{n,2}} z^{N-n} = 0$ are all inside the unit circle.

In order to address the concern about the stability of the identified IIR transfer function, the Jury test[39] can be used in each time step, to check the stability of the identified transfer function. If at any time step, the obtained IIR transfer function is not stable, all the closed loop poles can be projected inside the unit circle by a simple multiplication. Therefore, the resulting closed loop feedback system in Fig. 4.3 can be guaranteed to be stable when S is identified using an IIR filter, as given by Eq. (4.24).
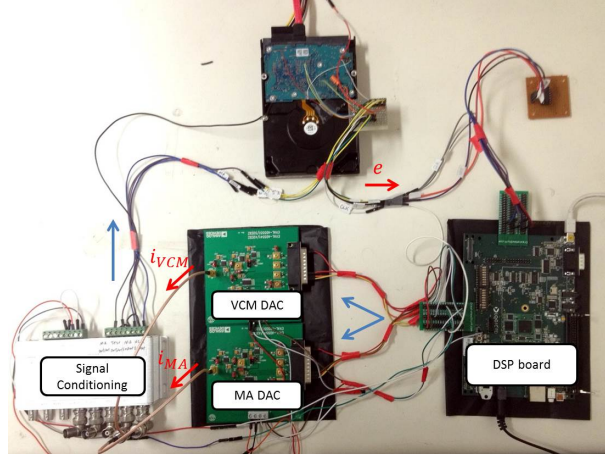
Figure 4.4: The experimental setup

4.3 Experimental Results

The proposed algorithm in the previous section has been implemented on a real hard disk drive, as shown in Fig. 4.4. The setup includes a DSP board which receives the PES signal, e, and can compute the signals which are needed to be injected at the u_{VCM}[1] and u_{MA} ports. The output of the DSP board is digital, therefore, DAC cards have been used to convert u_{VCM} and u_{MA} to analog signals prior to injection of these signals to the HDD. In this experiment, at each time step, the excitation signal, u_{MA}, is applied to the HDD and e is measured as the response of the system to this excitation. Therefore, the DSP board will use both the excitation and response signals in order to identify the uncertainty transfer function $S \in \mathbb{RH}_{\infty}^{1 \times 2}$.

Simulation results demonstrate that $S \in \mathbb{RH}_{\infty}^{1 \times 2}$ can be identified with a single transfer function estimate, $\hat{S} \in \mathbb{RH}_{\infty}^{1 \times 2}$, for the entire frequency range $\omega \in [0, \omega_N]$ where ω_N is the Nyquist frequency. However, the variance of the random excitation signal u_{MA} that is required to identify $\hat{S}$ for the entire frequency range is too large and results in an unacceptable track mis-registration (TMR). Therefore, $\hat{S}$ has been identified in three smaller frequency regions. In this case the required excitation signal variance is smaller than the maximum allowable injection signal. Moreover in each region, each element of $\hat{S} \in \mathbb{RH}_{\infty}^{1 \times 2}$ was identified using a second order IIR filter, as shown in Eq. (4.25).

$$\hat{S} = \frac{1}{S_0 + S_1 z^{-1} + S_2 z^{-2}} \left[\begin{array}{c} S_3 + S_4 z^{-1} + S_5 z^{-2} \\ S_6 + S_7 z^{-1} + S_8 z^{-2} \end{array} \right]^T \in \mathbb{RH}_{\infty}^{1 \times 2} \qquad (4.25)$$

In this structure, the same denominator is used for both elements of $\hat{S} \in \mathbb{RH}_{\infty}^{1 \times 2}$, in order to reduce the number of identified parameters. Moreover, during the identification process, the

---

[1]u_{VCM} port has not been used for this experiment.
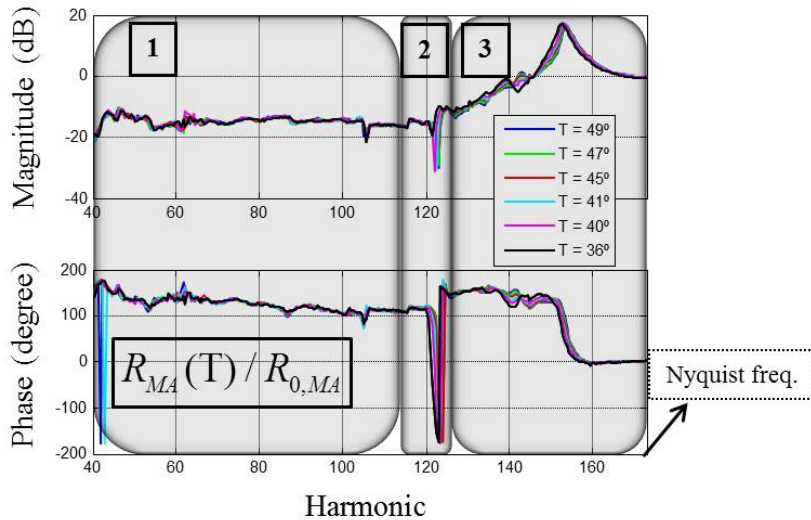
Figure 4.5: Frequency responses of R_{MA} at different temperatures, compared with the frequency response of the reduced order transfer function $R_{0,MA}$ at the nominal temperature of $34°\ Celsius$

stability of this second order denominator can be easily verified online using e.g. Jury test and, in the case of instability, the poles are projected inside the unit circle [18].

Fig. 4.5 shows the Bode plot of the ratio $R_{MA}(T)/R_{MA,0}$, where $R_{MA}(T)$ is the transfer function R_{MA} obtained at temperature T, while $R_{MA,0}$ is a reduced order transfer function at the nominal temperature of $34°\ Celsius$. According to the "90-degree criteria," the phase mismatch between $R_{MA}(T)$ and $R_{MA,0}$ must be less than 90 degree, which is violated here. Therefore, a single nominal second order transfer function $R_{MA,0}$ cannot be used in the adaptive RRO following algorithm.

The next set of plots in Figs. 4.6 and 4.7 show the experimental results. First, $\hat{S}$ has been identified using Eq. 4.25. This identification has been taken place in three frequency regions shown in Fig. 4.5. The Bode plots of the identified $\hat{S}$'s are given in Fig. 4.6, where the red asterisks show the frequency region in which the the parameter $\hat{S}$ has been identified. These identified transfer functions have been used in Eq. (4.18) to generate $\hat{R}_{MA}$, which is in turn used in the adaptive RRO following algorithm. The ratio of the actual transfer function, R_{MA}, over the updated models, $\hat{R}_{MA}$, are shown in Fig. 4.7, for the three frequency regions in Fig. 4.5. As shown in Fig. 4.7, the phase mismatch between the actual and the updated model is always less than 90 degree in each identified region, which shows the effectiveness of the proposed algorithm in satisfying the "90-degree criteria" in Eq. (4.2). It is worth mentioning that the proposed identification process was implemented as an online process, in order to compensate in real time the effect of temperature variations in the HDD dynamics.
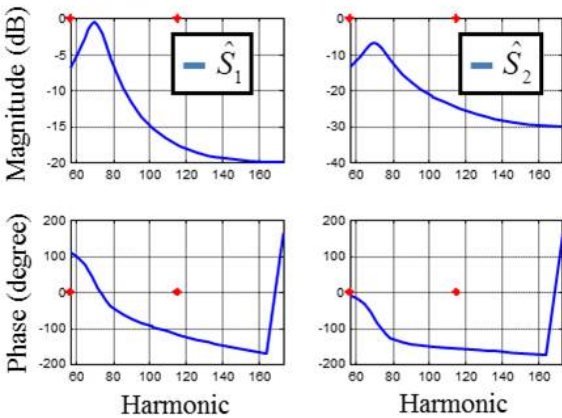
(a) Region 1
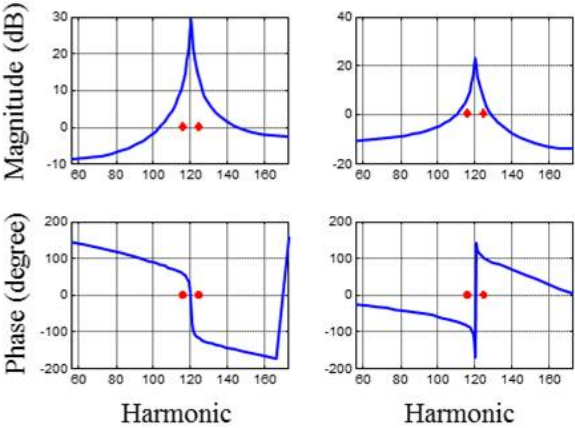
(b) Region 2
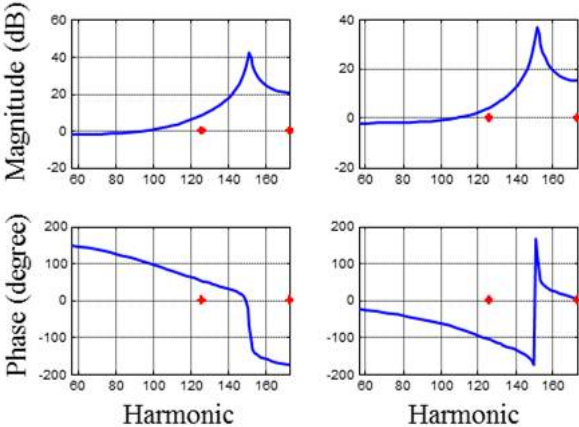
(c) Region 3

Figure 4.6: Bode plot of the identified uncertainty, $\hat{S} = [\hat{S}_1, \hat{S}_2] \in \mathbb{RH}_\infty^{1 \times 2}$, for the three frequency regions (The red asterisks show the frequency region in which the identification has been done.)
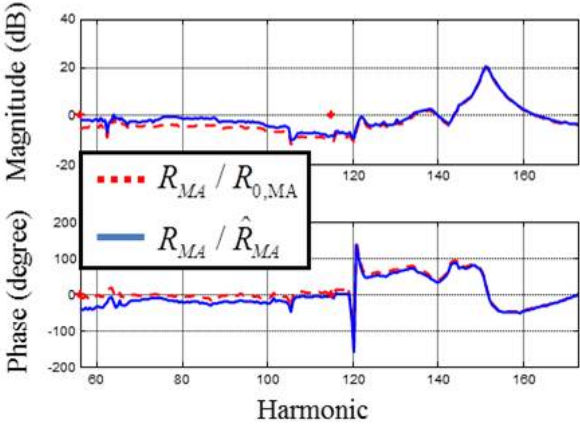
(a) Region 1
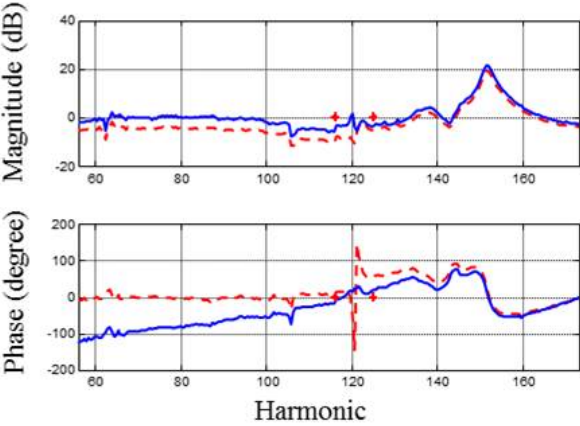
(b) Region 2
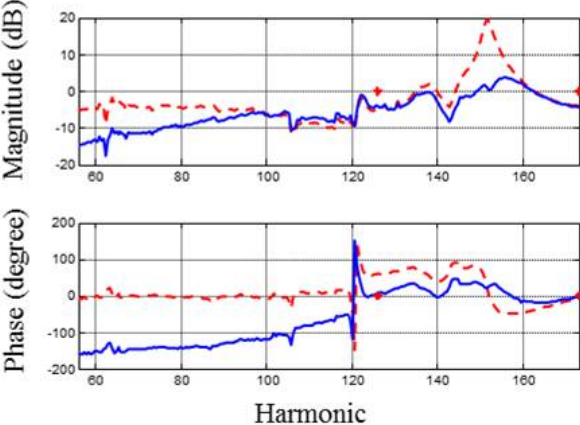
(c) Region 3

Figure 4.7: Comparison of the relative frequency response from the MA injection point to PES for the three frequency regions (The red asterisks show the frequency region in which the identification has been done.)

Chapter 5

Data Driven Control Design

The data-driven control design methodology, which designs the controller based on the frequency response measurements of the system, is discussed in this chapter. The main advantage of data-driven over model-based control design techniques is that the former only require the frequency response measurements of the plant without the need to identify a model. Therefore, the designed controller is guaranteed to stabilize the real physical system and achieve the performance specifications considered in the design process, if the number of measurements are adequate enough to represent the variations in the real physical system.

In section 5.1, the notations and mathematical preliminaries used in the data-driven control designs are elaborated. Subsequently, the control objectives which are considered in terms of H_∞ and H_2 norms of closed loop transfer functions are provided in section 5.2. The controller is obtained by solving a convex optimization problem, where these norms are translated to convex constraints and objectives. The necessary and sufficient convex conditions for the H_∞ constraints of the SISO systems have been proposed in [42]. Section 5.3 will extend this result to MISO systems. These extended results are considered along with H_2 results from [41] to form a mixed H_2/H_∞ control problem. The plant dynamics variations are addressed by considering multiple frequency response measurements of the plant in the design step.

5.1 Notations and Mathematical Preliminaries

In this section, the notations and preliminary concepts used for the data driven controller design are presented. First, the stable factorizations of the plant and controller will be reviewed. Then, the closed loop feedback structure and the resulting closed loop transfer functions are introduced.
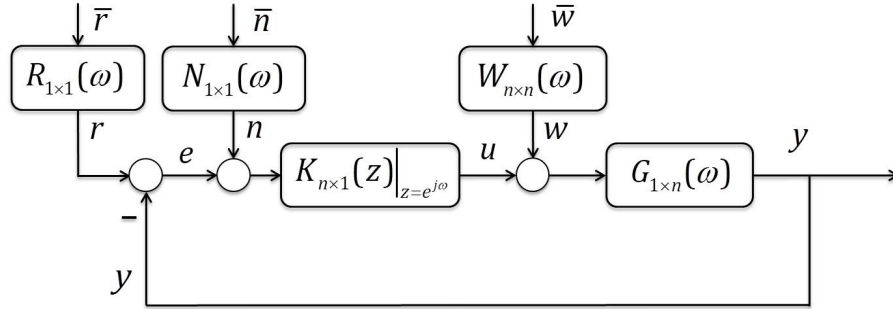
Figure 5.1: Control block diagram. $G_{1\times n}(\omega)$ represents the frequency response data of the plant. The disturbances to the system are colored by the stable weighting functions $R(\omega) \in \mathbb{RH}_\infty$, $N(\omega) \in \mathbb{RH}_\infty$ and $W(\omega) \in \mathbb{RH}_\infty^{n\times n}$.

Plant and Controller Factorizations

Consider the control block diagram given in Fig. 5.1. The block $G_{1\times n}(\omega)$ represents a controllable MISO system in terms of frequency response measurements. The plant accepts n control inputs and has only one sensor measurement as the output. The controller $K_{n\times 1}(z)$, uses the single measurement and generates the n control inputs. Therefore, the controller has one input and n outputs. This controller is called a SIMO system. The dimension notation used as a subscript may be eliminated in few places for the purpose of simplifying the notations.

The plant and controller are factorized using stable factorizations[26] given in Eqs. (1.2) and (1.3). According to stable factorizations, any system can be represented as the product of one stable system and the inverse of another stable system. Stable factorizations for the plant and the controller are as follows

$$G_{1\times n}(\omega) = \tilde{M}_{1\times 1}^{-1}(\omega)\tilde{N}_{1\times n}(\omega), \tag{5.1}$$

$$K_{n\times 1}(z) = X_{n\times 1}(z)Y_{1\times 1}^{-1}(z), \tag{5.2}$$

where $\tilde{M}_{1\times 1} \in \mathbb{RH}_\infty^{1\times 1}$, $\tilde{N}_{1\times n} \in \mathbb{RH}_\infty^{1\times n}$, $X_{n\times 1} \in \mathbb{RH}_\infty^{n\times 1}$ and $Y_{1\times 1} \in \mathbb{RH}_\infty^{1\times 1}$. It is worth mentioning that the stable factorizations can be obtained in both the frequency and z domains. Here, the plant $G_{1\times n}(\omega)$ in Eq. (5.1) is factorized in the frequency domain, while the controller $K_{n\times 1}(z)$ in Eq. (5.2) is factorized in the z domain. The stable factorizations in the z domain can be easily converted to the frequency domain using $z = e^{j\omega}$.

Deriving the stable factorizations for the plant $G_{1\times n}(\omega)$ in Eq. (5.1) can be challenging, since inspecting the stability of frequency response data is not straightforward. Here, three different scenarios for obtaining stable factorizations for the plant $G_{1\times n}(\omega)$ in the frequency domain are considered.

- *Stable $G_{1\times n}(\omega)$*: The most straightforward stable factorizations for a stable plant

$G_{1 \times n}(\omega)$ is

$$\tilde{N}_{1 \times n}(\omega) = G_{1 \times n}(\omega), \tag{5.3}$$

$$\tilde{M}_{1 \times n}(\omega) = 1. \tag{5.4}$$

- *Unstable* $G_{1 \times n}(\omega)$: A stabilizing controller $K_{n \times 1}^0(z)$ will be used to obtain the stable factorizations.

$$\tilde{N}_{1 \times n}(\omega) = \frac{G_{1 \times n}(\omega)}{1 + G_{1 \times n}(\omega)K_{n \times 1}^0(e^{j\omega})}, \tag{5.5}$$

$$\tilde{M}_{1 \times 1}(\omega) = \frac{1}{1 + G_{1 \times n}(\omega)K_{n \times 1}^0(e^{j\omega})}. \tag{5.6}$$

The factorizations given in Eqs (5.5) and (5.6) are stable, since both of these factorizations represent closed loop transfer functions of stable loops. It should be noted that $\tilde{N}_{1 \times n}(\omega)$ and $\tilde{M}_{1 \times 1}(\omega)$ in Eqs. (5.5) and (5.6) are themselves frequency response data, which are generated by computing the right side of the equation point-wise at the frequency point $\omega \in \Omega$. Also, $K_{n \times 1}^0(e^{j\omega}) \in \mathbb{C}^{n \times 1}$ is the data generated by computing the frequency response of the compensator $K_{n \times 1}^0(z)\big|_{z=e^{j\omega}}$ at the frequency point $\omega \in \Omega$, where $\Omega = (-\pi, \pi]$.

- *Known marginally stable poles times a stable* $G_{1 \times n}^0(\omega)$: In the case of known marginally stable poles, these poles can be considered as zeros in the factorization $\tilde{M}_{1 \times 1}(\omega)$. As an example, the stable factorizations of the following plant

$$G_{1 \times n}(\omega) = (\frac{e^{j\omega}}{e^{j\omega} - 1})^2 G_{1 \times n}^0(\omega) \tag{5.7}$$

can be derived as

$$\tilde{N}_{1 \times n}(\omega) = G_{1 \times n}^0(\omega), \tag{5.8}$$

$$\tilde{M}_{1 \times 1}(\omega) = (\frac{e^{j\omega} - 1}{e^{j\omega}})^2, \tag{5.9}$$

where $\tilde{N}_{1 \times n}(\omega)$ and $\tilde{M}_{1 \times 1}(\omega)$ will be stable factorizations of the plant $G_{1 \times n}(\omega)$.

The controller $K(z)$ is implemented in the z domain. Subsequently, the factorizations of this controller given in Eq. (5.2) are obtained in the z domain as well. These factorizations are stable if and only if all their poles are chosen to be inside the unit circle. Considering the following structure for the SIMO controller with m outputs in Fig. 5.1

$$K_{n \times 1}(z) = \frac{1}{y_n z^n + .. + y_1 z + y_0} \begin{bmatrix} x_{1,n} z^n + .. + x_{1,1} z + x_{1,0} \\ .. \\ x_{m,n} z^n + .. + x_{m,1} z + x_{m,0} \end{bmatrix}, \tag{5.10}$$

a simple set of stable factorizations will be the finite impulse response, FIR, filter with all the poles located at the origin.

$$X_{n \times 1}(z) = \frac{1}{z^n} \begin{bmatrix} x_{1,n}z^n + .. + x_{1,1}z + x_{1,0} \\ .. \\ x_{m,n}z^n + .. + x_{m,1}z + x_{m,0} \end{bmatrix}, \tag{5.11}$$

$$Y_{1 \times 1}(z) = \frac{y_n z^n + .. + y_1 z + y_0}{z^n} \tag{5.12}$$

where $X(z)$ and $Y(z)$ represent stable factorizations of the controller in Eq. (5.2). The stable factorizations can be written as the product of the controller coefficients and filter terms

$$X_{n \times 1}(z) = \rho_x F_x(z), \tag{5.13}$$

$$Y_{1 \times 1}(z) = \rho_y F_y(z), \tag{5.14}$$

where ρ_x and ρ_y represent the controller coefficients

$$\rho_x = \begin{bmatrix} x_{1,n}, & .., & x_{1,1}, & x_{1,0} \\ & .. & \\ x_{m,n}, & .., & x_{m,1}, & x_{m,0} \end{bmatrix}, \tag{5.15}$$

$$\rho_y = \begin{bmatrix} y_n, & .., & y_1, & y_0 \end{bmatrix}, \tag{5.16}$$

and the filter terms $F_x(z)$ and $F_y(z)$ are written as follows

$$F_x(z) = \frac{1}{z^n} \begin{bmatrix} z^n & .. & z^1 & z^0 \end{bmatrix}^T, \tag{5.17}$$

$$F_y(z) = \frac{1}{z^n} \begin{bmatrix} z^n & .. & z^1 & z^0 \end{bmatrix}^T. \tag{5.18}$$

Here for simplicity, the poles of stable factorizations are chosen to be at the origin. However, these poles can be chosen to be anywhere inside the unit circle. Any change in the location of these poles will directly affect the denominator of filter terms given in Eqs. (5.17) and (5.18).

A fixed structure can be considered inside the controller while deriving the stable factorizations for the controller. Assuming that the first element of the controller should include an integrator with the following structure

$$K_{f,1}(z) = \frac{z}{z - 1}. \tag{5.19}$$

The stable factorizations of the controller given in Eqs. (5.11) and (5.12) are modified to include this integrator in the structure.

$$X_{n \times 1}(z) = \frac{1}{(z - \alpha)z^{n-1}} \begin{bmatrix} z \left(x_{1,n-1}z^{n-1} + .. + x_{1,1}z + x_{1,0} \right) \\ (z - 1) \left(x_{2,n-1}z^{n-1} + .. + x_{2,1}z + x_{2,0} \right) \\ .. \\ (z - 1) \left(x_{m,n-1}z^{n-1} + .. + x_{m,1}z + x_{m,0} \right) \end{bmatrix}, \tag{5.20}$$

$$Y_{1\times1}(z) = \frac{z-1}{z-\alpha}\frac{y_{n-1}z^{n-1} + .. + y_1 z + y_0}{z^{n-1}},\tag{5.21}$$

where $|\alpha| < 1$ is a pole inside the unit circle. The stable factorizations in Eqs. (5.20) and (5.21) can also be written in terms of controller coefficients using Eqs. (5.13) and (5.14).

Feedback structure

The feedback structure given in Fig. 5.1 is used to design the controller $K(z)$. In this block diagram, r represents the reference trajectory which is desired to be followed. In addition, signals n, w represent measurement and control input noises, respectively. Signals $\bar{r}, \bar{n}, \bar{w}$ are white noises with unit variances, and the filter blocks $R \in \mathbb{RH}_\infty$, $N \in \mathbb{RH}_\infty$, $W \in \mathbb{RH}_\infty^{n\times n}$ are used to color these white noises.

In Fig. 5.1, the lower-case letters are used to represent signals, where the upper-case letters are used to represent open loop transfer functions. The closed loop transfer functions are also denoted using upper-case letters, where their subscripts represent the input to output causality. For example, $E_{r\to e}$ denotes the closed loop transfer function from input r to output e. Since the plant $G(\omega)$ in Fig. 5.1 is represented in the frequency domain, all the closed loop transfer functions are derived in the frequency domain. To make the notations simple, the frequency domain arguments $(e^{j\omega})$ and (ω) will be eliminated from transfer function notations.

The closed loop transfer functions from external signals in Fig. 5.1 to tracking error e, control input u and the measurement output y are given by

$$\begin{bmatrix} e \\ u \\ y \end{bmatrix} = \begin{bmatrix} E_{r\to e} & E_{n\to e} & E_{w\to e} \\ U_{r\to u} & U_{n\to u} & U_{w\to u} \\ Y_{r\to y} & Y_{n\to y} & Y_{w\to y} \end{bmatrix} \begin{bmatrix} r \\ n \\ w \end{bmatrix}.\tag{5.22}$$

Eq. (5.22) represents the transfer functions from colored excitation signals. The closed loop transfer functions from the white noises can be easily derived as follows

$$\begin{bmatrix} E_{\bar{r}\to e} & E_{\bar{n}\to e} & E_{\bar{w}\to e} \\ U_{\bar{r}\to u} & U_{\bar{n}\to u} & U_{\bar{w}\to u} \\ Y_{\bar{r}\to y} & Y_{\bar{n}\to y} & Y_{\bar{w}\to y} \end{bmatrix} = \begin{bmatrix} E_{r\to e} & E_{n\to e} & E_{w\to e} \\ U_{r\to u} & U_{n\to u} & U_{w\to u} \\ Y_{r\to y} & Y_{n\to y} & Y_{w\to y} \end{bmatrix} \cdot \begin{bmatrix} R & 0 & 0 \\ 0 & N & 0 \\ 0 & 0 & W \end{bmatrix}.\tag{5.23}$$

The closed loop transfer functions in Eqs. (5.22) and (5.23) are written in terms of the plant G and controller K using the block diagram in Fig. 5.1

$$\begin{bmatrix} E_{r\to e} & E_{n\to e} & E_{w\to e} \\ U_{r\to u} & U_{n\to u} & U_{w\to u} \\ Y_{r\to y} & Y_{n\to y} & Y_{w\to y} \end{bmatrix} = \frac{1}{1+KG} \begin{bmatrix} 1 & -KG & -G \\ K & K & -GK \\ GK & GK & G \end{bmatrix}.\tag{5.24}$$

Eqs. (5.1) and (5.2) can be used to derive the closed loop transfer functions in Eq. (5.24) in terms of the stable factorizations of the plant and controller

$$
\begin{bmatrix} E_{r\to e} & E_{n\to e} & E_{w\to e} \\ U_{r\to u} & U_{n\to u} & U_{w\to u} \\ Y_{r\to y} & Y_{n\to y} & Y_{w\to y} \end{bmatrix} = \frac{1}{X\tilde{N} + Y\tilde{M}} \begin{bmatrix} \tilde{M}Y & -X\tilde{N} & -\tilde{N}Y \\ \tilde{M}X & \tilde{M}X & -\tilde{N}X \\ \tilde{N}X & \tilde{N}X & \tilde{N}Y \end{bmatrix}.
\tag{5.25}
$$

It is worth mentioning that using the stable factorizations given in Eqs. (5.1) and (5.2) will create the common scalar denominator, $X\tilde{N} + Y\tilde{M}$, for all the closed loop transfer functions. Moreover, both the numerators and the denominator are all linear functions of both plant and controller stable factorizations, where these factorizations are also linear functions of controller coefficients in Eqs. (5.13) and (5.14).

5.2   Control Objectives

The very first step to design the controller $K_{n\times 1}(z)$ in Fig. 5.1 is to define the desired control objectives. The H_∞ and H_2 norms of the closed loop transfer functions will be used to define the control objectives, since these norms are representing both the average performance of the closed loop systems across the frequency region as well as the worst performance at a single frequency.

H_∞ norm

The H_∞ norm of a system was defined in Eq. (1.9). This norm is helpful for constraining the maximum singular value of the system across the entire frequency region. Therefore, this norm criteria can be used to shape the closed-loop transfer functions. As an example, the following H_∞ norm constraint for the SISO system $H_{1\times 1}$ is defined as

$$
\|W_H H_{1\times 1}\|_\infty < \gamma,
\tag{5.26}
$$

where $W_H \in \mathbb{C}$ is a bounded weighting function in the frequency domain and γ is the upper-bound for this H_∞ norm. According to the definition of the H_∞ norm for the SISO systems given in Eq. (1.11) and assuming

$$
\forall \omega \in \Omega : |W_H| \neq 0,
\tag{5.27}
$$

Eq. (5.26) can be written as follows

$$
\forall \omega \in \Omega : |H_{1\times 1}| < \gamma |W_H|^{-1}.
\tag{5.28}
$$

Therefore, the magnitude of the transfer function $H_{1\times 1}$ can be shaped with respect to the weighting function W_H and the scalar γ. In the data-driven control design method, W_H can be any numerically shaped bounded weighting function satisfying Eq. (5.27).

The H_∞ norm constraint defined in Eq. (5.26) can also be used for the MIMO system $H_{p \times q} \in \mathbb{R}_p^{p \times q}$ as follows

$$\|W_H H_{p \times q}\|_\infty < \gamma, \tag{5.29}$$

where $W_H \in \mathbb{C}^{o \times p}$ is a bounded weighting function in the frequency domain. According to the definition of the H_∞ norm for the MISO systems given in Eq. (1.9), Eq. (5.29) can be written as

$$\forall \omega \in \Omega : \bar{\sigma}(W_H H_{p \times q}) < \gamma, \tag{5.30}$$

where $\bar{\sigma}(M)$ represents the maximum singular value of the matrix M. In [33], it has been proved that the following inequality holds for the maximum singular value of the product of matrices $A \in \mathbb{C}^{a \times b}$ and $B \in \mathbb{C}^{b \times c}$, $a \geqslant b$,

$$\underline{\sigma}(A)\bar{\sigma}(B) \leq \bar{\sigma}(AB). \tag{5.31}$$

where $\underline{\sigma}(M)$ represents the minimum singular value of the matrix M. By combining Eqs. (5.30) and (5.31), and assuming

$$\forall \omega \in \Omega : \underline{\sigma}(W_H) \neq 0, \; W_H \in \mathbb{C}^{o \times p}, \; o \geqslant p, \tag{5.32}$$

Eq. (5.29) will result in the following equation

$$\forall \omega \in \Omega : \bar{\sigma}(H_{p \times q}) < \gamma \, \underline{\sigma}(W_H)^{-1}, \tag{5.33}$$

where the weighting function W_H can be defined to shape the maximum singular value of the transfer function $H_{p \times q}$. It is worth mentioning that Eq. (5.33) is only a necessary and not a sufficient condition for the H_∞ criterion defined in Eq. (5.29). However, Eq.(5.29) is directly used in the proposed control algorithm to derive a necessary and sufficient condition for the H_∞ norm criterion. Eq. (5.33) is used to represent the intuition behind the weighting function selection for MIMO systems.

Eq. (5.26) represents a H_∞ constraint on a closed loop transfer function. However, the H_∞ can be considered as an objective

$$\min_{\omega \in \Omega, \; K \in \mathbb{R}_{p,g}^{n \times 1}} \|W_H H\|_\infty, \tag{5.34}$$

where the goal is to find the controller $K(z)$ of order g in Fig. 5.1, which minimizes this norm.

H_2 norm

The H_2 norm of a system defined in Eq. (1.12) is a representative of the system average energy over the entire frequency region. Therefore, this norm is considered in the control design process to take into account the average energy of different closed loop transfer functions. Similar to the H_∞ norm, the H_2 norm can be either constrained by a scalar η

$$\|H\|_2^2 \leq \eta, \tag{5.35}$$

or minimized

$$\min_{K \in \mathbb{R}^{n \times 1}_{p,g}} \|H\|_2^2, \tag{5.36}$$

where the goal is to find the controller $K(z)$ of order g in Fig. 5.1.

The Parseval's relation [72] states that the square of the H_2 norm of a transfer function in the frequency domain is equal to the the variance of the corresponding signal in the time domain, if the input to the transfer function is zero mean white noise with a unit variance. Therefore, the H_2 norm constraint and objective defined in Eqs. (5.35) and (5.36) will directly constrain or minimize the variance of signals in the time domain.

Consider a signal $s(\omega)$, which is constructed using the following equation

$$s(\omega) = G(\omega)w(\omega) + s_0, \tag{5.37}$$

where $w(\omega)$ is a zero mean white noise with unit variance, $G(\omega)$ is a SISO stable filter transfer function and s_0 is a constant scalar. According to the Parseval's relation [72], the square of the H_2 norm of the transfer function $G(\omega)$ is equal to the variance of the signal $s(\omega)$ in the time domain which is denoted by σ^2.

$$\sigma^2 = E[\|(s(k) - s_0)^2\|] = \|G(\omega)\|_2^2 \tag{5.38}$$

where k represent the time domain notation. As a result, the variance of the signal $s(\omega)$ in the time domain can be directly minimized or constrained by considering the square of the H_2 norm of the transfer function $G(\omega)$ in the frequency domain as the minimization objective or constraints. The ability to restrict the variance of signals in the time domain can be helpful when dealing with actuator limitations such as input voltage or output stroke limitations.

Multiple plant measurements

The H_∞ and H_2 control objectives defined above are based on one frequency response measurement from a single plant. However, plants produced in the same production line may have slight variations in their frequency response measurements. Moreover, the frequency response measurement of a specific plant may have uncertainties or variations due to changing conditions. The H_∞ and H_2 control objectives can be modified to accommodate a number of plant frequency response measurements in the control design process.

Assume that there are l frequency response measurements available for the plant G in Fig. 5.1. Each of these measurements is denoted by G_i, where i represents the i's measurement. As a result for each specific closed loop path in Fig. 5.1, there are l closed-loop transfer functions corresponding to each individual plant measurement. These closed loop transfer functions are denoted as H_i.

In this dissertation, the H_∞ control objective for multiple plant measurements is defined based on the worst case scenario. Therefore, the H_∞ norm constraint given in Eq. (5.26) can be extended to multiple measurements using the following definition

$$\forall i \in 1, ., l : \|W_H H_i\|_\infty < \gamma, \tag{5.39}$$

which basically constrains the H_∞ norm of the closed loop transfer function for each individual measurements. Similarly, the H_∞ norm minimization objective defined in Eq. (5.34) can be extended as

$$\min_{\omega \in \Omega, \ K \in \mathbb{R}^{n \times 1}_{p,g}} \max_i \|W_H H_i\|_\infty \,, \tag{5.40}$$

where the goal is to find the controller $K(z)$ of order g, which minimizes the largest H_∞ norm among all the measurements.

The H_2 control objective for multiple plant measurements can be defined as the average of or the worst H_2 norm square of all the plant measurements.

- *The average H_2 norm*: The H_2 norm constraint given in Eq. (5.35) can be extended for multiple plant measurements as follows.

$$\frac{1}{l} \sum_{i=1}^{l} \|H_i\|_2^2 \leq \eta \tag{5.41}$$

  which constrains the average H_2 norm square of all the measurements. The H_2 norm minimization objective defined in Eq. (5.36) can be extended as

$$\min_{K \in \mathbb{R}^{n \times 1}_{p,g}} \sum_{i=1}^{n} \frac{1}{l} \|H_i\|_2^2 \tag{5.42}$$

  where the average H_2 norm square of all the measurements is minimized by solving for the controller $K(z)$ of order g.

- *The worst H_2 norm*: The H_2 norm constraint given in Eq. (5.35) can also be extended for multiple plant measurements as follows

$$\forall i \in 1, ., l : \|H_i\|_2^2 \leq \eta. \tag{5.43}$$

  This inequality constrains the worst H_2 norm square of all the measurements. The H_2 norm minimization objective defined in Eq. (5.36) can be extended as

$$\min_{K \in \mathbb{R}^{n \times 1}_p} \max_i \|H_i\|_2^2 \,, \tag{5.44}$$

  where the worst H_2 norm square of all the measurements is minimized.

5.3   Control Algorithms

The algorithm used to design the controller $K(z)$ in Fig. 5.1 will be discussed in this section. This algorithm does not rely on the use of a plant model. Instead, the algorithm synthesizes the controller by directly utilizing the available frequency response data from the plants.

The control objectives considered for this algorithm were reviewed in section 5.2, where it is desired to either constrain or minimize the H_∞ and H_2 norms of closed loop transfer functions. In this section, the individual convex conditions of H_∞ norm control objectives given in Eqs. (5.39) and (5.40) as well as H_2 norm control objectives given in Eqs. (5.41)-(5.44) are first described. Subsequently, the mixed H_2/H_∞ control problem are formulated by combining the convex conditions for both the H_∞ and H_2 norm control objectives.

Data-driven H_∞ control design

The data-driven H_∞ control design method is developed to design a stabilizing controller by minimizing or constraining the H_∞ norm of selected sets of closed loop transfer functions. In [42], *Karimi et al.* proposed a data-driven H_∞ control design methodology for Single Input-Single Output (SISO) systems. In this section, this algorithm is extended to Multi Input-Single Output (MISO) systems. The developed control algorithm obtains a necessary and sufficient convex condition for the H_∞ norm, which also guarantees the closed loop stability. Since the H_∞ norm control problem is translated to a convex condition, the controller can be obtained by solving a convex optimization problem.

The SIMO control block diagram for a MISO system is shown in Fig. 5.1, where the goal is to obtain the controller $K(z)$ satisfying the control objectives in section 5.2. Eq. (5.25) represents the closed loop transfer functions in terms of stable factorizations of the plant and controller given in Eqs. (5.1) and (5.2). As one can notice, all the closed loop transfer functions have a scalar denominator. However, the numerators can be scalar, vector or matrix transfer functions.

As an example, the convex condition for the H_∞ norm of the closed loop transfer function from control input disturbance w to control input u will be presented. The procedure for obtaining the convex condition of all other closed loop transfer functions in Eq. (5.25) is similar.

$$U_{w \to u} = \frac{-\tilde{N}X}{X\tilde{N} + Y\tilde{M}} \tag{5.45}$$

where $U_{w \to u} \in \mathbb{R}_p^{n \times n}$, since control input disturbance $w \in \mathbb{R}^n$ and control input signal $u \in \mathbb{R}^n$. The weighted H_∞ norm for this transfer function can be defined as follows.

$$H_\infty = \|W_{U_{w \to u}} U_{w \to u}\|_\infty, \tag{5.46}$$

where the weighting function, $W_{U_{w \to u}} \in \mathbb{C}^{n \times n}$, can be any numerically shaped bounded function of frequency. As mentioned in section 5.2, this weighting function will shape the maximum singular values of the closed loop transfer function $U_{w \to u}$ across the entire frequency region, if Eq. (5.32) is satisfied.

The following theorem proposes a methodology to convert the data-driven H_∞ control problem into a convex optimization problem for the given H_∞ norm defined in Eq. (5.46). The theorem was first developed for SISO systems in [42]. Theorem 5.3.1 extends the results to MISO systems.

Theorem 5.3.1. *Assume that the frequency response data for the plant $G_{1 \times n}(\omega)$ with n inputs and one output is given over the frequency region Ω, and is factorized according to Eq. (5.1). Given a positive scalar γ, the following two statements are equivalent.*

- *I) Controller $K_{n \times 1}(z)$ stabilizes the plant $G_{1 \times n}(\omega)$ and*

$$\|W_{U_{w \to u}} U_{w \to u}\|_\infty < \gamma \tag{5.47}$$

- *II) There exists controller stable factorizations $X(z)\big|_{z=e^{j\omega}}, Y(z)\big|_{z=e^{j\omega}}$ according to Eq. (5.2), such that the following convex inequality holds,*

$$\forall \omega \in \Omega : \gamma^{-1} \bar{\sigma}(\ W_{U_{w \to u}}(\omega) X(e^{j\omega}) \tilde{N}(\omega)\ ) < Re(\ \tilde{N}(\omega) X(e^{j\omega}) + \tilde{M}(\omega) Y(e^{j\omega})\ ) \tag{5.48}$$

where $\bar{\sigma}(M)$ and $Re(r)$ functions represent the maximum singular value of the matrix M and the real part of the complex number r, respectively.

Proof: See appendix A.

This theorem defines a necessary and sufficient convex condition for the H_∞ norm criterion given in Eq. (5.47). This H_∞ criteria can be used to either constraint or minimize the H_∞ norm in Eq. (5.46). It is worth mentioning that the frequency set Ω represents the entire frequency region. However, it is not practical to consider the condition in Eq. (5.48) for the entire frequency region. Therefore, a linear frequency grid is utilized to estimate the set Ω. This frequency grid will be considered throughout this dissertation for the H_∞, H_2 and mixed H_2/H_∞ control design problems.

If it is desired to constraint the H_∞ norm given in Eq. (5.46), the goal is to find a controller such that Eq. (5.48) holds for a given value of γ. Using the stable factorizations' coefficients ρ_x and ρ_y mentioned in Eqs. (5.13) and (5.14) to factorize the controller $K_{n \times 1}(z)$, Eq. (5.48) becomes a convex function of the coefficients ρ_x and ρ_y.

However, if the objective is to minimize the H_∞ norm, the value of γ which is the upper-bound of the H_∞ norm in Eq. (5.47) should be minimized. In this case, γ, ρ_x, ρ_y are all optimization variables and Eq. (5.48) will become nonlinear in terms of these variables. Therefore, the following iterative bisection algorithm[42] is used to solve this problem.

- 1) Pick a value for γ, which can obtain a feasible solution to Eq. (5.48).

- 2) Given γ, find ρ_x, ρ_y such that Eq. (5.48) is satisfied.

- 3) Given ρ_x, ρ_y, find the minimum value for γ such that Eq. (5.48) is satisfied.

- 4) Go back to step 2 until the difference between the value of γ in step 2 and 3 is smaller than a desired threshold.

The iterative bisection algorithm will not necessarily converge to the global optimal solution. Therefore, the controller obtained using this algorithm may only locally minimize the H_∞ norm given in Eq. (5.46).

The convex condition proposed in theorem 5.3.1 is a necessary and sufficient condition for the H_∞ norm criterion given in Eq. (5.47). In [41], a sufficient convex condition has been proposed for this criterion. For comparison purposes, this results is reviewed in the following theorem for MISO systems, but it is applicable to MIMO systems [41]. The controller design results based on theorems 5.3.1 and 5.3.2 are compared in chapter 6.

Theorem 5.3.2. *Assume that the frequency response data for the plant $G_{1\times n}(\omega)$ with n inputs and one output is given over the frequency region Ω, and is factorized according to Eq. (5.1). Given a positive scalar γ and the initial stabilizing controller $K_0(z) = X_0(z)Y_0(z)^{-1}$, the H_∞ constraint given in Eq. (5.47) is satisfied, if there exists controller stable factorizations $X(z)\big|_{z=e^{j\omega}}, Y(z)\big|_{z=e^{j\omega}}$ according to Eq. (5.2), such that the following LMI is satisfied*

$$\forall \omega \in \Omega : \begin{bmatrix} P^\star P_0 + P_0^\star P - P_0^\star P_0 & (W_{U_{w\to u}}X\tilde{N})^\star \\ W_{U_{w\to u}}X\tilde{N} & \gamma I_n \end{bmatrix} \succ 0 \tag{5.49}$$

where

$$P = \tilde{N}X + \tilde{M}Y, \tag{5.50}$$

and

$$P_0 = \tilde{N}X_0 + \tilde{M}Y_0. \tag{5.51}$$

Proof: See [41].

This algorithm requires an initial stabilizing controller $K_0(z)$. Moreover, the resulting controller $K(z) = X(z)Y^{-1}(z)$ does not necessarily stabilize the closed loop system. Theorem 5.3.4, which is reviewed in the next section and has been proposed in [41], will be used to guarantee closed loop stability.

A single set of plant measurement is considered in theorems 5.3.1 and 5.3.2. As mentioned in section 5.2, an H_∞ constraint norm for multiple plant measurements is defined to be the worst H_∞ norm. Therefore, theorem 5.3.1 can be extended for multiple plant measurements by replacing Eq. (5.48) with the following set of inequalities

$$\forall i, \ \forall \omega \in \Omega : \gamma^{-1}\bar{\sigma}(\ W_{U_{w\to u}}(\omega)X(e^{j\omega})\tilde{N}_i(\omega)\ ) < Re(\ \tilde{N}_i(\omega)X(e^{j\omega}) + \tilde{M}_i(\omega)Y(e^{j\omega})\ ), \tag{5.52}$$

where i represents the i's plant measurement, and $\tilde{M}_i$ and $\tilde{N}_i$ represent stable factorizations for that measurement. Similarly, theorem 5.3.2 can be extended for multiple plant measurements by replacing Eqs. (5.61)-(5.51) with the following set of Linear Matrix Inequalities (LMIs)

$$\forall \omega \in \Omega : \begin{bmatrix} P_i^\star P_{0,i} + P_{0,i}^\star P_i - P_{0,i}^\star P_{0,i} & (W_{U_{w\to u}}X\tilde{N}_i)^\star \\ W_{U_{w\to u}}X\tilde{N}_i & \gamma I_n \end{bmatrix} \succ 0, \tag{5.53}$$

$$P_i = \tilde{N}_iX + \tilde{M}_iY, \tag{5.54}$$

and

$$P_{0,i} = \tilde{N}_iX_0 + \tilde{M}_iY_0. \tag{5.55}$$

As one can observe from Eq. (5.52) or Eqs. (5.53)-(5.55), the goal is to find a common value of γ and controller coefficients ρ_x and ρ_y for all the plant measurements, and the value of γ will represent the upper-bound for the worst H_∞ norm of all the plant measurements.

Data-driven H_2 control design

The data-driven H_2 control design methodology used here was developed in [41] for MIMO systems, where a convex upper-bound for the H_2 norm is obtained using an affine approximation of quadratic terms [41, 71]. The H_2 constraint or minimization control objectives defined in Eqs. (5.35) and (5.36) are imposed by constraining or minimizing this upper-bound. Consider the following H_2 norm for the MISO system given in Fig. 5.1

$$H_2 = Q_{E_{r \to e}} \|E_{r \to e}\|_2^2 + Q_{U_{r \to u}} \|U_{r \to u}\|_2^2, \tag{5.56}$$

where $E_{r \to e}$ is a SISO and $U_{r \to u}$ is a SIMO transfer function. $Q_{E_{r \to e}}$ and $Q_{U_{r \to u}}$ are scalar weighting functions. The upper-bound for the H_2 norm defined in Eq. (5.56) can be written as

$$H_2 \leqslant \int_\Omega [Q_{E_r} Tr(\Gamma_{E_{r \to e}}) + Q_{U_{r \to u}} Tr(\Gamma_{U_{r \to u}})] \, d\omega, \tag{5.57}$$

where $\Gamma_{E_{r \to e}}(\omega) \in \mathbb{R}$ and $\Gamma_{U_{r \to u}}(\omega) \in \mathbb{R}^{n \times n}$ are the positive definite variables. Theorem 5.3.3 was developed in [41] to impose constraint on this upper-bound of the H_2 norm. Please note that the upper-bound for any other closed loop transfer functions can be formulated in a similar fashion.

Theorem 5.3.3. *Assume that the frequency response data for the plant $G_{1 \times n}(\omega)$ with n inputs and one output is given over the frequency region Ω, and is factorized according to Eq. (5.1). Given a positive scalar η and an initial stabilizing controller $K_0(z) = X_0(z)Y_0(z)^{-1}$, the H_2 norm defined in Eq. (5.56) and its upper-bound in Eq. (5.57) are constrained by η*

$$H_2 \leqslant \int_\Omega [Q_{E_r} Tr(\Gamma_{E_{r \to e}}) + Q_{U_{r \to u}} Tr(\Gamma_{U_{r \to u}})] \, d\omega \leqslant \eta, \tag{5.58}$$

if Eq. (5.58) is satisfied and there exists controller stable factorizations $X(z)\big|_{z=e^{j\omega}}, Y(z)\big|_{z=e^{j\omega}}$ according to Eq. (5.2), such that the following LMIs are satisfied

$$\forall \omega \in \Omega : \begin{bmatrix} \Gamma_{E_{r \to e}} & Y\tilde{M} \\ \tilde{M}^\star Y^\star & P^\star P_0 + P_0^\star P - P_0^\star P_0 \end{bmatrix} \succ 0 \tag{5.59}$$

and

$$\forall \omega \in \Omega : \begin{bmatrix} \Gamma_{U_{r \to u}} & X\tilde{M} \\ \tilde{M}^\star X^\star & P_k^\star P_0 + P_0^\star P - P_0^\star P_0 \end{bmatrix} \succ 0. \tag{5.60}$$

where P and P_0 are defined in Eqs. (5.50) and (5.51), respectively.

Proof: See [41].

Theorem 5.3.3 imposes a sufficient convex condition on the upper-bound of the H_2 norm defined in Eq. (5.57) using the variable η. This variable can be utilized to either constraint or minimize the H_2 norm upper-bound according to Eqs. (5.35) and (5.36).

Notice that the algorithm in theorem 5.3.3 uses the initial controller to find the current controller. Therefore, the H_2 norm conditions in Eqs (5.59) and (5.60) can be reformulated as an iterative approach by replacing those equations with the following equations

$$\forall \omega \in \Omega : \begin{bmatrix} \Gamma_{E_{r \to e}} & Y_k \tilde{M} \\ \tilde{M}^\star Y_k^\star & P_k^\star P_{k-1} + P_{k-1}^\star P_k - P_{k-1}^\star P_{k-1} \end{bmatrix} \succ 0, \tag{5.61}$$

and

$$\forall \omega \in \Omega : \begin{bmatrix} \Gamma_{U_{r \to u}} & X_k \tilde{M} \\ \tilde{M}^\star X_k^\star & P_k^\star P_{k-1} + P_{k-1}^\star P_k - P_{k-1}^\star P_{k-1} \end{bmatrix} \succ 0, \tag{5.62}$$

where the subscript k is representing the iteration number and the parameter P_k is defined as follows

$$P_k = \tilde{N} X_k + \tilde{M} Y_k. \tag{5.63}$$

In this iterative approach, the controller stable factorizations X_{k-1} and Y_{k-1} from the previous iteration $k-1$ are used to find the stable factorizations X_k and Y_k for the current iteration k. Therefore, the controller is obtained by iterating over its stable factorizations. According to [41, 71], the following two properties can be proved for this iterative approach.

- 1) If the algorithm converges, this upper-bound converges to the real value of the H_2 norm defined in Eq. (5.56).

- 2) Considering the minimization of the H_2 norm upper-bound defined in Eq. (5.57), the value of the upper-bound is guaranteed to decrease at each iteration.

Theorem 5.3.3 can be used to obtain a controller which impose H_2 constraint or minimization objectives on the upper-bound of the H_2 norm in terms of convex conditions. However, the obtained controller does not necessarily stabilize the closed loop system. Therefore, the following theorem has been proposed in [41] to guarantee closed loop stability.

Theorem 5.3.4. *Given a strictly proper plant G, an initial stabilizing controller $K_0 = X_0 Y_0^{-1}$ and a feasible solution to the following LMI,*

$$\forall \omega \in \Omega : P^* P_0 + P_0^* P \succ 0 \tag{5.64}$$

where P_0 and P are defined in Eqs. (5.50) and (5.51), and $K = XY^{-1}$. The controller K stabilizes the closed loop system, if

- *The initial controller K_0 and the controller K share the same poles on the unit circle.*

- *The following inequality holds.*

$$\forall \omega \in \Omega : Y^\star Y_0 + Y_0^\star Y - Y_0^\star Y_0 \succ 0 \tag{5.65}$$

Proof: See [41].

Another approach to guarantee the closed loop stability is to consider the mixed H_2/H_∞ control problem, where the convex condition for the H_∞ norm criterion developed in theorem 5.3.1 guarantees the closed loop stability. The mixed H_2/H_∞ control design will be illustrated in the next section.

The above H_2 control design methodology was developed for a single plant measurement. In the case of multiple plant measurements, as mentioned in section 5.2, the H_2 norm criteria can be defined either as the worst H_2 norm or as the average H_2 norm. Considering l plant measurements with stable factorizations $\tilde{M}_i$ and $\tilde{N}_i$ where i represents the $i's$ measurement, the H_2 norm upper-bound will be defined as follows.

- Worst case H_2 norm: The worst case H_2 norm for l measurements is denoted as H_2^{worst} and is defined as follows

$$H_2^{\text{worst}} = \max_{i \in \{1,2,..,l\}} Q_{E_{r \to e}} \|E_{r \to e,i}\|_2^2 + Q_{U_{r \to u}} \|U_{r \to u,i}\|_2^2. \tag{5.66}$$

where $E_{r \to e,i}$ and $U_{r \to u,i}$ represent the closed loop transfer functions from r to e and u in Fig. 5.1 using the $i's$ plant measurement. In this case, common positive definite frequency based variables, Γ_{S_r} and Γ_{U_r}, are considered for all the measurements. Therefore, Eqs. (5.58), (5.61) and (5.62) can be rewritten as follows.

$$H_2^{\text{worst}} \leqslant \int_\Omega [Q_{E_{r \to e}} Tr(\Gamma_{E_{r \to e}}) + Q_{U_{r \to u}} Tr(\Gamma_{U_{r \to u}})] \, d\omega \leqslant \eta \tag{5.67}$$

where,

$$\forall i \in 1,..,l, \ \forall \omega \in \Omega : \begin{bmatrix} \Gamma_{E_{r \to e}} & Y_k \tilde{M}_i \\ \tilde{M}_i^\star Y_k^\star & P_{k,i}^\star P_{k-1} + P_{k-1,i}^\star P_{k,i} - P_{k-1,i}^\star P_{k-1,i} \end{bmatrix} \succ 0, \tag{5.68}$$

$$\forall i \in 1,..,l, \ \forall \omega \in \Omega : \begin{bmatrix} \Gamma_{U_{r \to u}} & X_k \tilde{M}_i \\ \tilde{M}_i^\star X_k^\star & P_{k,i}^\star P_{k-1,i} + P_{k-1,i}^\star P_{k,i} - P_{k-1,i}^\star P_{k-1,i} \end{bmatrix} \succ 0 \tag{5.69}$$

and also

$$P_{k,i} = \tilde{N}_i X_k + \tilde{M}_i Y_k. \tag{5.70}$$

- Average H_2^{average} norm: The average H_2 norm for l measurements is denoted as H_2^{average} and is defined as follows

$$H_2^{\text{average}} = \frac{1}{l} \sum_{i=1}^l Q_{E_{r \to e}} \|E_{r \to e,i}\|_2^2 + Q_{U_{r \to u}} \|U_{r \to u,i}\|_2^2. \tag{5.71}$$

In this case, for each individual measurement i, the positive definite frequency based variables $\Gamma_{E_{r \to e}}^i$ and $\Gamma_{U_{r \to u}}^i$ are defined. Therefore, Eqs. (5.58), (5.61) and (5.62) can be written as follows

$$H_2^{\text{average}} \leqslant \frac{1}{l} \sum_{i=1}^l \int_\Omega [Q_{E_{r \to e}} Tr(\Gamma_{E_{r \to e}}^i) + Q_{U_{r \to u}} Tr(\Gamma_{U_{r \to u}}^i)] \, d\omega \leqslant \eta \tag{5.72}$$

where,

$$\forall i \in 1,..,l, \ \forall \omega \in \Omega : \begin{bmatrix} \Gamma^i_{E_{r \to e}} & Y_k \tilde{M}_i \\ \tilde{M}^\star_i Y^\star_k & P^\star_{k,i} P_{k-1} + P^\star_{k-1,i} P_{k,i} - P^\star_{k-1,i} P_{k-1,i} \end{bmatrix} \succ 0, \qquad (5.73)$$

$$\forall i \in 1,..,l, \ \forall \omega \in \Omega : \begin{bmatrix} \Gamma^i_{U_{r \to e}} & X_k \tilde{M}_i \\ \tilde{M}^\star_i X^\star_k & P^\star_{k,i} P_{k-1,i} + P^\star_{k-1,i} P_{k,i} - P^\star_{k-1,i} P_{k-1,i} \end{bmatrix} \succ 0, \qquad (5.74)$$

and also $P_{k,i}$ is given in Eq. (5.70).

The H_2 norm can be either minimized or constrained by imposing minimization or constraint criteria on the upper-bound of the H_2 norm given in Eqs. (5.58), (5.67) and (5.72). The inequalities in these equations are linear in terms of unknown variables which are $\Gamma_{E_{r \to e}}$, $\Gamma_{U_{r \to u}}$, ρ_x and ρ_y and η. Moreover, the inequalities given in Eqs. (5.61), (5.62), (5.68), (5.69), (5.73) and (5.74) are all linear matrix inequalities ($LMIs$). Therefore, the H_2 control problem can be formulated as a convex optimization problem. The convex optimization solvers are used to solve this problem. However, the solver should be capable of handling the LMIs as the constraints.

Data-driven mixed H_2/H_∞ control design

The convex conditions for either H_2 and H_∞ control design criteria are illustrated above. These H_2 and H_∞ criteria can be combined to form a mixed H_2/H_∞ control design problem. The main advantage of mixing the H_2 and H_∞ norm criteria is the capability of considering both these criteria in the controller design step.

In order to formulate the mixed H_2/H_∞ control design problem, the sufficient convex conditions for the H_2 norm criteria in theorem 5.3.3 are used to impose the H_2 norm constraints or minimization objectives. The conditions for the H_∞ norm criteria are imposed by using the necessary and sufficient convex conditions in theorem 5.3.1, or the sufficient conditions in theorem 5.3.2. The H_∞ conditions in theorem 5.3.1 will guarantee the closed loop stability, while the conditions in theorem 5.3.2 cannot guarantee the closed loop stability without considering the additional conditions given in theorem 5.3.4. Moreover, the H_∞ conditions in theorem 5.3.1 are necessary and sufficient, while the H_∞ conditions in theorem 5.3.2 are only sufficient. Therefore, the controller design algorithm in the next chapter mainly utilizes theorem 5.3.1 for imposing the H_∞ criteria as part of the mixed H_2/H_∞ control design problem. However in section 6.4, the design results for the mixed H_2/H_∞ control problem, when theorem 5.3.1 is utilized are compared with the corresponding results when theorem 5.3.2 is used instead of theorem 5.3.1.

Here as an example, the following mixed H_2/H_∞ control design problem is considered.

$$\begin{aligned} \min_{X_k \in \mathbb{RH}_\infty^{n \times 1}, Y_k \in \mathbb{RH}_\infty} \quad & H_{2, \text{ objective}} \quad \text{defined in Eq. (5.42) or Eq. (5.44)} \\ \text{subject to} \quad & H_{\infty, \text{ constraints}} \quad \text{defined in Eq. (5.39),} \\ & H_{2, \text{ constraints}} \quad \text{defined in Eq. (5.41) or Eq. (5.43).} \end{aligned} \qquad (5.75)$$
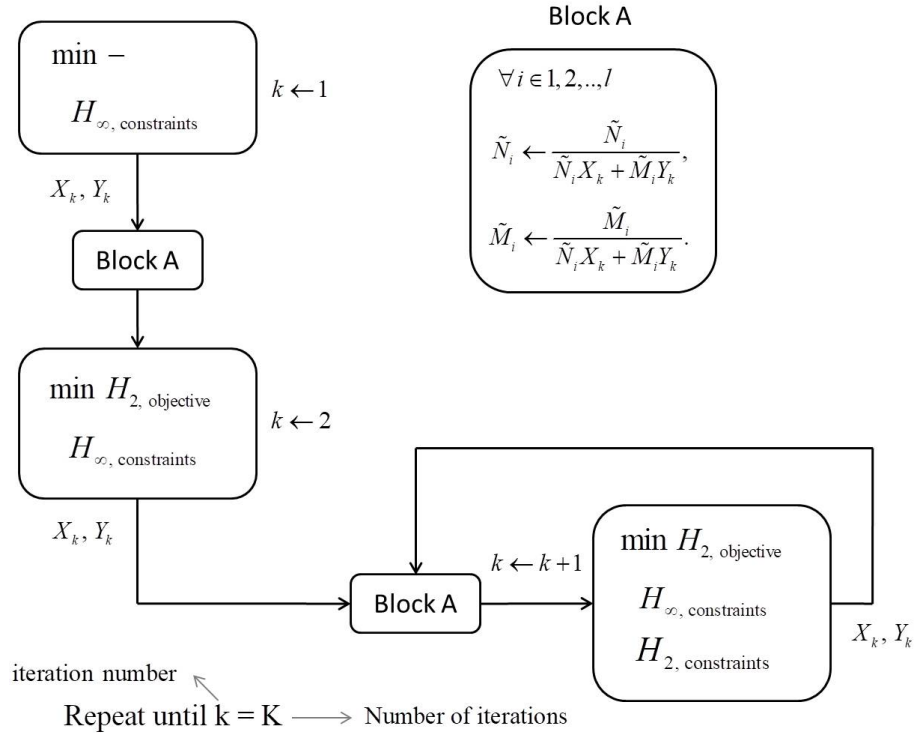
Figure 5.2: Mixed H_2/H_∞ design algorithm flowchart.

where the objective is the minimization of $H_{2,\text{ objective}}$ norm, subject to constraints imposed in terms of H_∞ and H_2 norms.

The mixed H_2/H_∞ control design scenario uses the design algorithm flowchart shown in Fig. 5.2. In this flowchart, k represents the iteration number and K is the total number of iterations used for obtaining the final iteration of the controller. $X_k(e^{j\omega}) \in \mathbb{C}^{n\times 1}$ and $Y_k(e^{j\omega}) \in \mathbb{C}$ are the frequency responses of the controller factorizations, which are transfer functions or polynomial in the z domain, evaluated at $z = e^{j\omega}$. On the other hand, $\tilde{N}_i(\omega) \in \mathbb{C}^{1\times n}$, $\tilde{M}_i(\omega) \in \mathbb{C}$ are frequency response data points of stable factorizations of the i's plant measurement.

The very first step to design a mixed H_2/H_∞ controller is to design a controller which satisfies the $H_{\infty,\text{ constraints}}$. The H_∞ control design algorithm proposed in theorem 5.3.1 stabilizes the closed loop system. Therefore, the roots of the common denominator for all the closed loop transfer functions, $\tilde{N}_i(\omega)X_k(e^{j\omega}) + \tilde{M}_i(\omega)Y_k(e^{j\omega})$, will be inside the unit circle. This common denominator obtained at iteration k is used to normalize the plant

factorizations at iteration $k + 1$ as follows

$$\forall i \in 1, .., l, \ \forall \omega \in \Omega :$$

$$\tilde{N}_i(\omega) \leftarrow \frac{\tilde{N}_i(\omega)}{\tilde{N}_i(\omega)X_k(e^{j\omega}) + \tilde{M}_i(\omega)Y_k(e^{j\omega})},$$

$$\tilde{M}_i(\omega) \leftarrow \frac{\tilde{M}_i(\omega)}{\tilde{N}_i(\omega)X_k(e^{j\omega}) + \tilde{M}_i(\omega)Y_k(e^{j\omega})},$$

(5.76)

where $\tilde{N}_i(\omega)$ and $\tilde{M}_i(\omega)$ on the left side of the arrows represent the plant factorizations used at iteration $k+1$. The next step is to design a controller which minimizes the $H_{2, \text{ objective}}$ subject to $H_{\infty, \text{ constraints}}$. Finally, the $H_{2, \text{ constraints}}$ will be included in the optimization problem and according to the flowchart, this optimization problem will be iterated over for the remaining iterations. The main reason for the step by step inclusion of the $H_{2, \text{ objective}}$ and $H_{2, \text{ constraints}}$ is that the convex condition of the H_2 norm is a sufficient and not a necessary solution, and depends on the plant factorizations $\tilde{M}_i(\omega)$, $\tilde{N}_i(\omega)$. Therefore, the normalizations of these parameters in Eq. (5.76) can be helpful in avoiding locally optimal solutions.

Chapter 6

Application of Data Driven Control Design to HDDs

In this chapter, the data-driven mixed H_2/H_∞ algorithm proposed in chapter 5 is used to design a track-following controller for a dual-stage HDD. The dual-stage HDD actuators have several resonance modes [9, 37]. In most model-based robust control design methodologies, including each of these resonance modes in the actuator models directly increases the controller order [72]. However by using the data-driven control methodology, all these modes are already included in the system frequency response measurements and will be considered in the controller design step without any direct effect on the controller order [14].

The feedback structure considered for the dual-stage HDD control design is presented in section 6.1. The feedback block is a SIMO controller with the sensitivity decoupling structure. However, the controllers inside this block will be designed using two different control synthesis strategies: the sequential SISO and SIMO data-driven design strategies, and the results obtained from these strategies will be compared with each other. In the sequential SISO design strategy, the dual-stage closed loop system is decoupled into two SISO loops, and SISO controllers are sequentially synthesized for each loop. On the other hand, the SIMO design strategy will design a SIMO controller for the MISO plant in one step.

The control objectives for the dual-stage HDD, represented in terms of H_∞ and H_2 norms of closed loop transfer functions, are defined in section 6.2. These control objectives are converted into convex optimization problems in section 6.3 for both sequential SISO and SIMO design strategies. In section 6.4, the controllers are designed by solving these optimization problems for five sets of actuators' frequency response measurements, and the designed controllers using both the sequential SISO and SIMO design strategies are compared.
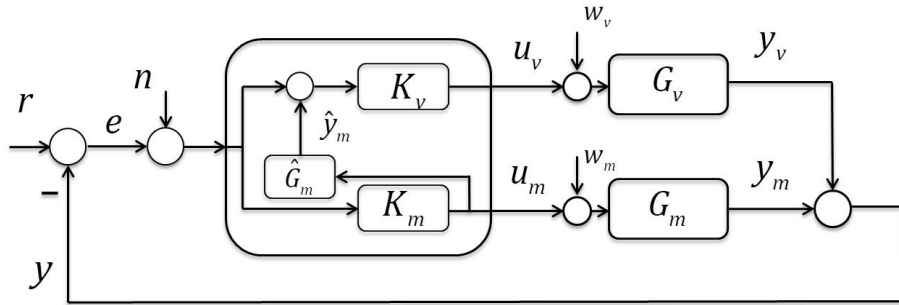
Figure 6.1: Sensitivity decoupling control Structure for a dual-stage HDD. $\hat{G}_m(z)$ represents an estimated Mili-Actuator (MA) transfer function.

6.1 Feedback Structure

The structure of a dual-stage HDD has been described in chapter 2. The Voice Coil Motor (VCM) and Mili-Actuator (MA) are the two actuators used for nano-positioning the head on the data tracks. These two actuators are respectively denoted as G_v and G_m in the dual-stage feedback structure shown in Fig. 6.1. In this block diagram, there are four sources of external noises and disturbances considered to be applied on the HDD. n is contaminating the position error, e, and is called the measurement noise. w_v and w_m are the control input noises and the r is the track run-out. The major sources for these noises and disturbances are the windage caused by the rotation of the magnetic disk, external vibrations and also the measurement noises.

The HDD actuators have uncertain dynamics, primarily consisting of resonance modes at high frequency regions, which make the control design problem challenging. The data-driven control design introduced in chapter 5 uses several actuator measurements as the representative of plant uncertainties and a controller is synthesized that stabilizes the closed loop system and achieves the desired performance characteristics for all the measurements. These performance characteristics are considered to be in terms of H_∞ and H_2 norms of closed loop transfer functions, where these norms can be constrained or minimized.

The common control structure used in the dual-stage HDD is the sensitivity decoupling structure illustrated in Fig. 6.1. As mentioned in chapter 2, the main advantage of using the sensitivity decoupling structure is that the sensitivity transfer function for the dual-stage structure, $E_{r\rightarrow e}$, can be written as the product of VCM and MA sensitivity transfer functions. Moreover, in the case of a MA failure, the signals u_m and $\hat{y}_m$ in Fig. 6.1 will be disconnected, and the HDD will perform as a single-stage HDD as shown in Fig. 6.2. The effect of the MA control input noise w_m on the VCM single-stage closed loop signals will not be considered in the controller design, since it is assumed that the effect of control input noises are lumped into the track run-out and measurement noise spectrum. This is a standard practice for designing a track following controller in the hard disk drive industry. However, if the noise spectrum for the MA control input noise is known, the transfer functions from the MA
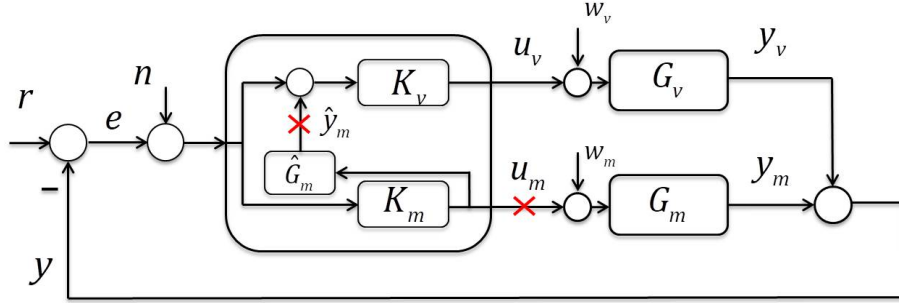
Figure 6.2: The single-stage HDD with VCM as the actuator. The cross-marks determine the signals which will be eliminated when switching to the single-stage actuation. The values of these signals will be zero.

control input noise to different closed loop signals can be included in the design process.

The sensitivity decoupling control structure depicted in Fig. 6.1 should be designed such that both the dual-stage and single-stage loops respectively depicted in Figs. 6.1 and 6.2 are stable and achieve the desired control objectives presented in section 6.2. The following two control design strategies are used to synthesize the controllers in the sensitivity decoupling structure.

- *Sequential SISO design strategy*: This is a two step design process. In the first step, the VCM SISO compensator K_v is designed for the single-stage loop given in Fig. 6.2. Then in the next step, the compensator K_v is fixed and the MA SISO compensator K_m for the dual-stage loop in Fig. 6.1 is designed.

- *SIMO design strategy*: In this design strategy, both the VCM compensator K_v and the MA compensator K_m are designed simultaneously. The controller block diagram in the sensitivity decoupling structure given in Fig. 6.1 can be expressed as follows

$$\bar{K} = \begin{bmatrix} \bar{K}_1 \\ \bar{K}_2 \end{bmatrix} = \begin{bmatrix} K_v(1 + K_m \hat{G}_m) \\ K_m \end{bmatrix}. \tag{6.1}$$

As a result, the sensitivity decoupling compensators K_v and K_m will be obtained in terms of $\bar{K}$.

$$K_v = \frac{\bar{K}_1}{1 + \bar{K}_2 \hat{G}_m}, \tag{6.2}$$

$$K_m = \bar{K}_2. \tag{6.3}$$

In the SIMO design strategy, the SIMO controller $\bar{K}$ is designed such that it stabilizes and achieves the desired control objectives for both the VCM single-stage loop in Fig. 6.2 and the dual-stage loop in Fig. 6.1. Subsequently, the compensators K_v and K_m, are obtained as a function of $\bar{K}$ utilizing Eqs. (6.2) and (6.3).

6.2 Control Objectives

The data-driven control methodology presented in chapter 5 will consider the control objectives in terms of H_∞ and H_2 norms of closed loop transfer functions in the frequency domain. The H_∞ norms will shape the frequency responses of the closed loop transfer functions and also guarantee closed loop stability. The H_2 norms of closed loop transfer functions will be used to constraint and/or minimize the variances of the corresponding signals in the time domain.

H_∞ norm

The H_∞ norm of closed loop transfer functions for both the dual-stage and the single-stage loops in Figs. 6.1 and 6.2 will be constrained. According to theorem 5.3.1, these constraints will guarantee closed loop stability for both of these loops.

The following H_∞ norm constraints for the single-stage HDD in Fig. 6.2 will be imposed.

$$\forall i \in 1,..,l: \quad \left\|W_{E^s_{r \to e}} E^s_{(r \to e)i}\right\|_\infty \quad < 1, \quad \left\|W_{U^s_{r \to u_v}} U^s_{(r \to u_v)i}\right\|_\infty \quad < 1, \\ \left\|W_{E^s_{w_v \to e}} E^s_{(w_v \to e)i}\right\|_\infty \quad < 1, \quad \left\|W_{U^s_{w_v \to u_v}} U^s_{(w_v \to u_v)i}\right\|_\infty \quad < 1. \tag{6.4}$$

where $W_H(\omega) \in \mathbb{C}^{o \times p}$ is a bounded weighting function in the frequency domain for the closed loop transfer function $H_{p \times q}$, and the frequency argument (ω) is eliminated from the notation for simplicity. The superscript H^s represents the closed loop transfer functions for the single-stage HDD, which utilizes only the VCM loop, as depicted in Fig 6.2. The closed loop transfer functions are denoted using upper-case letters, with their subscripts within parenthesis representing the input to output causality, while the subscript i represents the closed loop response using the ith frequency response data. l denotes the total number of frequency response data sets used to synthesize the controller. As an example, $E^s_{(w_v \to e)2}$ denotes the closed loop transfer function from input w_v to output e in the block diagram in Fig. 6.2 using the second frequency response data set. As mentioned in chapter 5, these weighting functions can be any bounded numerically shaped weighting functions.

The H_∞ norm constraints for the dual-stage HDD in Fig. 6.1 can be considered in a similar fashion to Eq. (6.4).

$$\forall i \in 1,..,l: \quad \left\|W_{E_{r \to e}} E_{(r \to e)i}\right\|_\infty \quad < 1, \quad \left\|W_{U_{r \to u}} U_{(r \to u)i}\right\|_\infty \quad < 1, \\ \left\|W_{E_{w \to e}} E_{(w \to e)i}\right\|_\infty \quad < 1, \quad \left\|W_{U_{w \to u}} U_{(w \to u)i}\right\|_\infty \quad < 1, \tag{6.5}$$

where

$$u = \begin{bmatrix} u_v \\ u_m \end{bmatrix}, \tag{6.6}$$

and

$$w = \begin{bmatrix} w_v \\ w_m \end{bmatrix}. \tag{6.7}$$

Since the control input as well as control input disturbance have two components, the closed-loop transfer functions in Eq. (6.5) are not necessarily SISO transfer functions and the H_∞ norm constraints will shape their maximum singular values across the frequency regions as explained in section 5.2.

If it is desired to shape the magnitude of individual SISO closed loop transfer functions in the dual-stage settings, the H_∞ norm for that specific SISO transfer function can be considered. The closed loop transfer functions $E_{(w \to e)i}$, $U_{(r \to u)i}$ and $U_{(w \to u)i}$ all have multiple inputs or multiple outputs. Therefore, the closed loop SISO transfer functions for each individual elements of these transfer functions will be considered. The individual closed loop transfer functions for the tracking error are

$$\forall i \in 1, .., l : \quad \left\|W_{E_{w_v \to e}} E_{(w_v \to e)i}\right\|_\infty < 1, \quad \left\|W_{E_{w_m \to e}} E_{(w_m \to e)i}\right\|_\infty < 1, \tag{6.8}$$

and for the control inputs are

$$\forall i \in 1, .., l :$$
$$\left\|W_{U_{r \to u_v}} U_{(r \to u_v)i}\right\|_\infty \; < 1, \; \left\|W_{U_{w_v \to u_v}} U_{(w_v \to u_v)i}\right\|_\infty \; < 1, \; \left\|W_{U_{w_m \to u_v}} U_{(w_m \to u_v)i}\right\|_\infty \; < 1,$$
$$\left\|W_{U_{r \to u_m}} U_{(r \to u_m)i}\right\|_\infty \; < 1, \; \left\|W_{U_{w_v \to u_m}} U_{(w_v \to u_m)i}\right\|_\infty \; < 1, \; \left\|W_{U_{w_m \to u_m}} U_{(w_m \to u_m)i}\right\|_\infty \; < 1. \tag{6.9}$$

H_2 norm

The primary control objective in the HDD is to minimize the variance of the position tracking error, $E[e^2(k)] = \|e\|_2^2$, despite the existence of all the disturbances in the system. We will assume that the disturbances r, n, w_v and w_m shown in Fig. 6.1 can be accurately described by filtering uncorrelated unit variance white noises through the transfer functions $R(\omega)$, $N(\omega)$, $W_v(\omega)$ and $W_m(\omega)$, respectively. Therefore, the average variance of the tracking error for the dual-stage loop will be expressed using the H_2 norms of closed loop transfer functions in the frequency domain

$$\frac{1}{l} \sum_{i=1}^{l} \|e_i\|_2^2 = \frac{1}{l} \sum_{i=1}^{l} \left(\; \left\|E_{(r \to e)i}R\right\|_2^2 + \left\|E_{(n \to e)i}N\right\|_2^2 + \left\|E_{(w_v \to e)i}W_v\right\|_2^2 + \left\|E_{(w_m \to e)i}W_m\right\|_2^2 \; \right).$$
$$\tag{6.10}$$

where i denotes the ith frequency response data set. The average variance of the tracking error for the single-stage VCM loop depicted in Fig. 6.2 will be expressed in a similar fashion

$$\frac{1}{l} \sum_{i=1}^{l} \|e_i^s\|_2^2 = \frac{1}{l} \sum_{i=1}^{l} \left(\; \left\|E_{(r \to e)i}^s R\right\|_2^2 + \left\|E_{(n \to e)i}^s N\right\|_2^2 + \left\|E_{(w_v \to e)i}^s W_v\right\|_2^2 \; \right). \tag{6.11}$$

The SIMO and sequential SISO control design strategies, which were introduced in section 6.1, will be used to synthesize the dual-stage controller in Fig. 6.1. In the SIMO control

strategy, the VCM compensator K_v and the MA compensator K_m are simultaneously designed in order to minimize the dual-stage H_2 tracking error criterion in Eq. (6.10) under H_∞ and H_2 constraints. In the sequential SISO control strategy, the VCM compensator K_v is first synthesized in order to minimize the SISO H_2 tracking criterion in Eq. (6.11) under H_∞ and H_2 constraints. Subsequently, K_v is kept fixed and the MA compensator K_m is synthesized in order to minimize the H_2 criterion in Eq. (6.10) under H_∞ and H_2 constraints.

It is also necessary to constrain the average variances of several signals to take into account actuator limitations. There is a limitation on the amplitude of the VCM control input signal in the time domain and its average variance has to be constrained. The following equations constrain the average variance of the VCM control input in terms of H_2 norms in the frequency domain for the single-stage VCM feedback loop depicted in Fig. 6.2

$$\frac{1}{l}\sum_{i=1}^{l}\|u_{vi}^s\|_2^2 =$$
$$\frac{1}{l}\sum_{i=1}^{l}\left(\ \left\|U_{(r\to u_v)i}^s R\right\|_2^2 + \left\|U_{(n\to u_v)i}^s N\right\|_2^2 + \left\|U_{(w_v\to u_v)i}^s W_v\right\|_2^2\ \right) < \eta_{u_v^s}, \tag{6.12}$$

and for the dual-stage feedback loop depicted in Fig. 6.1

$$\frac{1}{l}\sum_{i=1}^{l}\|u_{vi}\|_2^2 =$$
$$\frac{1}{l}\sum_{i=1}^{l}\left(\ \left\|U_{(r\to u_v)i} R\right\|_2^2 + \left\|U_{(n\to u_v)i} N\right\|_2^2 + \left\|U_{(w_v\to u_v)i} W_v\right\|_2^2 + \left\|U_{(w_m\to u_v)i} W_m\right\|_2^2\ \right) < \eta_{u_v}. \tag{6.13}$$

In the case of the MA, there are limitations on the amplitude of the MA control input as well as the MA output signals in the time domain. Therefore, the average variances of these two signals have to be constrained. Here for simplicity, only the average variance of the MA output will be constrained. However if necessary, the average variance of the MA input can also be considered as an additional constraint. The MA is only used in the dual-stage feedback loop depicted in Fig. 6.1, and the average variance of its output can be constrained in terms of H_2 norms in the frequency domain as follows

$$\frac{1}{l}\sum_{i=1}^{l}\|y_{mi}\|_2^2 =$$
$$\frac{1}{l}\sum_{i=1}^{l}\left(\ \left\|Y_{(r\to y_m)i} R\right\|_2^2 + \left\|Y_{(n\to y_m)i} N\right\|_2^2 + \left\|Y_{(w_v\to y_m)i} W_v\right\|_2^2 + \left\|Y_{(w_m\to y_m)i} W_m\right\|_2^2\ \right) < \eta_{y_m}. \tag{6.14}$$

The positive upper-bounds $\eta_{u_v^s}$, η_{u_v} and η_{y_m} are selected by the designer and will be specified in section 6.4.

6.3   Control Algorithms

In the previous section, the mixed H_2/H_∞ control objectives were defined by the general optimization problem given in Eq. (5.75). In this section, this general optimization problem will be specified in terms of the dual-stage feedback structure given in Fig. 6.1. The optimization problem will then be solved using both the sequential SISO and SIMO control design strategies described in section 6.1.

These optimization problems are formulated as convex optimization problems. The convex conditions for the control objectives defined in terms of H_∞ and H_2 norms were derived in section 5.3. The H_∞ norms control objectives are converted into their necessary and sufficient convex conditions, and the H_2 norms control objectives are approximated by their sufficient convex conditions.

In the sequential SISO design strategy, first the VCM compensator K_v is designed considering the single-stage VCM loop depicted in Fig. 6.2. The optimization problem that will be solved to synthesize K_v is

$$\begin{aligned}
\text{minimize} \quad & \frac{1}{l} \sum_{i=1}^{l} \|e_i^s\|_2^2 \text{ defined in Eq.}(6.11) \\
\text{subject to} \quad & \text{Eqs. } (6.4), \\
& \text{Eqs. } (6.12) \ .
\end{aligned} \tag{6.15}$$

After the VCM compensator K_v has been designed, the MA compensator K_m is subsequently designed considering the dual-stage loop depicted in Fig. 6.1 and fixing the compensator K_v. The optimization problem that will be solved to synthesize K_m, while keeping K_v fixed is

$$\begin{aligned}
\text{minimize} \quad & \frac{1}{l} \sum_{i=1}^{l} \|e_i\|_2^2 \text{ defined in Eq.}(6.10) \\
\text{subject to} \quad & \text{Eqs. } (6.5), \ (6.8), \ (6.9), \\
& \text{Eqs. } (6.13), \ (6.14).
\end{aligned} \tag{6.16}$$

The SIMO strategy can be used to obtain the compensators K_v and K_m, simultaneously. In this methodology, the dual-stage tracking error in Eq. (6.10) is minimized, while satisfying H_∞ and H_2 constraints for both the VCM single-stage loop in Fig 6.2 and the dual-stage loop in Fig. 6.1. Therefore, the obtained controller is not necessarily minimizing the single-stage VCM loop tracking error in Eq. (6.11). The optimization problem for the SIMO methodology that will be solved to synthesize the compensator $\bar{K}$ in Eq. (6.1) is

$$\begin{aligned}
\text{minimize} \quad & \frac{1}{l} \sum_{i=1}^{l} \|e_i\|_2^2 \text{ defined in Eq.}(6.10) \\
\text{subject to} \quad & \text{Eqs. } (6.4), \ (6.5), \ (6.8), \ (6.9), \\
& \text{Eqs. } (6.12), \ (6.13), \ (6.14).
\end{aligned} \tag{6.17}$$

After obtaining $\bar{K}$, the compensators K_v and K_m are obtained from Eqs. (6.2) and (6.3).

6.4 Control Design Results

Design Settings

In this section, the data driven mixed H_2/H_∞ control design methodology will be used to design a track following controller for a dual-stage HDD. As previously stated, the data-driven design methodology only uses frequency response measurements of the plant, without requiring models of the actuators. Here, five sets of frequency response data are used to represent dynamics variations for each actuator. Hence, $l = 5$ in Eqs. (6.4)-(6.17). These five sets of frequency response data are plotted in Fig. 6.3. If a higher number of frequency response data is required to represent system dynamics, those measurements can be easily included in the design process. A linear frequency grid with 200 points will be used to span the operating frequency region Ω, between 10-19,000 Hz. This frequency grid will be employed throughout this chapter to characterize the open loop and closed loop transfer functions, and synthesize all the compensators.

The frequency response plots shown in Fig. 6.3 were generated using realistic models of both the VCM and the MA. The data-driven design methodology presented in this dissertation was also used with real frequency response data provided by our HDD industrial research partners. However, this data is considered confidential and proprietary by our partners and cannot be presented here. Therefore, the frequency response data plotted in Fig. 6.3 were produced to mimic real measurements. We emphasize that, although actual transfer functions $G_{vi}(z)$ and $G_{mi}(z)$ were constructed to respectively characterize dynamics variations in the VCM and MA, only the frequency response data generated by these transfer functions, in the form of factorizations $N_{vi}(\omega)$, $M_{vi}(\omega)$ and $N_{mi}(\omega)$, $M_{mi}(\omega)$, were used in the control synthesis algorithms, where i denotes the ith frequency response data set.

Noise Spectrum

The noise spectrums considered for the H_2 norm computations in Eqs. (6.10)-(6.14) are shown in Fig. 6.4 for the run-out R and measurement noise N. The spectrums are denoted with the upper-case letters of the corresponding noises. These spectrums data will be used directly in the design process without any model fitting. According to our HDD industrial research partners, the spectrum for the control input noises can be set to zero, $W_v = 0$ and $W_m = 0$, since the spectrums given in Fig. 6.4 are obtained by assuming that the effects of control input noises are lumped into the run-out R and measurement noise N spectrums. Although the spectrum for the control input noises are set to zero, the closed loop transfer functions from control input noises to control inputs and error signals are considered in the design as H_∞ constraints.

H_∞ Constraints

The H_∞ constraints used in the optimization problems are weighted using numerically shaped bounded weighting functions over the frequency regions. As mentioned in section 5.2, the
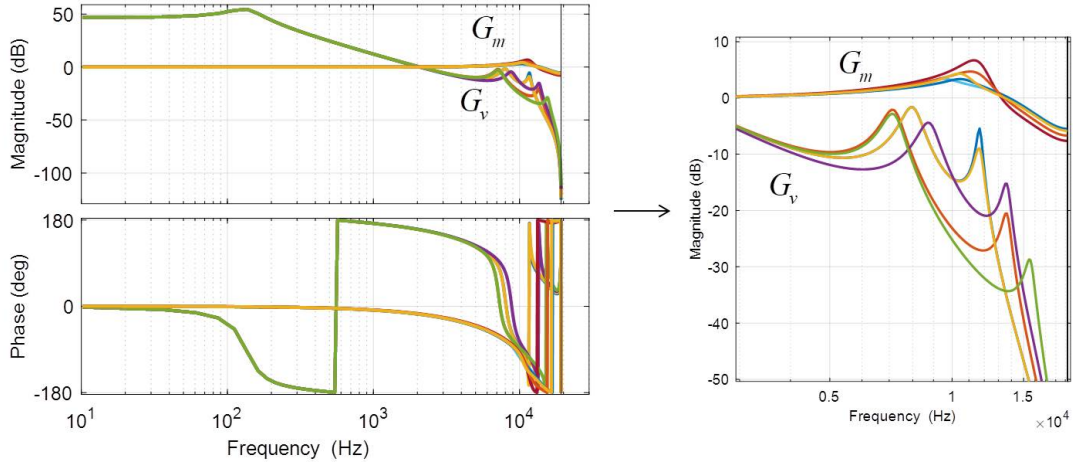
Figure 6.3: Hard disk drive actuators frequency response measurement data sets used in the design. Five measurements from each actuator is used in the design. G_v and G_m represent VCM and MA actuators' transfer functions, respectively. The actuators output units for both the VCM and the MA are 10 nm.
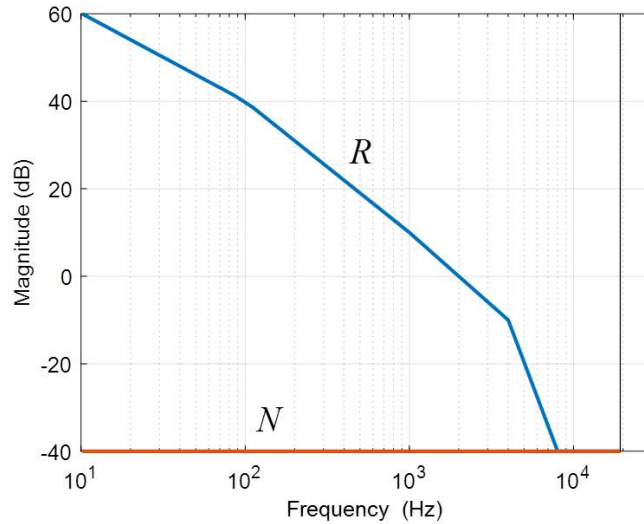
Figure 6.4: The magnitude Bode plots of the estimated spectrums of external noises applied on the hard disk drive. R and N respectively represent the spectrums for the run-out r and the measurement noise n. The units for both external noises are 10 nm.

SISO transfer functions are shaped using the inverse of these weighting functions. Moreover, the maximum singular values of the MIMO transfer functions are shaped using the inverse of the minimum singular values of these weighting functions. These shaping functions are shown with light blue dotted lines in appendix B and are called the H_∞ constraint limits. The scalar γ used in all H_∞ constraints is chosen to be 1.

H_2 Constraints

The H_2 constraints in Eqs. (6.12), (6.13) and (6.14) are used to constraint the average variances of the VCM input and the MA output stroke in the time domain for the set of $l = 5$ frequency response data sets. As mentioned in section 5.3, the worst case H_2 can be also used to constraint the maximum variance among the l frequency response data sets. Assume that the maximum allowable amplitude of a zero mean Gaussian random signal in the time domain is X. The standard practice in the magnetic recording industry is to constrain the 3σ value of the signal to be within X, in order to assure with a 99.7% probability that the random signal will remain within X, assuming that the signal is Gaussian. The maximum allowable VCM control input is usually $5\ Volts$, therefore its standard deviation and variance should be limited to be smaller than $5/3\ Volts$ and $(5/3)^2\ Volts^2$, respectively. Since the actuator models and noise spectrums given in Figs. 6.3 and 6.4 are only an approximation of the real system, therefore the upper-limits for the average variances of the VCM control input both in the VCM single-stage and dual-stage loops are rounded up to be

$$\eta_{u_v^s} = 2.0^2\ Volts^2,\ \eta_{u_v} = 2.0^2\ Volts^2, \tag{6.18}$$

respectively.

The MAs used in HDDs have limited output strokes. A MA with a smaller output stroke is generally cheaper to fabricate, more reliable and has higher resonance mode frequencies than MAs with larger strokes. On the other hand, decreasing the MA stroke can affect the performance of the servo system. In order to study the effect of the MA output stroke on the overall HDD track following servo performance, four different values for the average variance upper-limit of the MA output stroke are considered here

$$\eta_{y_m} = 44^2,\ 42^2,\ 40^2,\ 38^2\ nm^2. \tag{6.19}$$

Controller Structure

The sensitivity decoupling controller structure given in Fig. 6.1 is used for the dual-stage HDD control design. The estimated model of the MA plant used in the controller structure is considered to be a pure delay

$$\hat{G}_m = \frac{1}{z}. \tag{6.20}$$

Moreover, an integrator of the form $\frac{z}{1-z}$ is incorporated into the VCM controller, in order to eliminate the steady state tracking error due to DC disturbances. As mentioned in

section 6.1, the compensators K_v and K_m can be obtained using either the sequential SISO or SIMO design strategies. In the sequential SISO design strategy, these compensators are obtained in two consecutive steps, while in the SIMO design strategy, K_v and K_m are obtained simultaneously.

Stable Factorizations

The stable factorizations of a SIMO controller with an integrator included in the first element of the controller was derived in Eqs. (5.20) and (5.21). In these equations, the value of the parameter m is 2, since the SIMO controller for the dual-stage HDD has two outputs. The controller order parameter, n, will be selected to be 25.

In the sequential SISO design strategy, first the compensator K_v is obtained using the VCM single-stage loop in Fig. 6.2. Then, the compensator K_m is obtained using the dual-stage loop in Fig. 6.1 by fixing the compensator K_v. The first SISO design step for obtaining the compensator K_v uses the controller stable factorizations in Eqs.(5.20) and (5.21), which consider an integrator in the controller structure. Since this is a SISO loop, $m = 1$ is chosen. The compensator K_m uses stable factorizations given in Eqs. (5.11) and (5.12) with $m = 1$. The compensator order parameters, n, for K_v and K_m will be chosen to be 16 and 20, respectively. The reasoning behind choosing these values for the compensator order parameters are provided later in this section in the explanation of Fig. 6.11.

The actuators in the HDD are stable actuators. Therefore, the initial stable factorizations of the actuators frequency response measurements are obtained using Eqs. (5.3) and (5.4). As mentioned in the mixed H_2/H_∞ flowchart in Fig. 5.2, these stable factorizations will be normalized at the end of each iteration using Eq. (5.76).

Design Scenarios

Once the stable factorizations for the actuators and controllers are defined, the convex optimization problems mentioned in section 6.3 are formulated and solved. The sequential SISO controller design strategy solves the optimization problems formulated in Eqs. (6.15) and (6.16) for the compensators K_v and K_m, respectively. The SIMO controller $\bar{K}$ in Eq. (6.1) is obtained by solving Eq. (6.17). These convex optimization problems are formulated using the YALMIP toolbox[48] in MATLAB software package[50]. The formulated optimization problems are solved using the MOSEK solver[8]. This solver is capable of handling both linear and quadratic programs, where the constraints in the optimization problem are formulated as Linear Matrix Inequalities (LMIs).

The compensators in the sensitivity decoupling structure given in Fig. 6.1 were designed under four different scenarios each involving a different value of η_{y_m}, the upper-limit of the MA output stroke average variance. These values are given in Eq. (6.19) and also shown in Table 6.1. Since the compensators obtained using the sequential SISO design strategy always satisfied these four constraints, only the scenario involving the value of $\eta_{y_m} = 44 \ nm$ will be discussed for the sequential SISO design strategy. Table 6.1 presents the five cases

of controller design scenarios that will be evaluated and compared with each other in this section, as well as their respective color code used in the plots.

Table 6.1: Controller design scenarios and their color code.

Scenarios	$SIMO_1$	$SIMO_2$	$SIMO_3$	$SIMO_4$	$SISO_1$
Design strategies	SIMO	SIMO	SIMO	SIMO	sequential SISO
η_{y_m} (nm^2)	44^2	42^2	40^2	38^2	44^2
Color code					

The design approach proposed in chapter 5 is an iterative approach. In the results presented in this section, the controllers were designed using 10 iterations. The 10th iteration is used as the stopping criterion for the algorithm in order to have the same number of iterations for all the design scenarios in table 6.1. However, a more sophisticated stopping criterion, which take into account the rate of optimization objective reduction as a function of the iteration number can be implemented [15]. As shown in the flowchart given in Fig. 5.2, the first iteration only considers the H_∞ constraints. The second iteration also includes the H_2 objective. Finally starting from the third iteration, the full optimization problem including H_2 objective, and all H_2 and H_∞ constraints are considered.

Design Results

In this section, the synthesized dual-stage HDD compensators obtained by solving the control objectives in section 6.2 are discussed. First, the design results for the data-driven mixed H_2/H_∞ control methodology are discussed considering all the design scenarios in Table 6.1 using all the plant frequency response data sets in Fig. 6.3. The plots used to represent these design results utilize the color code in table 6.1 to distinguish between different scenarios. However, the plots for the same scenario but different frequency response data sets utilize the same color code and may not be distinguishable from each other at some frequency regions, where the plots are relatively close to each other. Subsequently, an example to describe a limitation of the sequential SISO design strategy as compared to the SIMO design strategy is provided. Last but not the least, the design results for the mixed H_2/H_∞ control problem, when theorem 5.3.1 is utilized to impose the H_∞ norm constraints, are compared with the corresponding results obtained when theorem 5.3.2 is used instead of theorem 5.3.1. Theorem 5.3.2 utilizes sufficient conditions for imposing the H_∞ norm constraints, while theorem 5.3.1 utilizes necessary and sufficient conditions.

Design Scenarios Comparison

The closed loop transfer functions in the final, 10th iteration, and their H_∞ constraint limits for the VCM single-stage and dual-stage loops are shown in appendix B. As shown in the figures, all the closed loop transfer functions satisfy the H_∞ constraints given in Eqs. (6.4),

(a) $\sqrt{\frac{1}{l}\sum_{i=1}^{l}\|e_i^s\|_2}$

(b) $\sqrt{\frac{1}{l}\sum_{i=1}^{l}\|u_{vi}^s\|_2}$
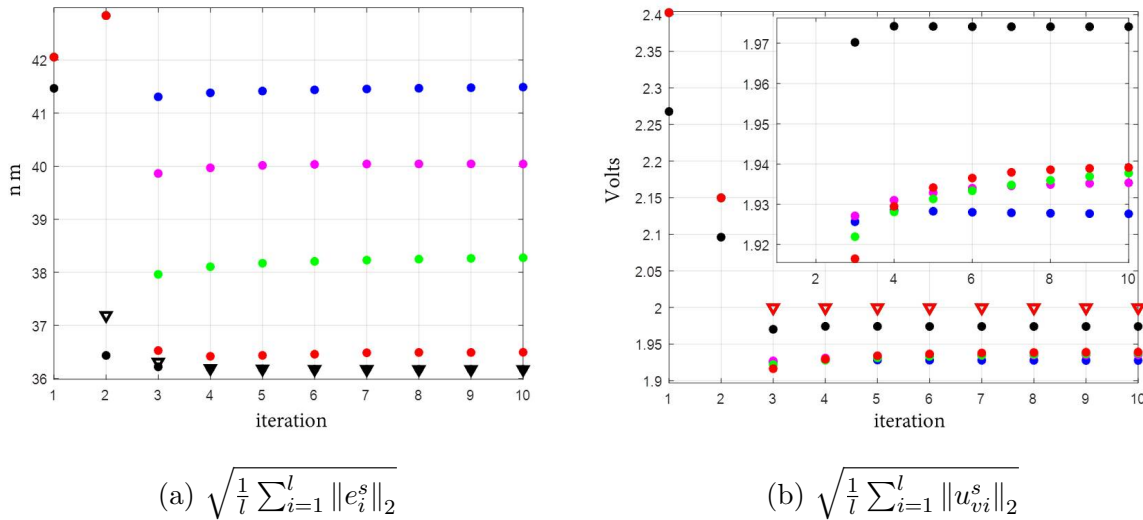
Figure 6.5: The H_2 norm objective and constraints, for the VCM single-stage loop depicted in Fig. 6.2 over the iterations. The average variances of signals are considered in the optimization problems, however the square roots of the average variances are plotted here. The triangles show the upper-bound for the square root of the average variance for the tracking error (a) and the VCM control action (b), where the circles show the real values for these variables. The H_2 norm objective and constraints are activated starting from the second and third iterations, respectively.

(6.5), (6.8) and (6.9). The weighting functions used in these equations will shape the closed loop transfer functions. These weighting functions can be numerically shaped, since the data-driven control design methodology is utilized.

The H_2 norm objective and constraints, for the VCM single-stage loop depicted in Fig. 6.2 are shown in Fig. 6.5, considering all the scenarios mentioned in table 6.1. In the sequential SISO design strategy, the objective is to minimize the average variance of the VCM single-stage tracking error, while designing the VCM controller. However, the objective in the SIMO design strategy is to minimize the average variance of the dual-stage tracking error, without explicitly considering the average variance of the single-stage tracking error as an optimization objective. Therefore, as one can notice in Fig. 6.5a, the sequential SISO design strategy achieves the smallest average variance for the VCM single-stage tracking error, as compared to the SIMO designs. Moreover, Fig. 6.5b shows that the VCM controller designed using the sequential SISO strategy has the highest activity in terms of the VCM control input average variance.

The MA output stroke is restricted by defining an upper-bound on its average variance in Eq. (6.14). Reducing the value of this upper-bound will reduce the MA range and consecutively reduce the MA's ability to minimize the tracking error. In this case, the sensitivity decoupling structure suggests that the VCM should compensate for the MA by achieving

a smaller average variance of the VCM single-stage tracking error. According to Figs. 6.5a and 6.5b, if the MA output stroke is reduced, the VCM single-stage loop achieves a smaller average variance of the tracking error at the cost of having increased average variance of the VCM control input.

As shown in Fig. 6.5a, the controller designed using the sequential SISO design strategy is the most aggressive one in terms of minimizing the average variance of the VCM single-stage tracking error. Also, the SIMO controllers with the more stringent restriction on the MA output stroke will be more aggressive based on this definition. The VCM single-stage sensitivity plots for all these scenarios are shown in Fig. 6.6. In the frequency region between $0 - 500 \ Hz$, where the VCM is the dominant actuator, all these scenarios achieve almost the same level of the VCM single-stage tracking error reduction. However in the frequency region between $500 - 2000 \ Hz$, where both actuators are active, the more aggressive VCM single-stage controller will improve the VCM single-stage tracking error reduction, in order to compensate for the MA output stroke restriction.

Since the z-domain transfer functions for all of the actuators frequency response measurements shown in Fig. 6.3 are available for this example, we were able to compute the closed loop poles of the feedback system, for all of the synthesized compensators and for all of the scenarios in table 6.1, and to verify that all of the compensators designed yield stable feedback systems for all of the plants. The stability margins and bandwidths for all these scenarios are obtained in the frequency domain using the plant frequency response data sets shown in Fig. 6.3. The worst case stability margins and bandwidths are defined in Eqs. (6.21)-(6.25) and are shown in table 6.2 for all of the scenarios in table 6.1.

$$\text{worst}(E^s_{r \to e}\text{peak}) = \max_i E^s_{(r \to e)i}\text{peak} \tag{6.21}$$

$$\text{worst}(GM) = \min_i GM_i \tag{6.22}$$

$$\text{worst}(PM) = \min_i PM_i \tag{6.23}$$

$$\text{worst}(\omega_{GM}) = \min_i \omega_{GM_i} \tag{6.24}$$

$$\text{worst}(\omega_{PM}) = \min_i \omega_{PM_i} \tag{6.25}$$

where the subscript i denotes the ith frequency response data sets. The more aggressive controller generally increases the worst case bandwidth, worst(ω_{PM}), at the cost of having lower stability margins. However, this trend is not completely followed, since the aggressiveness of the controllers is defined in terms of the H_2 norm of the closed loop transfer functions, which restricts the integration of the frequency response magnitude over the entire frequency region. Therefore, increasing the restriction on the H_2 norm does not always directly affect the bandwidth and stability margins of the open loop transfer function.

The H_2 norm constraints for the VCM input and the MA output stroke in the dual-stage HDD are shown in Figs. 6.7a and 6.7b, respectively. In the sequential SISO design strategy, the VCM is designed to be aggressive. As a result, the average variance of the VCM control input in both the VCM single-stage and dual-stage loops for the sequential SISO design

Table 6.2: Open loop worst case stability margins for the VCM single-stage loop in Fig. 6.2. These margins are obtained by selecting the worst case margins among all frequency response data sets using Eqs. (6.21)-(6.25).

Scenarios	Worst case	$E^s_{r \to e}$ peak dB	GM dB	PM $degree$	ω_{GM} Hz	ω_{PM} Hz
$SIMO_1$		9.97	3.45	25.83	2,206	1,242
$SIMO_2$		10.01	3.30	28.55	2,319	1,230
$SIMO_3$		10.17	3.22	31.17	2,427	1,244
$SIMO_4$		10.03	3.28	32.46	2,548	1,276
$SISO_1$		10.10	3.28	31.45	2,493	1,344
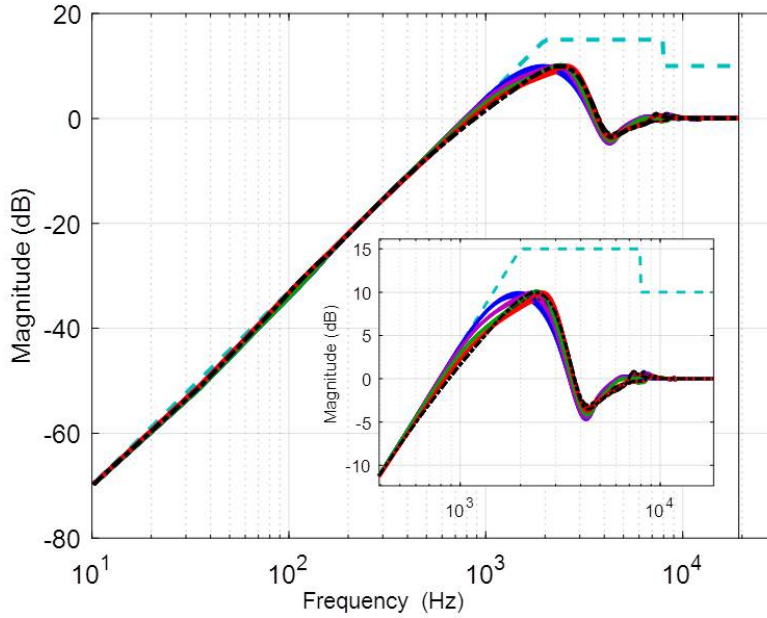
Figure 6.6: The magnitude Bode plots of the VCM single-stage sensitivity transfer function, $E^s_{r \to e}$. These plots include 25 closed loop transfer functions for all the 5 design scenarios in table 6.1 using all the 5 frequency response data sets in Fig. 6.3.

strategy will be higher compared to all the scenarios in the SIMO design strategy, as shown in Figs. 6.5b and 6.7a. As previously mentioned, using a MA with a smaller output stroke will result in a corresponding increase in the average variance of the VCM control input in the VCM single-stage loop, in order to compensate for the MA output stroke reduction. However, the MA with a smaller output stroke decreases the average variance of the VCM control input in the dual-stage loop. This can be justified by the fact that the the smaller MA output stroke requires less VCM movements to compensate for the MA output movements,

(a) $\sqrt{\frac{1}{l} \sum_{i=1}^{l} \|u_{vi}\|_2}$

(b) $\sqrt{\frac{1}{l} \sum_{i=1}^{l} \|y_{mi}\|_2}$
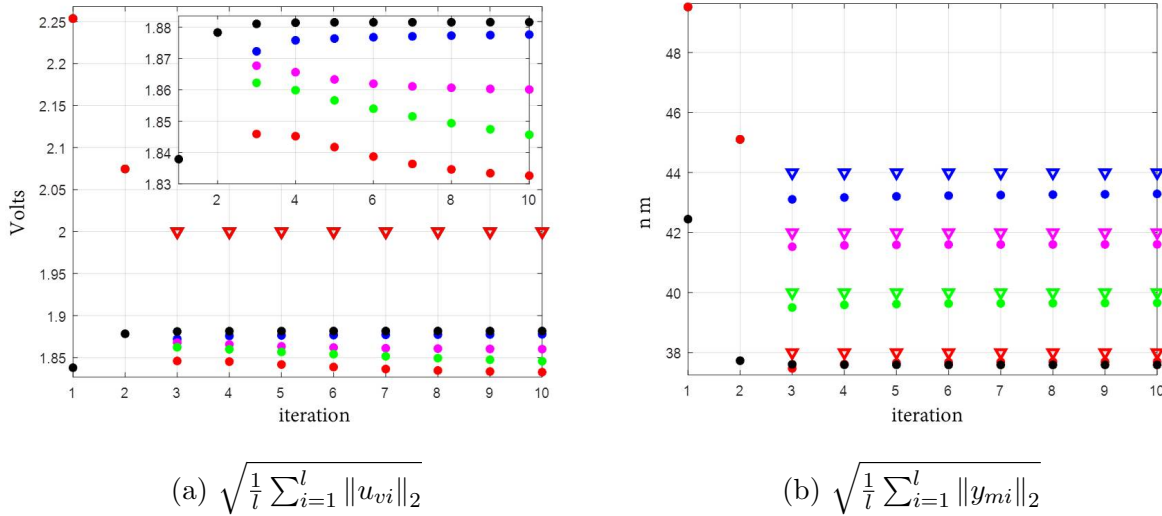
Figure 6.7: The H_2 norm constraints for the dual-stage loop over the iterations. The average variances of signals are considered in the optimization problems, however the square roots of the average variances are plotted here. The triangles show the upper-bound for the square root of the average variance for the VCM control action (a) and the MA output stroke (b), where the circles show the real value for these variables. The H_2 norm objective and constraints are activated starting from second and third iterations, respectively.

which are out of phase with the VCM output movements. Fig. 6.7b demonstrates that all the controller design scenarios considered in table 6.1 are satisfying their upper-bound constraints for the average variance of the MA output stroke.

Fig. 6.8 plots the square root of the average variance of the tracking error for the dual-stage feedback system in Fig. 6.1. According to Eqs. (6.16) and (6.17), the average variance is considered as the minimization objective in the SIMO design strategy as well as the second step of the sequential SISO design strategy. In the sequential SISO design strategy, the obtained VCM compensator K_v, which is synthesized to optimize the average variance of the VCM single-stage tracking error, is kept fixed during the synthesis of the MA compensator K_m. This results in a suboptimal overall compensator in terms of minimizing the average variance of the dual-stage tracking error, since the compensator K_v design process in the sequential SISO design strategy does not take into account the dual-stage loop. This is verified in Fig. 6.8, which shows that the sequential SISO design strategy achieves a relatively higher average variance of the dual-stage tracking error compared to all the scenarios in the SIMO design strategy.

The results in Fig. 6.8 also suggest that the average variance of the dual-stage tracking error in the SIMO design strategy is a non-linear function of the restriction on the average variance of the MA output stroke. If the average variance upper-bound on the MA output stroke given in Eq. (6.19) is 42 nm or greater, the average variance of the dual-stage tracking
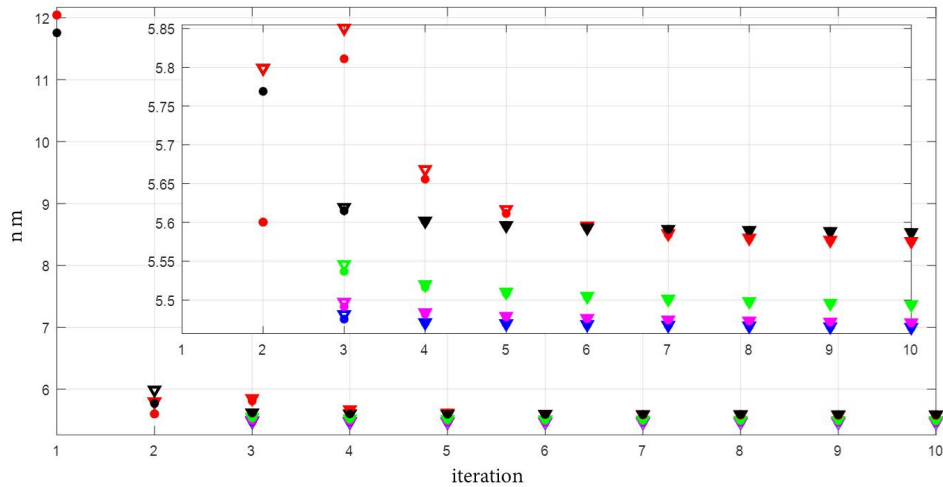
Figure 6.8: $\sqrt{\frac{1}{l}\sum_{i=1}^{l}\|e_i\|_2^2}$ for the SIMO feedback system in Fig. 6.1 as a function of control synthesis iterations: The average variances of signals are considered in the optimization problems, however the square roots of the average variances are plotted here. The H_2 norm objective and constraints are activated starting from second and third iterations, respectively.

error will not change significantly. The main reason to this phenomenon is that, according to Fig. 6.5a, the VCM is able to compensate for this MA output stroke restriction. However, the VCM's ability to compensate for the MA output stroke restriction is limited. If the average variance upper-bound on the MA output stroke is smaller than 42^2 nm, the decrease in this upper-bound will increase the average variance of the dual-stage tracking error at a higher rate as compared to the case of the MA output stroke with the average variance upper-bound of 42^2 nm or greater.

Similar to the VCM single-stage loop, the closed loop poles for all the scenarios in table 6.1 were computed using the z-domain transfer functions of the actuator frequency response measurements. All these closed loop poles were confirmed to be located inside the unit circle. Therefore, all the closed loop transfer functions were stable for all the plants used to generate the frequency response data in the data-driven mixed H_2/H_∞ formulation. Table 6.3 presents the dual-stage open loop stability margins and bandwidths for these design scenarios. These stability margins and bandwidths are reported as the worst case margins and bandwidths using Eqs. (6.21)-(6.25). In this table, the open loop transfer function is from the track run-out r to the position head output y in Fig. 6.1. As shown in Fig. 6.1, the imposition of a more stringent restriction on the MA output stroke, which is achieved by reducing the upper-bound on the average variance of this signal, will result in a lower dual-stage bandwidth. This reduction in the bandwidth will help to improve the stability margins. The dual-stage controller designed using the sequential SISO design strategy will have a relatively lower bandwidth and a higher peak for the sensitivity plot as compared to the $SIMO_4$ case. The

higher sensitivity plot peak for the sequential SISO design strategy can be justified by the fact that this strategy will design compensators k_v and k_m in two individual steps and the compensator K_v is designed without considering the dual-stage actuation structure.

Table 6.3: Open loop worst case stability margins for the dual-stage loop in Fig. 6.1. The open loop transfer function is from the track run-out r to the position head output y. These margins are obtained by selecting the worst case margins among all frequency response data sets using Eqs. (6.21)-(6.25).

Scenarios	Worst case $E_{r \to e}^s$ peak dB	GM dB	PM $degree$	ω_{GM} Hz	ω_{PM} Hz
$SIMO_1$	9.63	8.85	19.13	12,392	4,924
$SIMO_2$	9.62	8.85	19.14	12,393	4,922
$SIMO_3$	9.55	8.86	19.36	12,390	4,914
$SIMO_4$	9.43	8.87	19.74	12,401	4,884
$SISO_1$	9.58	8.90	19.23	12,377	4,857

Fig. 6.9b plots the frequency responses of the closed loop transfer functions from the track run-out r to the actuator outputs y_v and y_m. As shown in the figure, the VCM is more active at the low frequency region, while the MA takes over at the mid-frequency region. At the high frequency region, the output of both actuators will reduce, since the system can not be controlled due to the dynamics uncertainty of the actuators.

According to Fig. 6.4, the run-out r is the dominant external noise and its magnitude has an inverse relationship with frequency. Therefore, a more stringent restriction on the average variance of the MA output stroke defined in Eq. (6.14) will force the MA output to be more active at higher frequency regions, where the magnitude of run-out is smaller. As shown in Fig. 6.9b, a controller designed with a more restricted MA output stroke criteria will produce a smaller MA output magnitude in frequencies between $500 - 2000\ Hz$ and a higher MA output magnitude in frequencies between $2000 - 3000\ Hz$. According to Fig. 6.9a, the smaller magnitude of the MA output in lower frequency regions also deteriorates the tracking error rejection in those regions. At higher frequency regions, the larger magnitude of the MA output helps to improve the tracking error rejection.

The frequency responses of the obtained compensators K_v and K_m are plotted in Fig. 6.10 for all the scenarios in table 6.1. The SIMO design strategy uses the stable factorizations of the controller in Eqs. (5.20) and (5.21) with the controller order parameter $n = 25$ in order to obtain the SIMO controller. After designing the SIMO controller, the compensators K_v and K_m are derived using Eqs. (6.2) and (6.3). The Hankel singular values [7] of these compensators are plotted in Fig. 6.11. In order to reduce the compensators orders, a few of the Hankel singular values with the smallest magnitudes were eliminated. The gray boxes in Fig. 6.11 show the eliminated Hankel singular values. The reduced order compensators K_v and K_m will be 17th and 20th orders, respectively. The comparisons between the reduced

(a) $E_{r \to e}$

(b) $Y_{r \to y_v, y_m}$
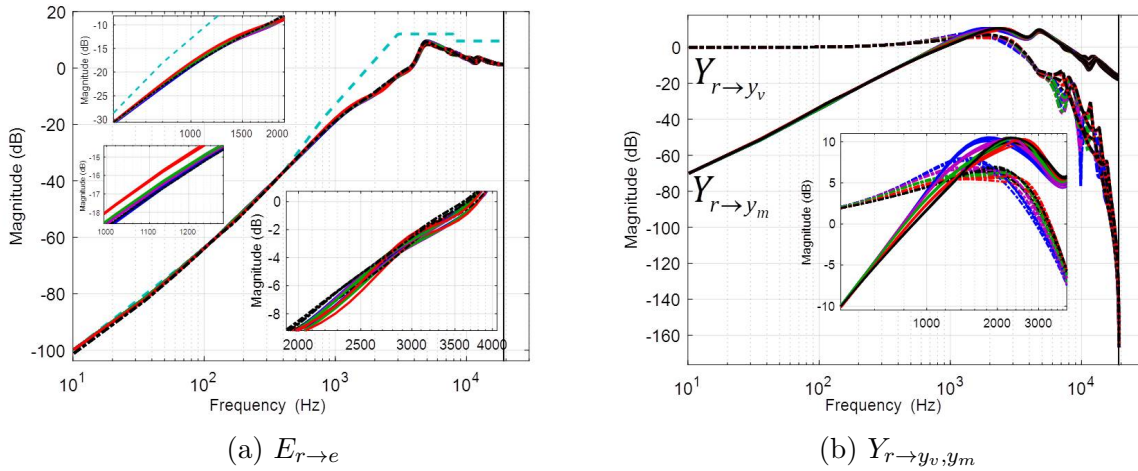
Figure 6.9: The magnitude Bode plots of the closed loop transfer functions for the dual-stage loop. These plots include 25 closed loop transfer functions for all the 5 design scenarios in table 6.1 using all the 5 frequency response data sets in Fig. 6.3.

order and the full order compensators are provided in Fig. 6.11. As shown in the figures, the compensator order reduction will not create any significant difference in the low and mid frequency regions of the compensators frequency responses. In high frequency regions, the deviation between the reduced order and the full order VCM compensator K_v will not significantly affect the closed loop transfer functions, since according to Fig. 6.3, the VCM response has relatively small magnitude at high frequency regions. Moreover, the effect of MA compensator order reduction at high frequency regions is negligible. Therefore, the orders for the compensators K_v and K_m in the sequential SISO design strategy can be reduced to 17th and 25th orders respectively, which are equal to the orders of the corresponding reduced order compensators in the SIMO design strategy.

A limitation of the Sequential SISO Design Strategy

It is worth mentioning that if the SIMO design strategy is successful to find a feasible solution for the optimization problem in Eq. (6.17), there is no guarantee that the sequential SISO design strategy can also find a feasible solution for the optimization problem in Eq. (6.16) by considering the same set of control objectives. As an example, the weighting function used in the H_∞ norm of the closed loop transfer function $U_{w_v \to u_m}$ was adjusted to force more restrictions at high frequency regions for the scenarios $SISO_1$ and $SIMO_1$ in table 6.1. In Fig. 6.12, the less stringent H_∞ constraint limit is shown with light blue dotted lines, while the more stringent H_∞ constraint limit is shown with red dotted lines. The SIMO design strategy is able to synthesize a controller that can satisfy the more stringent constraint. However, the sequential SISO design strategy is not able to find a feasible solution to satisfy this constraint. This result can be partially explained by considering the fact that, in the sequential SISO design strategy the compensator K_v is first synthesized without considering
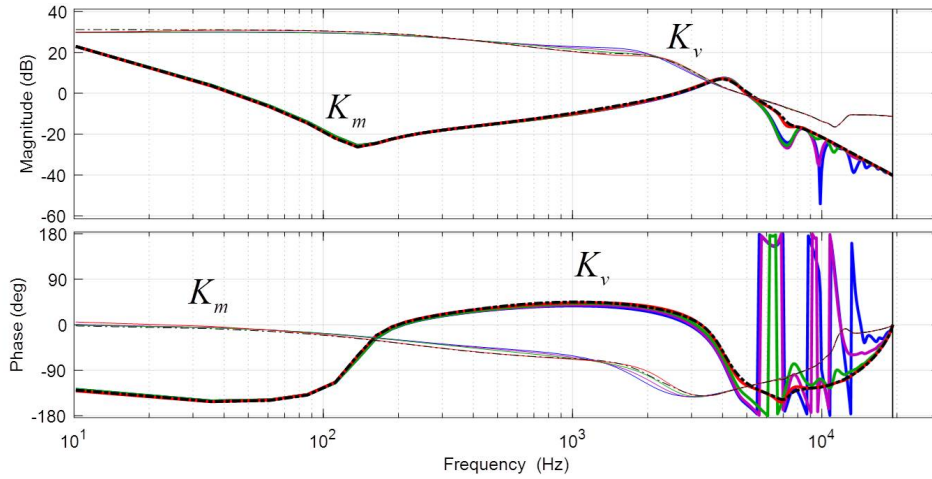
Figure 6.10: Frequency responses of the compensators K_v and K_m for all the 5 design scenarios in table 6.1 synthesized considering all the 5 plant frequency response data sets plotted in Fig. 6.3. The frequency responses of the compensator K_v are plotted with thick lines, while the frequency responses of the compensator K_m are plotted with thin lines.

(a) K_v

(b) K_m
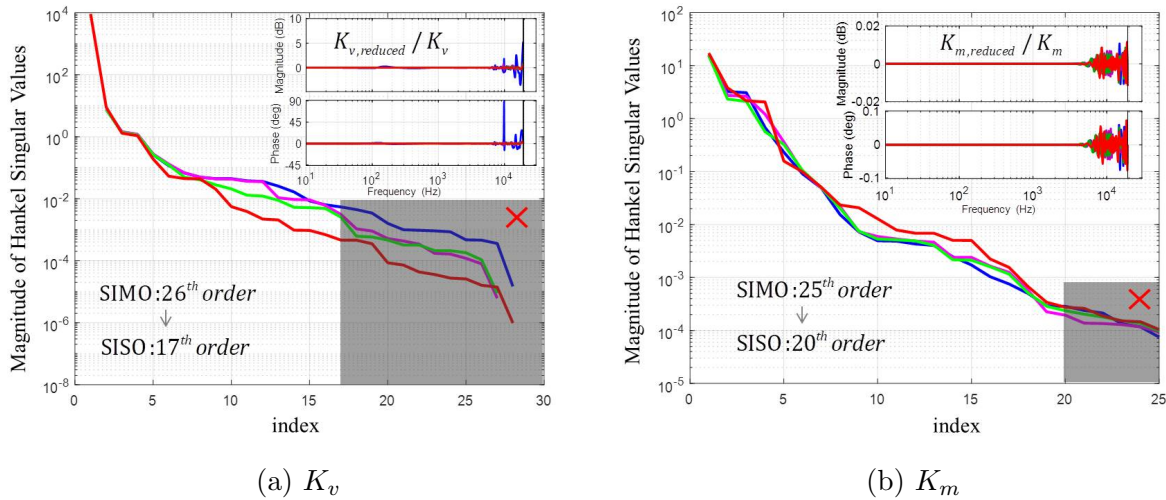
Figure 6.11: The Hankel singular values for both the K_v and K_m compensators for the design scenarios $SIMO_1$-$SIMO_4$ in table 6.1. The gray boxes show the singular values which were eliminated in the compensator order reduction. The comparisons between the reduced order and the full order compensators are also provided in these plots.
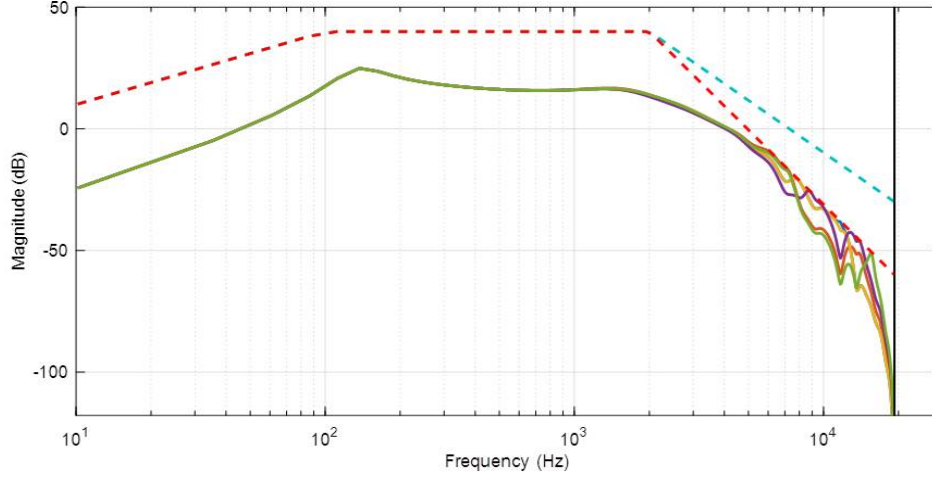
Figure 6.12: The magnitude Bode plots of the closed loop transfer function from control input disturbance w_v to MA control input u_m, $U_{w_v \to u_m}$. The solid lines show the magnitude Bode plots of the closed loop transfer function $U_{w_v \to u_m}$ for the design scenario $SIMO_1$ in table 6.1 considering all the 5 plant frequency response data sets in Fig. 6.3. The red dotted lines represent the more stingest H_∞ constraint limit, while the light blue dotted lines represent the less stingest H_∞ constraint limit used in this section. The SIMO design strategy obtains the controller such that $U_{w_v \to u_m}$ transfer functions satisfy the more stingest H_∞ constraint limit, while the sequential SISO design strategy cannot find a feasible solution for this H_∞ constraint limit.

the overall dual-stage loop constraints, and in addition, the compensator K_m is subsequently synthesized without the added flexibility of changing the compensator K_v.

Design Results Comparison Using Two Different Conditions for Imposing H_∞ Constraints

The results presented in this section, were obtained using theorem 5.3.1 to prescribe necessary and sufficient convex conditions for imposing the H_∞ constraints considered in the mixed H_2/H_∞ optimization problems given in Eqs. (6.15)-(6.17). As mentioned in section 5.3, sufficient convex conditions for imposing the H_∞ constraints were proposed in [41]. These two types of convex conditions for imposing the H_∞ constraints can be summarized as

- I) necessary and sufficient convex conditions given in theorem 5.3.1,

- II) sufficient convex conditions given in theorem 5.3.2.

The H_∞ sufficient convex conditions in theorem 5.3.2 can be applied to the synthesis of general MIMO compensators, while the H_∞ necessary and sufficient convex conditions in theorem 5.3.1 is only applied to the synthesis of SIMO compensators.
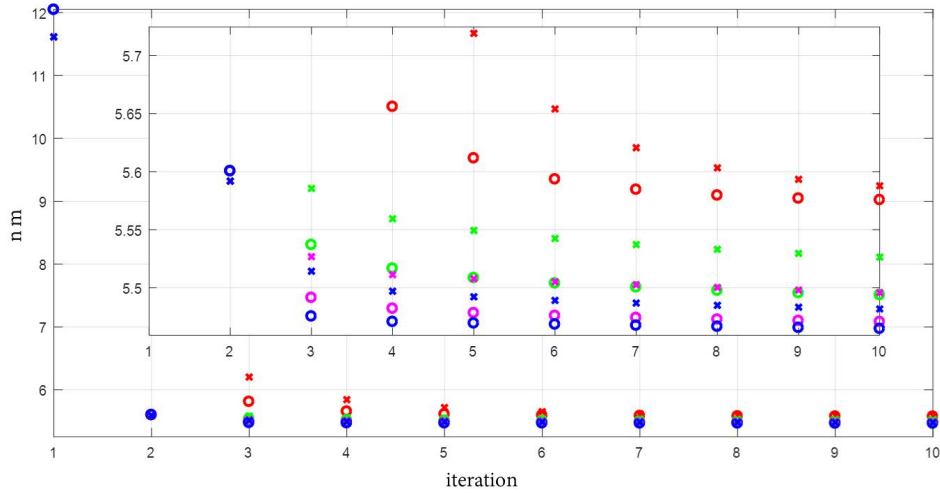
Figure 6.13: $\sqrt{\frac{1}{l}\sum_{i=1}^{l}\|e_i\|_2^2}$ for the SIMO feedback system in Fig. 6.1 as a function of control synthesis iterations, considering the design scenarios $SIMO_1$-$SIMO_4$ in table 6.1: The average variances of the dual-stage tracking error signal are considered in the optimization problems, however the square roots of the average variances are plotted here. The circle ($\circ$) and cross ($\times$) marks respectively represent conditions I and II as the convex conditions for imposing the H_∞ constraints used in Eq. (6.17). The H_2 norm objective and constraints are considered in the optimization problem starting from the second and third iterations, respectively.

In order to compare these two convex conditions for imposing the H_∞ constraints, the SIMO dual-stage controller in Fig. 6.1 that was synthesizes by solving the mixed H_2/H_∞ control design problem given in Eq. (6.17), for all the scenarios in table 6.1 using the SIMO design strategy were redesigned using the sufficient convex conditions II instead of using the necessary and sufficient convex condition I, and its performance was compared to the compensator previously designed using condition I. All the designed compensators were able to satisfy the H_∞ and H_2 norm constraints. The resulting H_2 norm objectives for these two conditions are compared in Fig. 6.13, where the circle ($\circ$) and cross ($\times$) marks respectively represent conditions I and II as the convex conditions for imposing the H_∞ constraints. As shown in the figure, a controller designed utilizing the sufficient H_∞ conditions II will produce a larger cost when compared with the cost produced by a controller designed using the necessary and sufficient H_∞ conditions I under the same design scenariosg and the same plant data sets. The degraded performance for condition II can be justified by the fact that having only sufficient conditions for imposing the H_∞ constraints introduces conservatism in the optimization problem and leads to an increase in the minimization objective as compared to the necessary and sufficient conditions.

Chapter 7

Conclusion and Future Work

7.1   Conclusion

This dissertation discussed three control design methodologies for hard disk drives servo systems, in order to improve their performance as well as their reliability. The first was a state estimator for non-uniform sampled systems with irregularities in the measurement sampling time, which estimated the states at a uniform sampling time. The second was an online uncertainty identification algorithm, which parametrized and identified the uncertain part of transfer functions in a dual-stage HDD. The third was a frequency based data-driven control design methodology, which considered mixed H_2/H_∞ control objectives and was able to synthesize track following servo systems for dual stage actuators utilizing only the frequency response measurement data, without the need of identifying the models of the actuators.

In chapter 1, an introduction as well as a brief literature review for the control problems in hard disk drives were provided first. Then, the contributions for each chapter of this dissertation were summarized. Last but not the least, the notations used throughout this dissertations were introduced in this chapter.

In chapter 2, a general overview of the dual-stage HDD structure and mechanisms were provided. The servo assembly of the dual-stage Hard Disk Drive (HDD) is composed of the Voice Coil Motor (VCM) and the Mili-Actuator (MA), where the VCM is responsible for coarse positioning at low frequency regions and the MA is responsible for fine positioning at high frequency regions. Controlling these two actuators is very critical in precision positioning of the read/write head, which is mounted at the edge of the servo assembly.

In chapter 3, the observer design problem for systems with uniform sampled control inputs and non-uniform sampled measurements was considered. In the spiral writing procedure in the self-servo writing process, the head position measurements are arriving at non-uniform sampling times, while the control inputs are updating at uniform sampling times. The variations in measurement sampling times were modeled as variations in the plant model dynamics. The gain-scheduling technique accommodated these variations in the design stage

and obtained a varying observer which could estimate system states at the uniform sampling times. The gain-scheduling observer were designed using the Kalman filter structure and its performance was evaluated by comparing it with the Kalman filter [40].

Kalman filter is the optimal observer in terms of minimizing the trace of a-posteriori state estimation error covariance, given the values of noise variances. Therefore, if noise variances were known in advance, the Kalman filter would achieve the best performance. However, the exact values of noise variances may not be known in real systems. The simulation results showed that if the upper-bound of the noise variances were known, the gain-scheduling observer could outperform the Kalman filter. The main reason behind this observation is that the Kalman filter was designed for the exact given values of noise variances, while the gain-scheduling observer was designed for noise variances of equal or smaller than the designed values.

It is worth mentioning that one of the main advantages of the gain-scheduling observer is its less online computational complexity as compared to the Kalman filter. The gain-scheduling observer gain can be computed using only a few multiplications and additions, while the Kalman filter gain computation required significantly higher number of multiplications as well as divisions, which could be computationally expensive.

In chapter 4, the variations in system dynamics were described by stable uncertainty parameterizations using coprime factorizations [26, 64], which was identified in an online fashion. The main reason for parameterizing the uncertainty is to avoid unnecessary identification of the unchanged part of the plant dynamics. Therefore, the uncertainty identification, in comparison to the complete plant dynamics identification, requires less computational power as well as smaller order for the identified transfer function.

As an example, the adaptive RRO following algorithm introduced in [61, 62] was considered. Stability and convergence of this algorithm require that the phase difference between the actual closed loop transfer functions from feed-forward injection points to PES and their corresponding models must be less than 90 degrees. Temperature variations affected the MA dynamics, particularly the high frequency resonance modes. Therefore, it was necessary to update in real time the MA closed-loop transfer function $\hat{R}_{MA}$, which was used by the adaptive RRO following algorithm.

The coprime factorizations technique was used for an experimental dual-stage HDD in order to parameterize and identify the uncertainty caused by temperature variations in terms of a stable, second order causal transfer function $S \in \mathbb{RH}_{\infty}^{1\times 2}$. Therefore, only identification of the uncertainty parameterization S was required at different temperatures, which reduced the numbers of parameters to be identified as compared to the entire closed loop transfer function identification. The uncertain transfer function S was identified in an online fashion, in three co-adjacent frequency regions. The corresponding updated MA closed-loop transfer function estimate, $\hat{R}_{MA}$, was found to satisfy the robustness criteria for the given experimental dual-stage HDD.

In chapter 5, the frequency based data-driven mixed H_2/H_∞ control design algorithm was studied in order to design feedback loops. The data-driven control design algorithm directly uses the frequency response measurements of the plant in the control design step, rather

than fitting an estimated model to those measurements. Therefore, the obtained controller can guarantee the stability and performance level achieved in the design step, if adequate number of frequency response measurements are considered in the design step to represent system dynamics variations.

The data-driven mixed H_2/H_∞ control design problem was converted to a convex local optimization problem, which was solved iteratively. In the proposed algorithm, the H_2 and H_∞ norms of the closed loop transfer functions had the flexibility to be considered as the constraints and/or the objective of the optimization problem. The H_∞ norm criteria were used for guaranteeing the closed loop stability and shaping the closed loop transfer functions. The H_2 norm criteria were used for constraining or minimizing the variance of signals in the time domain, since H_2 norms of transfer functions in the frequency domain are equivalent to the square root of their corresponding signals variances in the time domain.

The necessary and sufficient convex conditions of the H_∞ norm control problem for SISO systems are obtained in [42]. These results were extended to MISO systems, where the obtained controller stabilized the given MISO system and satisfied the defined H_∞ constraints. These results were combined with H_2 results in [41] in order to form the mixed H_2/H_∞ control problem. The H_2 and H_∞ norms used in this algorithm were defined such that multiple sets of plant measurements could be considered in the design process.

In chapter 6, the proposed data-driven mixed H_2/H_∞ control methodology was used to design a track following controller for a dual-stage HDD. The sensitivity decoupling approach was considered as the control structure [34]. The controllers in this structure were obtained using either sequential SISO or SIMO data-driven control design strategies. In the sequential SISO strategy, the control problem was decoupled into two SISO problems, and the controller for each actuator was obtained in one individual step. In the SIMO strategy, the complete control block was obtained in one step. It is worth mentioning that the dual-stage controller should be designed such that in the case of MA failure, the single-stage loop remains stable and satisfies predefined performance characteristics. The single-stage and dual-stage stability and performance characteristics were considered together as the constraints and the objectives of the optimization problem.

The dual-stage HDD controller was designed considering the set of five frequency response plant measurement data sets. The closed loop transfer functions for all these data sets were shaped using the weighted H_∞ norm constraints. Since the H_2 norms of closed loop transfer functions are directly related to the square roots of variances for the corresponding signals in the time domain, the H_2 norm objective and constraints were imposed using the variances of closed loop signals, which were averaged among the set of five frequency response plant measurement data sets. The average variance of the tracking error was considered as the minimization objective, while the VCM control input and the MA output stroke average variances were constrained.

The design results demonstrated that the data driven mixed H_2/H_∞ control design algorithm was successful in satisfying the defined mixed H_2/H_∞ control objectives by designing controllers, which stabilized both the single-stage and the dual-stage loops. Considering the set of five frequency response plant measurement data sets, the SIMO design strategy

achieved a smaller average variance of the dual-stage tracking error as well as a higher worst case bandwidth as compared to the sequential SISO design strategy, since it designed the controllers for the VCM and MA simultaneously. Also, the more stringent restriction on the MA output stroke in the SIMO design strategy compromised the worst case dual-stage bandwidth as well as the average variance of the dual-stage tracking error.

7.2 Future Work

In the frequency based data-driven control design problem discussed in chapter 5 and 6, multiple sets of frequency response measurements from the system are required in order to capture the uncertainties and dynamics variations in the design step. The proposed algorithm can accommodate multiple measurements in the design process. However, the size of optimization problem, including variables and constraints, grows linearly by increasing the number of measurements, which makes the algorithm computationally expensive and impractical for large number of frequency response measurements.

In order to make this algorithm practical for the large number of measurements, the very first solution is to improve the computational efficiency of the proposed algorithm. The more efficient algorithm reduces the memory usage and increases the number of measurements which can be handled by this algorithm.

The other possible solution for accommodating more plant measurements in the design process is to cluster the plant measurements. Assume that a significant number of frequency response measurement data sets from an uncertain plant are available. The objective is to derive an efficient algorithm, which can cluster the frequency response measurements, based on the dynamics uncertainties, and pick a few measurements from each cluster, which can represent the dynamics uncertainties in that cluster.

The H_∞ control problem is addressed for MISO systems by deriving sufficient and necessary convex conditions for the H_∞ constraints. However, these results cannot be used for systems with multiple feedback measurements. It is proposed to extend the developed H_∞ control algorithm to the MIMO systems. The extended algorithm will be useful in variety of control system designs such as vibration rejection algorithms in HDDs, where accelerometer measurement is available in addition to the head position signal. In this case, the accelerometer measurement can be augmented into the plant model such that the augmented plant has acceleration measurement in addition to the head position as the plant measurement outputs. Therefore, the MIMO extension of the algorithm can be used to design a desired feedback controller.

In order to consider the H_∞ constraints in the data-driven control design problem for MIMO systems, the H_∞ constraints should be converted into convex inequalities. However, deriving these convex inequalities for the case of MIMO systems is not as straightforward as the MISO systems shown in theorem 5.3.1. Here, it will be demonstrated how to convert a H_∞ norm constraint of a stable MIMO system to an inequality between singular values and Frobenius norms of specific expressions which are linear functions of controller factorizations.
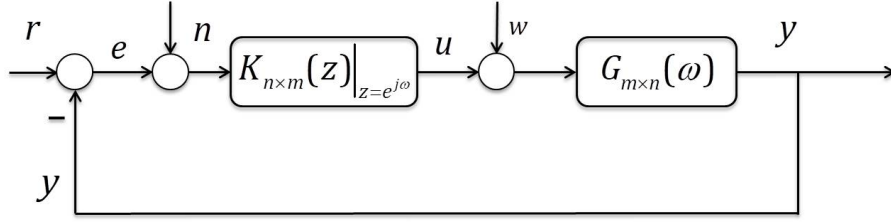
Figure 7.1: Control block diagram. $G_{m \times n}(\omega)$ represents the frequency response data of the plant.

However, the obtained inequality is not necessarily convex. The interested reader may be able to find a convex equivalent for this inequality using similar approaches as the ones used in proof of Lemma A.0.0.1 in appendix A.

Consider the frequency response of a stable system with n inputs and m outputs denoted by $G_{m \times n}$. Fig. 7.1 represents the general feedback structure for this plant. The objective is to find a stabilizing controller $K_{n \times m}(z)$ with the following stable factorizations

$$K_{n \times m}(z) = X_{n \times m}(z) Y_{m \times m}^{-1}(z), \tag{7.1}$$

such that the closed loop transfer function from reference signal to control input, $U_{r \to u}^{n \times m}$, satisfies the following H_∞ constraint

$$\left\| W_{U_{r \to u}} U_{r \to u}^{n \times m} \right\|_\infty < 1, \tag{7.2}$$

where $W_{U_r} \in \mathbb{C}^{l \times n}$ is a bounded frequency response function used to shape the closed loop transfer function. The closed loop transfer function in terms of controller stable factorizations can be obtained as

$$U_{r \to u}^{n \times m} = X_{n \times m}(Y_{m \times m} + G_{m \times n} X_{n \times m})^{-1}. \tag{7.3}$$

Therefore, the term inside the H_∞ norm constraint given in Eq. (7.2) can be simplified as

$$W_{U_{r \to u}} U_{r \to u}^{n \times m} = Q_{n \times m} P_{m \times m}^{-1}, \tag{7.4}$$

where

$$Q_{n \times m} = W_U X_{n \times m}, \tag{7.5}$$

$$P_{m \times m} = Y_{m \times m} + G_{m \times n} X_{n \times m}. \tag{7.6}$$

The parameters $Q_{n \times m}$ and $P_{m \times m}$ are linear functions of controller stable factorizations. According to [41], the H_∞ norm mentioned in (7.2) is equivalent to the following inequality

$$Q_{n \times m}^* Q_{n \times m} \prec P_{m \times m}^* P_{m \times m}, \tag{7.7}$$

where $\prec$ represents the matrix inequality and the singular value decomposition of the P and Q terms are

$$Q_{n \times m} = U_{Q, \ n \times n} \Sigma_{Q, \ n \times m} V_{Q, \ m \times m}^*, \tag{7.8}$$

$$P_{m \times m} = U_{P, \ m \times m} \Sigma_{P, \ m \times m} V_{P, \ m \times m}^*. \tag{7.9}$$

In these decompositions, $U_{Q,\ n\times n}$, $V_{Q,\ m\times m}$, $U_{P,\ m\times m}$ and $V_{P,\ m\times m}$ are all unitary matrices, and $\Sigma_{Q,\ n\times m}$ and $\Sigma_{P,\ m\times m}$ are rectangular diagonal matrices containing the singular values of Q and P. Without loss of generality, it can be assumed that $m > n$. Therefore, the singular values matrices are given by

$$\Sigma_{Q,\ n\times m} = \begin{bmatrix} \sigma_1^2(Q_{n\times m}) & 0 & .. & 0 & .. & 0 \\ 0 & \sigma_2^2(Q_{n\times m}) & .. & 0 & .. & 0 \\ .. & .. & .. & .. & .. & 0 \\ 0 & 0 & .. & \sigma_n^2(Q_{n\times m}) & .. & 0 \end{bmatrix} \tag{7.10}$$

and

$$\Sigma_{P,\ m\times m} = \begin{bmatrix} \sigma_1^2(P_{m\times m}) & 0 & .. & 0 \\ 0 & \sigma_2^2(P_{m\times m}) & .. & 0 \\ .. & .. & .. & .. \\ 0 & 0 & .. & \sigma_n^2(P_{m\times m}) \end{bmatrix}. \tag{7.11}$$

Substituting the singular value decompositions given in Eqs. (7.8) and (7.9) into Eq. (7.7) will result in

$$V_{Q,\ m\times m}\Sigma_{Q,\ n\times m}^{*}\Sigma_{Q,\ n\times m}V_{Q,\ m\times m}^{*} \prec V_{P,\ m\times m}\Sigma_{P,\ m\times m}^{*}\Sigma_{P}V_{P,\ m\times m}. \tag{7.12}$$

Multiplying left side of this inequality by $V_{Q,\ m\times m}^{*}$ and the right side by $V_{Q,\ m\times m}$ will lead to the following inequality

$$\Sigma_{Q,\ n\times m}^{*}\Sigma_{Q,\ n\times m} \prec V_{m\times m}\Sigma_{P,\ m\times m}^{*}\Sigma_{P}V_{m\times m}, \tag{7.13}$$

where $V_{m\times m} = V_{Q,\ m\times m}^{*}V_{P,\ m\times m}$ are also the unitary matrices. According to Eqs. (7.10) and (7.11), Eq. (7.13) can be expanded in the following form

$$\begin{bmatrix} \sigma_1^2(Q_{n\times m}) & 0 & .. & 0 \\ 0 & \sigma_2^2(Q_{n\times m}) & .. & 0 \\ .. & .. & .. & .. \\ 0 & 0 & .. & \sigma_n^2(Q_{n\times m}) \end{bmatrix} \prec$$

$$\begin{bmatrix} V_{m\times m}^{(1)} & V_{m\times m}^{(2)} & .. & V_{m\times m}^{(n)} \end{bmatrix} \begin{bmatrix} \sigma_1^2(P_{m\times m}) & 0 & .. & 0 \\ 0 & \sigma_2^2(P_{m\times m}) & .. & 0 \\ .. & .. & .. & .. \\ 0 & 0 & .. & \sigma_n^2(P_{m\times m}) \end{bmatrix} \begin{bmatrix} V_{m\times m}^{(1)*} \\ V_{m\times m}^{(2)*} \\ .. \\ V_{m\times m}^{(n)*} \end{bmatrix}, \tag{7.14}$$

where $V_{m\times m}^{(i)}$ is the ith column of vector $V_{m\times m}$. Since $V_{m\times m}$ is a unitary matrix and the singular matrix is diagonal, the right side of the above inequality is equal to $\sum_{i=1}^{n}\sigma_i^2(P).I_n$, and I_n is the identity matrix of size n. Therefore, the H_∞ constraint in Eq. (7.2) is equivalent to the following inequality

$$\forall i \ \in \ \{1,2,..,n\}: \ \sigma_i^2(Q_{n\times m}) < \sum_{i=1}^{n}\sigma_i^2(P_{m\times m}). \tag{7.15}$$

The Frobenius norm of a matrix P is defined as

$$\|P_{m\times m}\|_F^2 = \sum_{i=1}^{n}\sum_{j=1}^{n}|p_{ij}|^2,\tag{7.16}$$

where p_{ij} represents the element in row i and column j of the matrix $P_{m\times m}$. It has been shown in [65] that the Frobenius norm can also be obtained using singular values of the matrix

$$\|P_{m\times m}\|_F^2 = \sum_{i=1}^{n}\sigma_i^2(P_{m\times m}).\tag{7.17}$$

Therefore, Eq. (7.15) can also be written as

$$\forall i \in \{1,2,..,n\}: \ \sigma_i^2(Q_{m\times m}) < \|P_{m\times m}\|_F^2,\tag{7.18}$$

or equivalently

$$\forall i \in \{1,2,..,n\}: \ \sigma_i^2(Q_{n\times m}) < \sum_{i=1}^{n}\sum_{j=1}^{n}|p_{ij}|^2.\tag{7.19}$$

According to Eqs. (7.15), (7.18) and (7.19), the H_∞ constraints for a MIMO system defined in Eq. (7.2) are translated to an inequality between singular values of $Q_{n\times m}$ and a quadratic convex function of the parameter $P_{m\times m}$, which can be represented in terms of singular values, Frobenius norm or square of matrix elements. The challenge which is proposed as a future work is to find a convex equivalent for these inequalities as it was obtained in appendix A for MISO systems.

Appendix A

Proof of Theorem 5.3.1

Theorem 5.3.1 is stated and proved for SISO systems in [42]. In this section, the proof presented in [42] is extended to MISO systems. In order to prove theorem 5.3.1, Lemma A.0.0.1 is first proved [55].

All transfer functions are considered in the discrete time frequency domain. However to make the notations simple, the frequency dependence arguments $(e^{j\omega})$ and (ω) will not be written in the transfer functions. The feedback system shown in Fig. 5.1 is also plotted here in Fig. A.1 as a reference.

Lemma A.0.0.1. *Assume the transfer function $W_{U_{w\to u}}U_{w\to u}$ used in theorem 5.3.1 is bounded and analytic in the right half plane, where $U_{w\to u}$ is written in terms of plant and controller stable factorizations in Eq. (5.45). The H_∞ norm defined in Eq. (5.47) is satisfied if and only if the following inequality holds over the entire frequency region, Ω,*

$$\forall \omega \in \Omega : \ \gamma^{-1}\bar{\sigma}(W_{U_\omega}X\tilde{N}F) < Re(\tilde{N}XF + \tilde{M}YF) \tag{A.1}$$

where $F \in \mathbb{RH}_\infty$ is a stable proper rational scalar transfer function and $\sigma(\bar{M})$ denotes the maximum singular value of the matrix M.
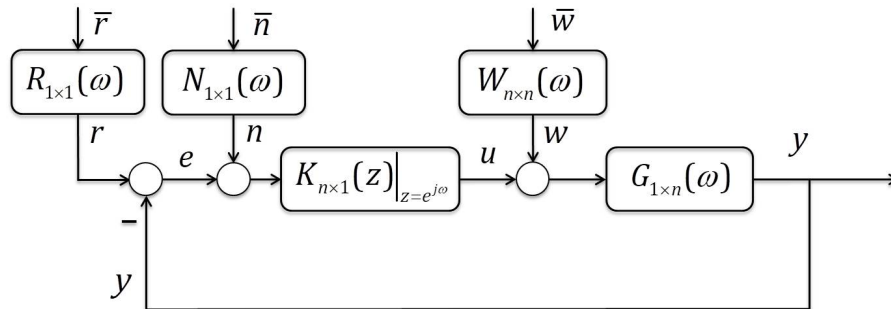

Figure A.1: Control block diagram. $G_{1\times n}(\omega)$ represents the frequency response data of the plant. The disturbances to the system are colored by the weighting functions $R(\omega)$, $N(\omega)$ and $W(\omega)$.
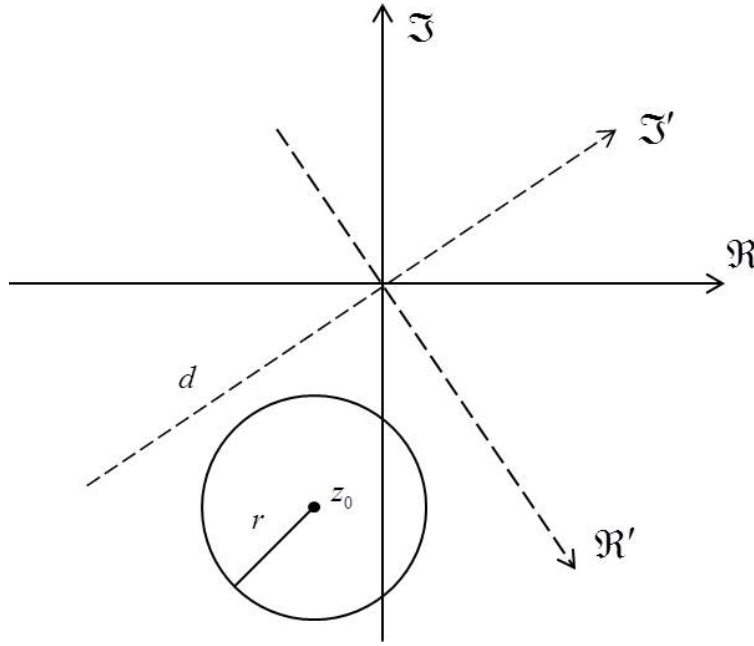
Figure A.2: $\mathbb{R}$ and $\mathbb{I}$ represent the real and imaginary axes, respectively. The prime notation is used to represent the rotated axes.

Proof of Lemma A.0.0.1

Proof. Considering the definition of H_∞ norm in Eq. (1.9), the weighted H_∞ norm criterion given in Eq. (5.47) can be written as

$$\forall \omega \in \Omega : \ \bar{\sigma}(W_{U_{w \to u}} X \tilde{N}(\tilde{N}X + \tilde{M}Y)^{-1}) < \gamma. \tag{A.2}$$

According to the dimensions of plant and controller stable factorizations given in Eqs. (5.1) and (5.2), the term $\tilde{N}X + \tilde{M}Y$ will be a scalar. Therefore, the above equation can be simplified as follows

$$\forall \omega \in \Omega : \ \gamma^{-1}\bar{\sigma}(W_{U_{w \to u}} X \tilde{N}) < \left| \tilde{N}X + \tilde{M}Y \right|. \tag{A.3}$$

where $|G| = |G(\omega)|$ denotes the magnitude of $G(\omega)$.

At each given frequency $\omega \in \Omega$, a disk centered at $z_0 = \tilde{N}X + \tilde{M}Y$ with radius $r = \gamma^{-1}\bar{\sigma}(W_{U_{w \to u}} X \tilde{N})$ will be considered. This disk is shown in Fig. A.2, where all the points inside this disk will be represented as

$$|z - z_0| < r \tag{A.4}$$

By combining Eqs. (A.3) and (A.4), it can be concluded that the origin $z = (0,0)$ is not located inside this disk. Therefore, as one can see in Fig. A.2, there exists a line d passing

through the origin that does not intersect the disk. A unitary rotation matrix $f(j\omega)$ will be considered which makes line d the new imaginary axis. The center and radius of the disk in the new rotated system will be given by

$$z_0^f = \tilde{N}Xf + \tilde{M}Yf, \tag{A.5}$$
$$r^f = \gamma^{-1}\bar{\sigma}(W_{U_\omega}X\tilde{N}f). \tag{A.6}$$

Since line d is the new imaginary axis and is not intersecting with the disk, the real component of the disk center must be always greater than the disk radius

$$r^f < Re(z_0^f). \tag{A.7}$$

Plugging in Eqs. (A.5) and (A.6) into Eq. (A.7) will result in the following inequality

$$\forall \omega \in \Omega : \ \gamma^{-1}\bar{\sigma}(W_{U_{w\to u}}X\tilde{N}f) < Re(\tilde{N}Xf + \tilde{M}Yf). \tag{A.8}$$

According to [55], f can be approximated by the frequency response data of a stable proper rational scalar transfer function F, if and only if

$$V = \frac{1}{\left|\tilde{N}X + \tilde{M}Y\right| - \gamma^{-1}\bar{\sigma}(W_{U_{w\to u}}X\tilde{N})} \tag{A.9}$$

is analytic in the right half plane for all $\bar{\gamma} > \gamma$. In order to prove that V is analytic in the right half plane, we first assume $\bar{\gamma} \to \infty$. Therefore, $V = \frac{1}{\left|\tilde{N}.X+\tilde{M}.Y\right|}$ is stable and analytic according to stability of $U_{w\to u}$. If $\bar{\gamma}$ is reduced from infinity to γ, the poles of V will move continuously, and according to Eq. (A.3), it can be shown that

$$\forall \omega \in \Omega : V^{-1}(j\omega) \neq 0. \tag{A.10}$$

Therefore, the function V will remain analytic in the right half plane for all $\bar{\gamma} > \gamma$. As a result, the rotation matrix $f(j\omega)$ can be estimated by a stable proper rational scalar transfer function F, which will prove the inequality given in Eq. (A.1). $\qquad\square$

Proof of Theorem 5.3.1

Proof. The equivalence of statements I and II presented in theorem 5.3.1 will be proved here.

- $(I \Rightarrow II)$ Assume the stabilizing controller is factorized as $K = X_0 Y_0^{-1}$. According to Lemma A.0.0.1, the H_∞ norm criterion given in Eq. (5.47) can be written as

$$\forall \omega \in \Omega : \gamma^{-1}\bar{\sigma}(W_{U_{w\to u}}X_0\tilde{N}F) < Re(\tilde{N}X_0F + \tilde{M}Y_0F). \tag{A.11}$$

  Since F is a stable proper rational scalar transfer function, it can be merged inside the controller factorizations such that $X = X_0 F$ and $Y = Y_0 F$. This merge will not change the controller and $K = XY^{-1} = X_0 Y_0^{-1}$. Therefore, Eq. (A.11) will result in Eq. (5.48) given in statement II of the theorem.

- ($II \Rightarrow I$) The real part of any complex number is always less than its magnitude

$$Re(\ \tilde{N}X + \tilde{M}Y\ ) < \left|\ \tilde{N}X + \tilde{M}Y\ \right|. \tag{A.12}$$

Therefore, Eq. (5.48) will result in the following equation

$$\forall \omega \in \Omega:\ \gamma^{-1}\bar{\sigma}(W_{U_\omega}X\tilde{N}) < \left|\ \tilde{N}X + \tilde{M}Y\ \right|. \tag{A.13}$$

Since $\tilde{N}X + \tilde{M}Y$ is a scalar term, Eq. (A.13) can be written as

$$\forall \omega \in \Omega:\ \bar{\sigma}(W_{U_{w \to u}}X\tilde{N}(\tilde{N}X + \tilde{M}Y)^{-1}) < \gamma \tag{A.14}$$

According to the definition of the weighted H_∞ norm given in Eq. (1.9), the above equation is basically equivalent to the H_∞ criterion given in Eq. (5.47).

Now, we have to show that the controller K stabilizes the plant G. The stability is analyzed using the Nyquist stability theorem[72]. According to Eq. (5.25), the closed loop transfer functions can be written as follows

$$\begin{bmatrix} E_{r \to e} & E_{n \to e} & E_{w \to e} \\ U_{r \to u} & U_{n \to u} & U_{w \to u} \\ Y_{r \to y} & Y_{n \to y} & Y_{w \to y} \end{bmatrix} = \frac{1}{D} \begin{bmatrix} \tilde{M}Y & -X\tilde{N} & -\tilde{N}Y \\ \tilde{M}X & \tilde{M}X & -\tilde{N}X \\ \tilde{N}X & \tilde{N}X & \tilde{N}Y \end{bmatrix}, \tag{A.15}$$

where

$$D = \tilde{N}X + \tilde{M}Y. \tag{A.16}$$

Since all the elements of the numerator matrix in Eq. (A.15) are stable factorizations of the plant and controller, they will have stable poles. Therefore, the closed loop systems in Eq. (A.15) will be stable if all the zeros of D are stable.

In order to prove that the zeros of D are stable, the Nyquist plot for D will be considered. Since D is a linear function of stable factorizations, it will not have any unstable poles. Moreover, Eq. (5.48) will result in

$$Re(D(\omega)) > 0, \tag{A.17}$$

which means that D will not encircle around the origin. As a result, the Nyquist stability theorem will conclude that D will not have any unstable zeros. Therefore, all the closed loop systems in Eq. (A.15) are stable and the controller K stabilizes the plant G.

□

Appendix B

The H_∞ constraints

The closed loop transfer functions considered in the H_∞ norm constraints given in Eqs. (6.4), (6.5), (6.8) and (6.9) are plotted in this section. These plots include the closed loop transfer functions, as well as the weighting functions used to shape those transfer functions. The closed loop transfer functions are obtained for all the design scenarios in table 6.1 using all the frequency response data sets in Fig. 6.3. These plots utilize the color code in table 6.1 to distinguish between different scenarios. However, the plots for the same scenario but different frequency response data sets utilize the same color code and may not be distinguishable from each other at some frequency regions, where the plots are relatively close to each other.

According to Eq. (5.28) which is obtained for the SISO transfer functions, the inverse of the weighting functions magnitude shapes the magnitude of the closed loop transfer functions. The inverse of weighting functions for the single-stage loop as well as individual SISO loops in the dual-stage loop are shown in Figs. B.1, B.3a, B.4 and B.5 with light blue dotted lines. The closed loop transfer functions are also shown with their corresponding color code mentioned in table B.1.

Table B.1: Controller design scenarios and their color code.

Scenarios	$SIMO_1$	$SIMO_2$	$SIMO_3$	$SIMO_4$	$SISO_1$
Design strategy	SIMO	SIMO	SIMO	SIMO	sequential SISO
η_{y_m} (nm^2)	44^2	42^2	40^2	38^2	44^2
Color code	▬	▬	▬	▬	▬

The transfer functions for the dual-stage loops are plotted in Fig. B.2. $E_{r\to e}$ is a SISO and $E_{w\to e}$, $U_{r\to u}$, $U_{w\to u}$ are MIMO transfer functions. The weighting functions used to shape

the MIMO transfer functions in Eq. (6.5) are as follows

$$\forall \omega \in \Omega : W_{E_{w \to e}}(\omega) = \begin{bmatrix} 0.10 \\ 0.10 \end{bmatrix}, \tag{B.1}$$

$$\forall \omega \in \Omega : W_{E_{r \to u}}(\omega) = \begin{bmatrix} 0.10 & 0.00 \\ 0.00 & 0.10 \end{bmatrix}, \tag{B.2}$$

$$\forall \omega \in \Omega : W_{E_{w \to u}}(\omega) = \begin{bmatrix} 0.10 & 0.10 \\ 0.04 & 0.10 \end{bmatrix}. \tag{B.3}$$

According to Eq. (5.33), the weighting functions in the MIMO transfer functions shape the maximum singular values of the closed loop transfer functions by limiting them to be smaller than the inverse of minimum singular values of the weighting transfer functions across the entire frequency region. Figs. B.3b-B.3d plot the maximum singular values of closed loop transfer functions with the color code mentioned in table B.1 and the inverse of the minimum singular values of the weighting functions with light blue dotted lines.

All the values corresponding to SISO and MIMO closed loop transfer functions plotted in this section are smaller than their upper-bounds shown with light blue dotted lines. Therefore, all these closed loop transfer functions satisfy the H_∞ constraints defined in Eqs. (6.4), (6.5), (6.8) and (6.9).

(a) $E^s_{r \to e}$, $\left|W_{E_{r \to e}}\right|^{-1}$

(b) $E^s_{w_v \to e}$, $\left|W_{E^s_{w_v \to e}}\right|^{-1}$

(c) $U^s_{r \to u_v}$, $\left|W_{U^s_{r \to u_v}}\right|^{-1}$

(d) $U^s_{w_v \to u_v}$, $\left|W_{U^s_{w_v \to u_v}}\right|^{-1}$
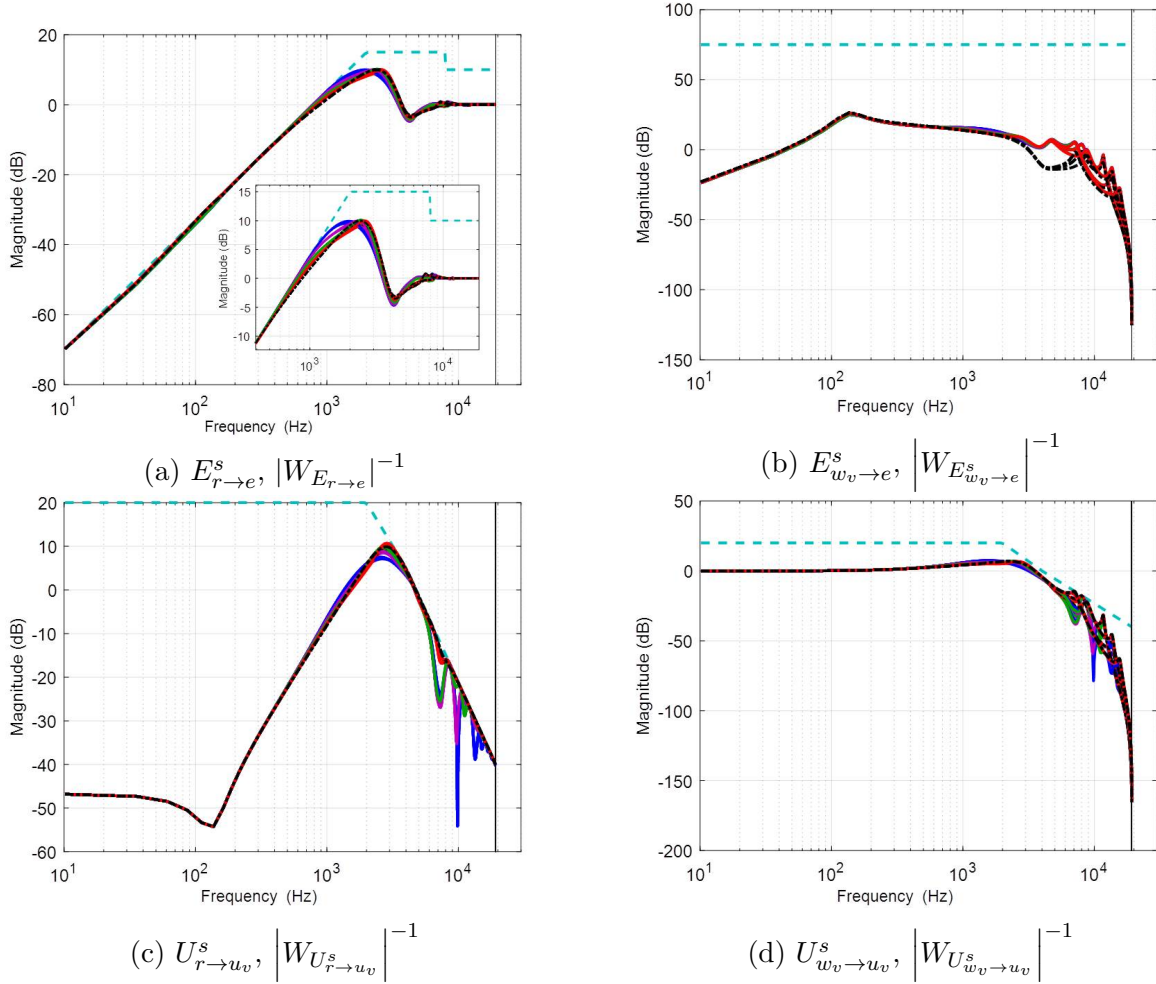
Figure B.1: The magnitude Bode plots of the single-stage closed loop transfer functions (H) and the inverse of the H_∞ weighting functions magnitudes ($|W_H|^{-1}$). The $|W_H|^{-1}$ functions are shown with the light blue dotted lines. The H_∞ norm criteria are provided in Eq. (6.4). These plots include 25 closed loop transfer functions for all the 5 design scenarios in table 6.1 using all the 5 frequency response data sets in Fig. 6.3.

(a) $E_{r \to e}$

(b) $E_{w \to e}$, $w = \begin{bmatrix} w_v & w_m \end{bmatrix}^T$

(c) $U_{r \to u}$, $u = \begin{bmatrix} u_v & u_m \end{bmatrix}^T$

(d) $U_{w \to u}$, $w = \begin{bmatrix} w_v & w_m \end{bmatrix}^T$, $u = \begin{bmatrix} u_v & u_m \end{bmatrix}^T$

Figure B.2: The magnitude Bode plots of the dual-stage closed loop transfer functions. These plots include 25 closed loop transfer functions for all the 5 design scenarios in table 6.1 using all the 5 frequency response data sets in Fig. 6.3.

(a) $\bar{\sigma}(E_{r\to e})$, $\underline{\sigma}^{-1}(W_{E_{r\to e}})$

(b) $\bar{\sigma}(E_{w\to e})$, $\underline{\sigma}^{-1}(W_{E_{w\to e}})$

(c) $\bar{\sigma}(U_{r\to u})$, $\underline{\sigma}^{-1}(W_{U_{r\to u}})$

(d) $\bar{\sigma}(U_{w\to u})$, $\underline{\sigma}^{-1}(W_{U_{w\to u}})$

Figure B.3: The maximum singular values of the dual-stage closed loop transfer functions H shown as $\bar{\sigma}(H)$ and the inverse of the minimum singular values of the H_∞ weighting functions ($\underline{\sigma}^{-1}(W_H)$). The $\underline{\sigma}^{-1}(W_H)$ functions are shown with the light blue dotted lines. The H_∞ norm criteria are provided in Eq. (6.5). These plots include 25 closed loop transfer functions for all the 5 design scenarios in table 6.1 using all the 5 frequency response data sets in Fig. 6.3.

(a) $E_{w_v \to e}$, $\left| W_{E_{w_v \to e}} \right|^{-1}$ (b) $E_{w_m \to e}$, $\left| W_{E_{w_m \to e}} \right|^{-1}$
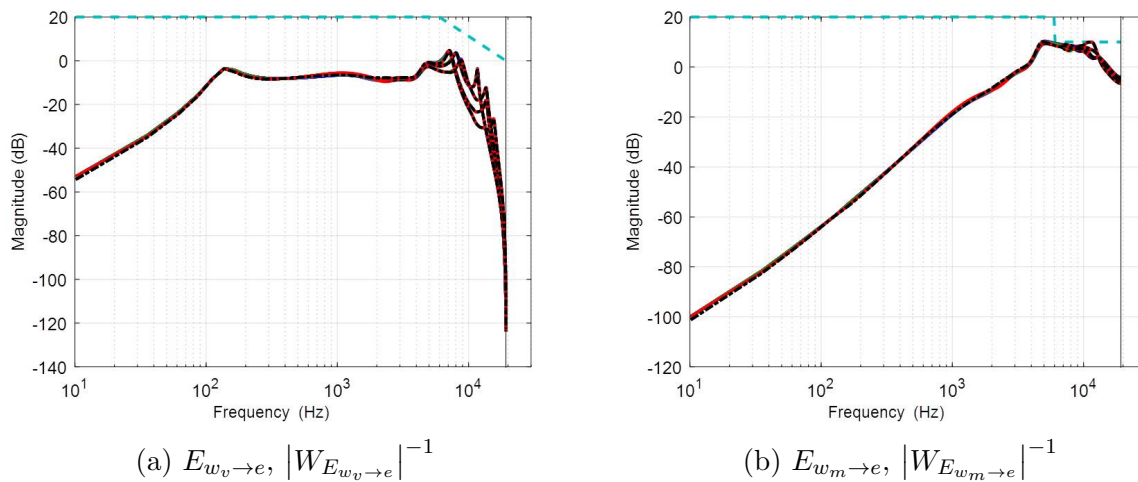
Figure B.4: The magnitude Bode plots of the individual SISO closed loop transfer functions to the tracking error in the dual-stage HDD (H) and the inverse of their H_∞ weighting functions magnitudes ($|W_H|^{-1}$). The $|W_H|^{-1}$ functions are shown with the light blue dotted lines. The H_∞ norm criteria are provided in Eq. (6.8). These plots include 25 closed loop transfer functions for all the 5 design scenarios in table 6.1 using all the 5 frequency response data sets in Fig. 6.3.
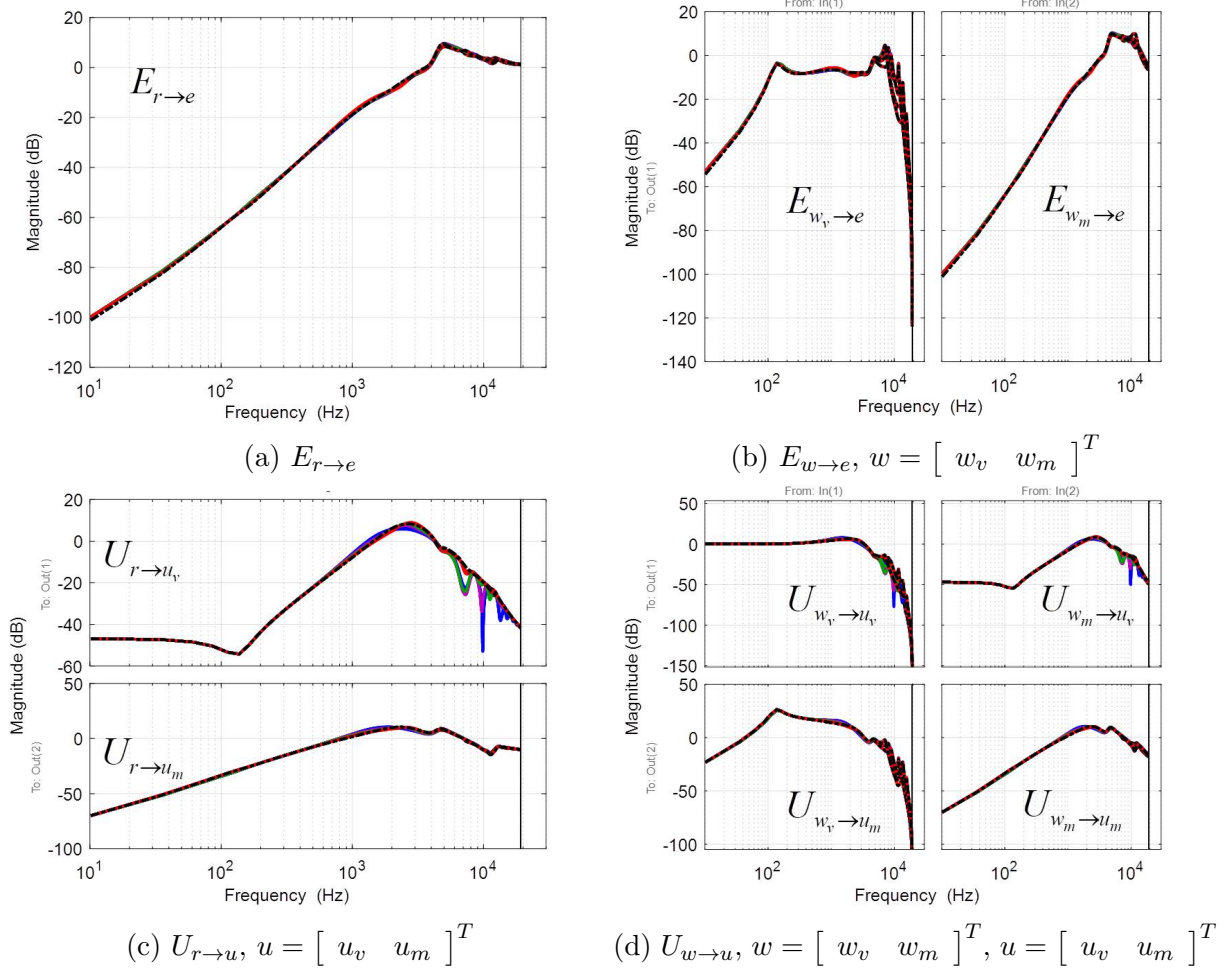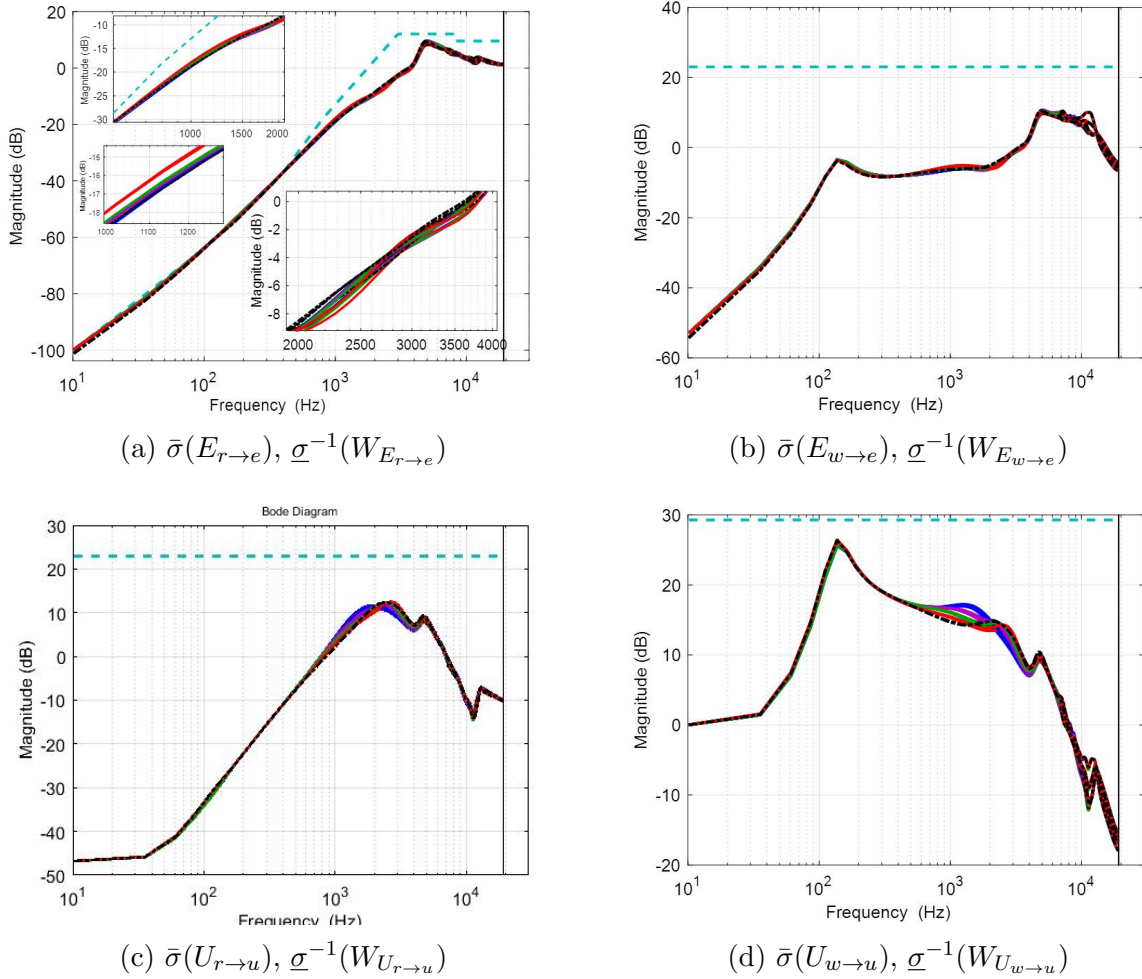
(a) $U_{r \to u_v}$, $\left| W_{U_{r \to u_v}} \right|^{-1}$

(b) $U_{r \to u_m}$, $\left| W_{U_{r \to u_m}} \right|^{-1}$

(c) $U_{w_v \to u_v}$, $\left| W_{U_{w_v \to u_v}} \right|^{-1}$

(d) $U_{w_v \to u_m}$, $\left| W_{U_{w_v \to u_m}} \right|^{-1}$

(e) $U_{w_m \to u_v}$, $\left| W_{U_{w_m \to u_v}} \right|^{-1}$

(f) $U_{w_m \to u_m}$, $\left| W_{U_{w_m \to u_m}} \right|^{-1}$

Figure B.5: The magnitude Bode plots of the individual SISO closed loop transfer functions to the control inputs in the dual-stage HDD (H) and the inverse of their H_∞ weighting functions magnitudes ($|W_H|^{-1}$). The $|W_H|^{-1}$ functions are shown with the light blue dotted lines. The H_∞ norm criteria are provided in Eq. (6.9). These plots include 25 closed loop transfer functions for all the 5 design scenarios in table 6.1 using all the 5 frequency response data sets in Fig. 6.3.
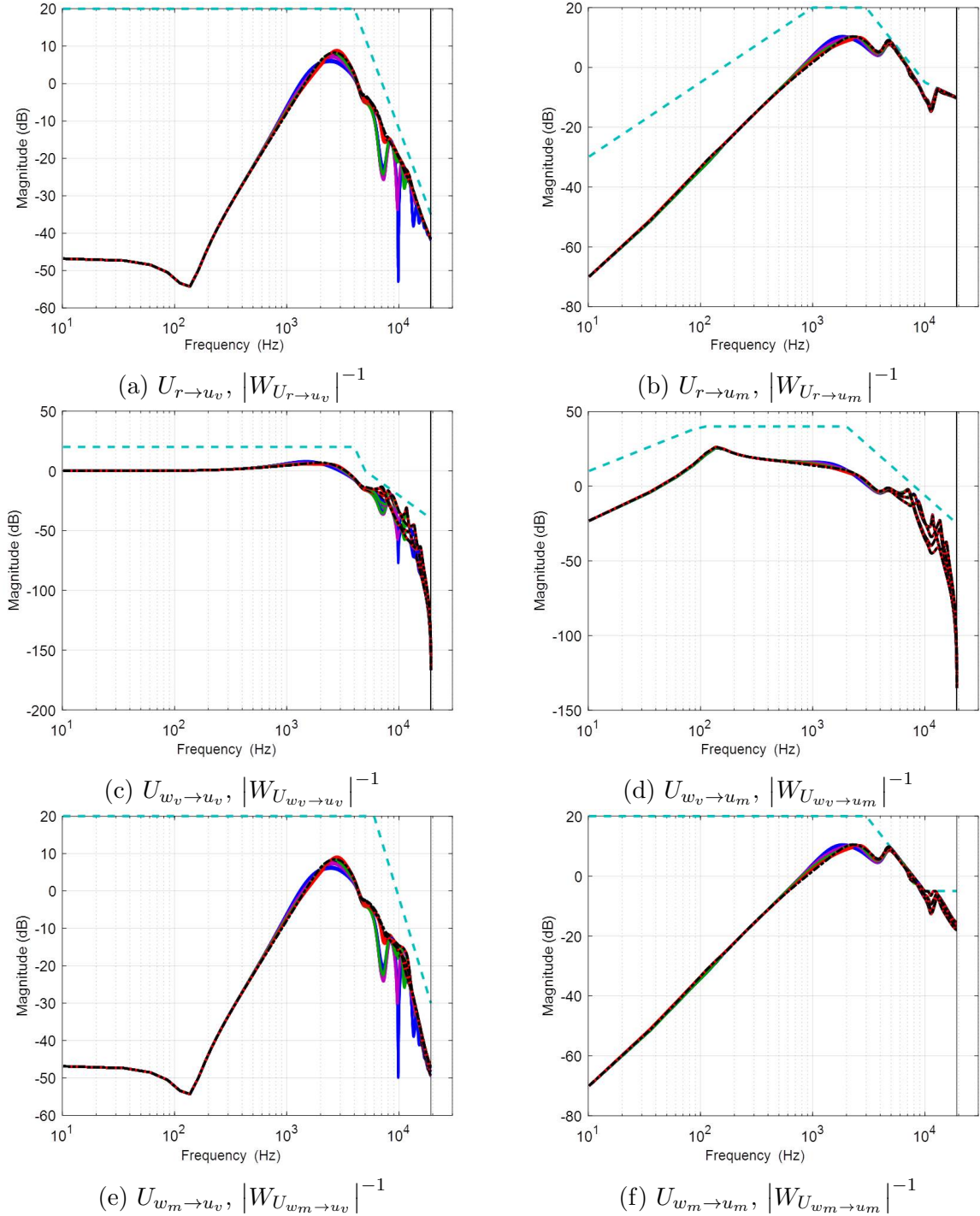
Bibliography

[1]   Daniel Abramovitch and Gene Franklin. "A brief history of disk drive control". In: *IEEE Control Systems* 22.3 (2002), pp. 28–42.

[2]   Vinay K Agarwal and Robert L Cloke. *Using an external spiral servo writer to write spiral reference patterns to a disk to facilitate writing product servo bursts to the disk.* US Patent 6,992,848. Jan. 2006.

[3]   Sanjay K Aggarwal, David A Horsley, Roberto Horowitz, and Albert P Pisano. "Micro-actuators for high density disk drives". In: *American Control Conference, 1997. Proceedings of the 1997.* Vol. 6. IEEE. 1997, pp. 3979–3984.

[4]   Muhammad Tahir Akhtar, Masahide Abe, and Masayuki Kawamata. "A new variable step size LMS algorithm-based method for improved online secondary path modeling in active noise control systems". In: *Audio, Speech, and Language Processing, IEEE Transactions on* 14.2 (2006), pp. 720–726.

[5]   Abdullah Al Mamun, GuoXiao Guo, and Chao Bi. *Hard disk drive: mechatronics and control.* Vol. 23. CRC press, 2006.

[6]   Abdullah Al Mamun, Iven Mareels, TH Lee, and Arthur Tay. "Dual stage actuator control in hard disk drive-a review". In: *Industrial Electronics Society, 2003. IECON'03. The 29th Annual Conference of the IEEE.* Vol. 3. IEEE. 2003, pp. 2132–2137.

[7]   Athanasios C Antoulas. *Approximation of large-scale dynamical systems.* SIAM, 2005.

[8]   MOSEK ApS. *The MOSEK optimization toolbox for MATLAB manual. Version 7.1 (Revision 28).* 2015. URL: http://docs.mosek.com/7.1/toolbox/index.html.

[9]   Takenori Atsumi, Toshihiro Arisaka, Toshihiko Shimizu, and Takashi Yamaguchi. "Vibration servo control design for mechanical resonant modes of a hard-disk-drive actuator". In: *JSME International Journal Series C Mechanical Systems, Machine Elements and Manufacturing* 46.3 (2003), pp. 819–827.

[10] Omid Bagherieh and Roberto Horowitz. "Improved Feed-Forward Control in Track Seeking Using Iterative Learning Control". In: *ASME 2016 Conference on Information Storage and Processing Systems.* American Society of Mechanical Engineers. 2016, V001T03A002–V001T03A002.

[11] Omid Bagherieh, Behrooz Shahsavari, and Roberto Horowitz. "Online identification of system uncertainties using coprime factorizations with application to hard disk drives". In: *ASME 2015 Dynamic Systems and Control Conference.* American Society of Mechanical Engineers. 2015, V002T23A006–V002T23A006.

[12] Omid Bagherieh, Behrooz Shahsavari, Ehsan Keikha, and Roberto Horowitz. "Observer Design for Non-Uniform Sampled Systems Using Gain-Scheduling". In: *ASME 2014 Conference on Information Storage and Processing Systems.* American Society of Mechanical Engineers. 2014, V001T03A004–V001T03A004.

[13] Bill Baker, Steven Lambert, Jong Lin, Michael Anthony Moser, and Shu-Yu Sun. *Self-writing of servo patterns based on printed reference pattern in rotating disk drive.* US Patent 6,304,407. Oct. 2001.

[14] Alexandre Sanfelice Bazanella, Lucíola Campestrini, and Diego Eckhard. *Data-driven controller design: the H2 approach.* Springer Science & Business Media, 2011.

[15] Stephen Boyd and Lieven Vandenberghe. *Convex optimization.* Cambridge university press, 2004.

[16] Dana H Brown, Thomas C Christensen, Earl A Cunningham, and Wayne A Rogelstad. *Self servo writing file.* US Patent 5,570,247. Oct. 1996.

[17] Ben M Chen, Tong H Lee, Venkatakrishnan Venkataramanan, and Ben M Chen. *Hard disk drive servo systems.* Springer Berlin, 2002.

[18] Xu Chen and Masayoshi Tomizuka. "A minimum parameter adaptive approach for rejecting multiple narrow-band disturbances with application to hard disk drives". In: *IEEE Transactions on Control Systems Technology* 20.2 (2012), pp. 408–415.

[19] Xu Chen and Masayoshi Tomizuka. "Selective model inversion and adaptive disturbance observer for time-varying vibration rejection on an active-suspension benchmark". In: *European Journal of Control* 19.4 (2013), pp. 300–312.

[20] YangQuan Chen, Kevin L Moore, Jie Yu, and Tao Zhang. "Iterative learning control and repetitive control in hard disk drive industry-a tutorial". In: *Decision and Control, 2006 45th IEEE Conference on.* IEEE. 2006, pp. 2338–2351.

[21] Kok Kia Chew and Masayoshi Tomizuka. "Digital control of repetitive errors in disk drive systems". In: *American Control Conference, 1989.* IEEE. 1989, pp. 540–548.

[22] Robert L Cloke. *Disk drive for circular self servo writing and spiral self servo writing using prewritten reference servo bursts.* US Patent 6,977,789. 2005.

[23] Jan De Caigny, Juan F Camino, Ricardo CLF Oliveira, Pedro LD Peres, and Jan Swevers. "Gain-scheduled dynamic output feedback control for discrete-time LPV systems". In: *International Journal of Robust and Nonlinear Control* 22.5 (2012), pp. 535–558.

[24] Jan De Caigny, Juan F Camino, Ricardo CLF Oliveira, Pedro Luis Dias Peres, and Jan Swevers. "Gain-scheduled H2 and Hinf control of discrete-time polytopic time-varying systems". In: *IET control theory & applications* 4.3 (2010), pp. 362–380.

[25] Jiagen Ding, M Tomizukas, and H Numasato. "Design and robustness analysis of dual stage servo system". In: *American Control Conference, 2000. Proceedings of the 2000*. Vol. 4. IEEE. 2000, pp. 2605–2609.

[26] John Doyle. *Lecture Notes for ONR*. Honeywell Workshop on Advances in Multivariable Control. Minneapolis, Minesota, 1984.

[27] Richard M Ehrlich, Jong Lin, David B Jeppson, and Kenji Oki. *Hard disk drive having self-written servo burst patterns*. US Patent 6,519,107. Feb. 2003.

[28] Gorka Galdos, Alireza Karimi, and Roland Longchamp. "H-infinity controller design for spectral MIMO models by convex optimization". In: *Journal of Process Control* 20.10 (2010), pp. 1175–1182.

[29] Graham C Goodwin, Michel Gevers, and Brett Ninness. "Quantifying the error in estimated transfer functions with application to model order selection". In: *IEEE Transactions on Automatic Control* 37.7 (1992), pp. 913–928.

[30] Takeyori Hara and Masayoshi Tomizuka. "Multi-rate controller for hard disk drive with redesign of state estimator". In: *American Control Conference, 1998. Proceedings of the 1998*. Vol. 5. IEEE. 1998, pp. 3033–3037.

[31] Daniel Hernandez, Sung-Su Park, Roberto Horowitz, and Andrew K Packard. "Dual-stage track-following servo design for hard disk drives". In: *American Control Conference, 1999. Proceedings of the 1999*. Vol. 6. IEEE. 1999, pp. 4116–4121.

[32] Guido Herrmann and Guoxiao Guo. "HDD dual-stage servo-controller design using a μ-analysis tool". In: *Control engineering practice* 12.3 (2004), pp. 241–251.

[33] Leslie Hogben. *Handbook of linear algebra*. CRC Press, 2006.

[34] Roberto Horowitz, Yunfeng Li, Kenn Oldham, Stanley Kon, and Xinghui Huang. "Dual-stage servo systems and vibration compensation in computer hard disk drives". In: *Control Engineering Practice* 15.3 (2007), pp. 291–305.

[35] Roberto Horowitz, Yunfeng Li, Kenn Oldham, Stanley Kon, and Xinghui Huang. "Dual-stage servo systems and vibration compensation in computer hard disk drives". In: *Control Engineering Practice* 15.3 (2007), pp. 291–305.

[36] Zhong-Sheng Hou and Zhuo Wang. "From model-based control to data-driven control: survey, classification and perspective". In: *Information Sciences* 235 (2013), pp. 3–35.

[37] Fu-Ying Huang, Tetsuo Semba, Wayne Imaino, and Francis Lee. "Active damping in HDD actuator". In: *IEEE Transactions on Magnetics* 37.2 (2001), pp. 847–849.

[38] Akihide Jinzenji, Tatsuro Sasamoto, Koichi Aikawa, Susumu Yoshida, and Keiji Aruga. "Acceleration feedforward control against rotational disturbance in hard disk drives". In: *IEEE Transactions on Magnetics* 37.2 (2001), pp. 888–893.

[39] EI Jury and J Blanchard. "A stability test for linear discrete systems in table form". In: *Proc. IRE* 49.12 (1961), pp. 1947–1948.

[40]   Rudolph Emil Kalman. "A new approach to linear filtering and prediction problems". In: *Journal of basic Engineering* 82.1 (1960).

[41]   Alireza Karimi and Christoph Kammer. "A Data-driven Approach to Robust Control of Multivariable Systems by Convex Optimization". In: *arXiv preprint arXiv:1610.08776* (2016).

[42]   Alireza Karimi, Achille Nicoletti, and Yuanming Zhu. "Robust H-infinity controller design using frequency-domain data via convex optimization". In: *International Journal of Robust and Nonlinear Control* (2016).

[43]   Vamsee Kasavajhala. "Solid state drive vs. hard disk drive price and performance study". In: *Proc. Dell Tech. White Paper* (2011), pp. 8–9.

[44]   Pramod P Khargonekar and Mario A Rotea. "Mixed H-2/H-infinity control: a convex optimization approach". In: *IEEE Transactions on Automatic Control* 36.7 (1991), pp. 824–837.

[45]   Masahito Kobayashi and Roberto Horowitz. "Track seek control for hard disk dual-stage servo systems". In: *IEEE Transactions on Magnetics* 37.2 (2001), pp. 949–954.

[46]   Seung-Hi Lee, Young-Hoon Kim, and Chung Choo Chung. "Dual-stage actuator disk drives for improved servo performance: Track follow, track seek, and settle". In: *IEEE transactions on magnetics* 37.4 (2001), pp. 1887–1890.

[47]   Lennart Ljung. *System identification*. Wiley Online Library, 1999.

[48]   Johan Lofberg. "YALMIP: A toolbox for modeling and optimization in MATLAB". In: *Computer Aided Control Systems Design, 2004 IEEE International Symposium on*. IEEE. 2004, pp. 284–289.

[49]   Paulo AC Lopes and Moisés S Piedade. "The behavior of the modified FX-LMS algorithm with secondary path modeling errors". In: *Signal Processing Letters, IEEE* 11.2 (2004), pp. 148–151.

[50]   MATLAB. *version 9.1.0 (R2016b)*. Natick, Massachusetts: The MathWorks Inc., 2016.

[51]   K Mori, T Munemoto, H Otsuki, Y Yamaguchi, and K Akagi. "A dual-stage magnetic disk drive actuator using a piezoelectric device for a high track density". In: *IEEE Transactions on Magnetics* 27.6 (1991), pp. 5298–5300.

[52]   Huy Nguyen, Omid Bagherieh, and Roberto Horowitz. "Settling Control of the Triple-Stage Hard Disk Drives Using Robust Output Feedback Model Predictive Control". In: *ASME 2016 Dynamic Systems and Control Conference*. American Society of Mechanical Engineers. 2016, V002T18A006–V002T18A006.

[53]   Jinwen Pan, Omid Bagherieh, Behrooz Shahsavari, and Roberto Horowitz. "Triple-Stage Track-Following Servo Design for Hard Disk Drives". In: *ASME 2016 Dynamic Systems and Control Conference, American Society of Mechanical Engineers*. 2016.

[54]   Rik Pintelon and Johan Schoukens. *System identification: a frequency domain approach*. John Wiley & Sons, 2012.

[55] Anders Rantzer and A Megretski. "A convex parameterization of robustly stabilizing controllers". In: *IEEE Transactions on Automatic Control* 39.9 (1994), pp. 1802–1808.

[56] Mark H Richardson and David L Formenti. "Parameter estimation from frequency response measurements using rational fraction polynomials". In: *Proceedings of the International Modal Analysis Conference*. 1982, pp. 167–182.

[57] HJ Richter, AY Dobin, O Heinonen, KZ Gao, RJMvd Veerdonk, RT Lynch, J Xue, D Weller, P Asselin, MF Erden, et al. "Recording on Bit-Patterned Media at Densities of 1 Tb/in and Beyond". In: *Magnetics, IEEE Transactions on* 42.10 (2006), pp. 2255–2260.

[58] Markus Rupp and Ali H Sayed. "Two variants of the FxLMS algorithm". In: *Applications of Signal Processing to Audio and Acoustics, 1995., IEEE ASSP Workshop on*. IEEE. 1995, pp. 123–126.

[59] Tetsuo Semba, Naoyuki Kagami, and Akira Tokizono. *Method and apparatus for suppressing mechanical resonance in a disk drive storage device using a notch filter*. US Patent 6,219,196. 2001.

[60] Behrooz Shahsavari, Richard Conway, Ehsan Keikha, Fu Zhang, and Roberto Horowitz. "Robust track-following controller design for hard disk drives with irregular sampling". In: *Magnetics, IEEE Transactions on* 49.6 (2013), pp. 2798–2804.

[61] Behrooz Shahsavari, Ehsan Keikha, Fu Zhang, and Roberto Horowitz. "Adaptive Repetitive Control Using a Modified Filtered-X LMS Algorithm". In: *ASME 2014 Dynamic Systems and Control Conference*. American Society of Mechanical Engineers. 2014, V001T13A006–V001T13A006.

[62] Behrooz Shahsavari, Ehsan Keikha, Fu Zhang, and Roberto Horowitz. "Repeatable Runout Following in Bit Patterned Media Recording". In: *ASME 2014 Conference on Information Storage and Processing Systems*. American Society of Mechanical Engineers. 2014, V001T03A001–V001T03A001.

[63] Cisco Systems. *Amount of Data Actually Stored in Data Centers Worldwide from 2015 to 2020 (in Exabytes). Statista - The Statistics Portal, Statista*. June 2017. URL: `www.statista.com/statistics/638613/worldwide-data-center-storage-used-capacity/`.

[64] TT Tay, JB Moore, and R Horowitz. "Indirect adaptive techniques for fixed controller performance enhancement". In: *International Journal of Control* 50.5 (1989), pp. 1941–1959.

[65] Eric W Weisstein. "Frobenius norm". In: (2003).

[66] Matthew T White, Masayoshi Tomizuka, and Craig Smith. "Improved track following in magnetic disk drives using a disturbance observer". In: *IEEE/ASME Transactions on mechatronics* 5.1 (2000), pp. 3–11.

[67] Robert L White, RMH Newt, and R Fabian W Pease. "Patterned media: a viable route to 50 Gbit/in 2 and up for magnetic recording". In: *Magnetics, IEEE Transactions on* 33.1 (1997), pp. 990–995.

[68] Shang-Chen Wu and Masayoshi Tomizuka. "An iterative learning control design for self-servowriting in hard disk drives". In: *Mechatronics* 20.1 (2010), pp. 53–58.

[69] Li Yi and Masayoshi Tomizuka. "Two-degree-of-freedom control with robust feedback control for hard disk servo systems". In: *IEEE/ASME transactions on mechatronics* 4.1 (1999), pp. 17–24.

[70] M Yu, L Wang, and T Chu. "Sampled-data stabilisation of networked control systems with nonlinearity". In: *Control Theory and Applications, IEE Proceedings-*. Vol. 152. 6. IET. 2005, pp. 609–614.

[71] Alan L Yuille and Anand Rangarajan. "The concave-convex procedure". In: *Neural computation* 15.4 (2003), pp. 915–936.

[72] Kemin Zhou, John Comstock Doyle, Keith Glover, et al. *Robust and optimal control*. Vol. 40. Prentice hall New Jersey, 1996.